

# **Thermoacoustic Instabilities in the Rijke Tube: Experiments and Modeling**

Thesis by

Konstantin Matveev

In Partial Fulfillment of the Requirements

for the Degree of

Doctor of Philosophy



California Institute of Technology

Pasadena, California

2003

(Defended February 7, 2003)



## ACKNOWLEDGEMENTS

I gratefully acknowledge help and support of members of Caltech community who have influenced the development of my research toward the Ph.D. thesis.

First and foremost, I would like to thank my advisor, Professor Fred Culick, for introducing me into the world of thermoacoustic and combustion instabilities, and for his guidance during my graduate study and thesis preparation. I appreciate his encouragement and help with my work on other topics of fluids engineering. Also, I wish to thank Professors Tim Colonius, Richard Murray, and Ken Pickar for serving on my thesis committee.

I was lucky to have great colleagues at the Jet Propulsion Center, Caltech. Winston Pun and Steve Palm helped me a lot with experimental apparatus, instrumentation and signal processing. I also benefited from discussions with Al Ratner.

I would like to thank my previous scientific advisor Igor Borisovich Esipov, D.Sc., and his research group at Andreyev Acoustics Institute in Moscow.

Special thanks to my parents and to my wife, Anna, for their support and understanding.

## ABSTRACT

Thermoacoustic instability can appear in thermal devices when unsteady heat release is coupled with pressure perturbations. This effect results in excitation of eigen acoustic modes of the system. These instabilities are important in various technical applications, for instance, in rocket motors and thermoacoustic engines.

A Rijke tube, representing a resonator with a mean flow and a concentrated heat source, is a convenient system for studying the fundamental physics of thermoacoustic instabilities. At certain values of the main system parameters, a loud sound is generated through a process similar to that in real-world devices prone to thermoacoustic instability. Rijke devices have been extensively employed for research purposes. The current work is intended to overcome the serious deficiencies of previous investigations with regard to estimating experimental errors and the influence of parameter variation on the results. Also, part of the objective here is to account for temperature field non-uniformity and to interpret nonlinear phenomena. The major goals of this study are to deliver accurate experimental results for the transition to instability and the scope and nature of the excited regimes, and to develop a theory that explains and predicts the effects observed.

An electrically heated, horizontally oriented, Rijke tube is used for the experimental study of transition to instability. The stability boundary is quantified as a function of major system parameters with measured uncertainties for the data collected. Hysteresis in the stability boundary is observed for certain operating regimes of the Rijke tube.

An innovative theory is developed for modeling the Rijke oscillations. First, linear theory, incorporating thermal analysis that accurately determines the properties of the modes responsible for the transition to instability, is used to predict the stability boundary. Then, a nonlinear extension of the theory is derived by introducing a hypothesis for a special form of the nonlinear

heat transfer function. This nonlinear modeling is shown to predict the hysteresis phenomenon and the limit cycles observed during the tests.

A new, reduced-order modeling approach for combustion instabilities in systems with vortex shedding is derived using the developed analytical framework. A hypothesis for the vortex detachment criterion is introduced, and a kicked oscillator model is applied to produce nonlinear results characteristic for unstable combustion systems.

The experimental system and the mathematical model, developed in this work for the Rijke tube, are recommended for preliminary design and analysis of real-world thermal devices, where thermoacoustic instability is a concern.

**TABLE OF CONTENTS**

Acknowledgements	iii
Abstract	iv
Table of Contents	vi
List of Figures	ix
List of Tables	xiii
CHAPTER 1 INTRODUCTION	1
1.1 Thermoacoustic Instability	1
1.2 Motivation	2
1.3 Rijke Tube	5
1.4 Literature Survey	6
1.5 Status of Understanding of Rijke Oscillations	11
1.6 Objectives	13
CHAPTER 2 EXPERIMENTAL APPARATUS AND RESULTS	15
2.2 Experimental Apparatus and Instrumentation	15
2.2 Test Procedure and Data Acquisition	20
2.3 Stability Boundaries for Instability in the First Mode	30
2.4 Stability Boundary for Instability in the Second Mode	38
2.5 Limit Cycles	42
2.6 Summary of Experimental Results	52

CHAPTER 3 SIMPLIFIED MODELING	53
3.1 Objectives and Assumptions	53
3.2 Analysis	55
3.3 Results and Discussion	58
CHAPTER 4 HEAT TRANSFER ANALYSIS	62
4.1 Heat Balance Equations	62
4.2 Correlations for Heat Transfer Rates	67
4.3 Thermal Radiation Model	70
4.4 Computational Procedure	72
4.5 Tuning of Heat Transfer Model	74
CHAPTER 5 LINEAR THEORY	77
5.1 Wave Equation	77
5.2 Damping Mechanisms	80
5.3 Matching Conditions at the Heater	84
5.4 Transfer Function	86
5.5 Computational Procedure	90
5.6 Results and Discussion	96
CHAPTER 6 NONLINEAR MODELING	103
6.1 Nonlinear Effects	103
6.2 Heat Transfer in Pulsating Flow	105
6.3 Stability Boundaries	113
6.4 Hysteresis Effect	116

6.5 Limit-Cycles Properties of a Self-Excited Mode	119
6.6 Simplified Theory for Higher Harmonics	122
CHAPTER 7 CONCLUDING REMARKS	128
APPENDIX A Model for Combustion Instability in the Systems with Vortex Shedding	132
A.1 Introduction	132
A.2 Theory	136
A.3 Some Results	143
REFERENCES	151



## LIST OF FIGURES

Figure 1-1: Thermal system with unsteady heat release.	1
Figure 1-2: Effect of equivalence ratio on NO <sub>x</sub> production.	3
Figure 1-3: Landfill flare station.	4
Figure 1-4: Scheme of a thermoacoustic engine.	4
Figure 1-5: Original configuration of the Rijke tube.	5
Figure 1-6: Horizontal electric Rijke tube with a forced mean flow.	6
Figure 2-1: Experimental setup of the Rijke tube.	16
Figure 2-2: Dimensions of the insulation frame and the heater assembly.	17
Figure 2-3: Steady state recordings on the Rijke tube ( $x/L = 1/4$ ; stable case).	24
Figure 2-4: Steady state recordings on the Rijke tube ( $x/L = 1/4$ ; excited case).	26
Figure 2-5: Steady state recordings on the Rijke tube ( $x/L = 5/8$ ; excited case).	27
Figure 2-6: Power spectra of pressure signals.	29
Figure 2-7: RMS of pressure oscillation near the stability boundary.	32
Figure 2-8: Dominant frequency of pressure oscillation near the stability boundary.	33
Figure 2-9: Transition to instability for heater location $x/L = 1/4$ .	35
Figure 2-10: Transition to instability for heater location $x/L = 1/8$ .	37
Figure 2-11: Transition to instability for heater location $x/L = 5/8$ .	39
Figure 2-12: Dominant frequency in the signal on transition to instability.	41
Figure 2-13: Amplitudes of the excited mode and its harmonics of the Rijke tube in the unstable state. Mass flow rate 1.63 gm/sec; $x/L = 1/4$ .	45
Figure 2-14: Frequencies of the excited mode and its harmonics of the Rijke tube in the unstable state. Mass flow rate 1.63 gm/sec; $x/L = 1/4$ .	46
Figure 2-15: Amplitudes of the excited mode and its harmonics of the Rijke tube in	

the unstable state. Mass flow rate 2.40 gm/sec; $x/L = 1/4$ .	47
Figure 2-16: Frequencies of the excited mode and its harmonics of the Rijke tube in the unstable state. Mass flow rate 2.40 gm/sec; $x/L = 1/4$ .	48
Figure 2-17: Amplitude and frequency of the excited mode of the Rijke tube in the unstable state. Mass flow rate 2.05 gm/sec; $x/L = 5/8$ .	50
Figure 2-18: Amplitude and frequency of the excited mode of the Rijke tube in the unstable state. Mass flow rate 2.21 gm/sec; $x/L = 5/8$ .	51
Figure 3-1: One-dimensional Rijke tube with a concentrated heat source.	54
Figure 3-2: Magnitude and phase delay of the transfer function.	57
Figure 3-3: Stability boundaries calculated by simplified modeling and compared with experimental data.	59
Figure 4-1: Structural model of the Rijke tube for heat transfer analysis.	63
Figure 4-2: Model of the downstream tube section for thermal radiation analysis.	70
Figure 4-3: Calculated and measured temperatures in structural components.	75
Figure 5-1: Duct with one-dimensional flow and a plane heat source.	80
Figure 5-2: Magnitude and phase delay of the transfer function $Tr$ .	89
Figure 5-3: Mode shapes of the first and the second modes.	94
Figure 5-4: Structure of numerical algorithm for determining stability boundary.	95
Figure 5-5: Comparison of the experimental (crosses) and calculated (solid line) results for transition to instability. Heater location $x/L = 1/4$ .	97
Figure 5-6: Comparison of the experimental (crosses) and calculated (solid line) results for transition to instability. Heater location $x/L = 1/8$ .	98
Figure 5-7: Comparison of the experimental (crosses) and calculated (solid line) results for transition to instability. Heater location $x/L = 5/8$ .	100
Figure 5-8: Calculated frequency of the unstable mode at the transition to instability.	

Measured dominant frequency in the signal after the transition to instability.	101
Figure 6-1: Time variation of the reduced velocity in the incident flow and the quasi-steady heat transfer rate.	107
Figure 6-2: Nonlinear corrections, calculated using model 1 and model 2, for the mean heat transfer rate and the transfer function.	109
Figure 6-3: Amplitudes of higher harmonics of the heat transfer rate.	110
Figure 6-4: Stability boundary for three heater positions.	114
Figure 6-5: Transition between stable and excited states. Mass flow rate 2.75 gm/sec. Heater location $x/L = 1/4$ .	117
Figure 6-6: Transition between stable and excited states. Mass flow rate 0.89 gm/sec. Heater location $x/L = 1/4$ .	118
Figure 6-7: Properties of the excited eigen acoustic mode at heater location $x/L = 1/4$ and mass flow rate 1.63 gm/sec.	120
Figure 6-8: Properties of the excited eigen acoustic mode at heater location $x/L = 1/4$ and mass flow rate 2.40 gm/sec.	121
Figure 6-9: Properties of the excited eigen acoustic mode at heater location $x/L = 5/8$ and mass flow rates 2.05 gm/sec and 2.20 gm/sec.	122
Figure 6-10: Properties of higher harmonics of the excited mode at heater location $x/L = 1/4$ . and mass flow rate 1.63 gm/sec.	125
Figure 6-11: Properties of higher harmonics of the excited mode at heater location $x/L = 1/4$ . and mass flow rate 2.40 gm/sec.	126
Figure A-1: Acoustic / vortex / combustion interactions.	135
Figure A-2: Stable and unstable flow in dump combustor.	137
Figure A-3: Lock-in regions: (a) around $f_{s0}/f_p = 1$ ; (b) around $f_{s0}/f_p = 0.5$ .	143
Figure A-4: Coefficient of the mode importance.	146

Figure A-5: Pressure fluctuations near at the lip in the limit-cycle regime calculated using one-mode and six-mode models. Mean flow velocity 40 m/s.	147
Figure A-6: Amplitude spectra of the pressure fluctuation.	148
Figure A-7: Amplitudes of the spectral peaks in steady-state regimes.	149

**LIST OF TABLES**

Table 2-1: PCB 112A04 pressure transducer properties with 422D11 charge amp.	18
Table 2-2: Data acquisition analog measurements.	20
Table 4-1: Dependence of Nusselt number on reduced distance for simultaneously developing flow.	69
Table 4-2: Discrepancy between measured and calculated temperatures.	76
Table 5-1: Reflection coefficient of the chamber rear wall as a function of frequency.	83

## Chapter 1

# Introduction

### 1.1 Thermoacoustic instability

Thermoacoustic instabilities refer to the appearance of pressure oscillation coupled with an unsteady heat release. The idea can be understood from the diagram, shown in Figure 1-1. A chamber of a thermal device, such as a combustor, possesses certain acoustic properties. If the heat, released in the system, depends on pressure and velocity fluctuations, a feedback loop is formed, that can destabilize the system.

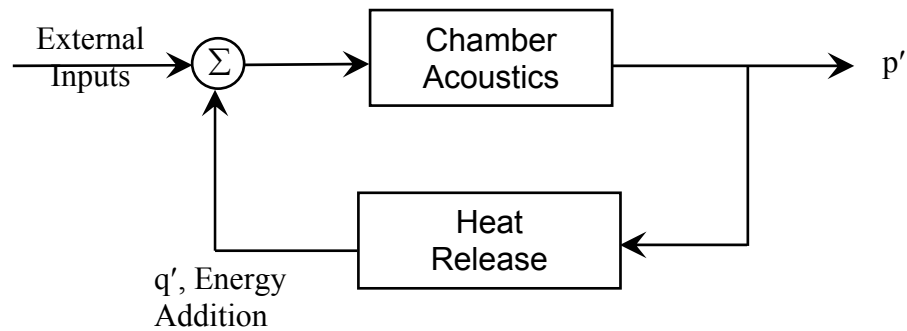


**Figure 1-1: Thermal system with unsteady heat release.**

In the 19th century Lord Rayleigh proposed a criterion for heat-driven acoustic oscillation:

“If heat be given to the air at the moment of greatest condensation, or be taken from it at the moment of greatest rarefaction, the vibration is encouraged. On the other hand, if heat be given at the moment of greatest rarefaction, or abstracted at the moment of greatest condensation, the vibration is discouraged.”

This rule can be conveniently expressed via transformation of thermal energy to acoustic energy. Considering conservation equations, Culick (1976) derived an expression for the energy addition to the acoustic mode

$$(1-1) \quad \Delta E = \frac{\gamma - 1}{p_0 \gamma} \int_V dv \int_t^{t+T} p' \dot{Q}' dt,$$

where  $p'$  is the pressure perturbation;  $\dot{Q}'$  is the fluctuation of the heat release rate;  $\gamma$  is the gas constant;  $p_0$  is the mean ambient pressure;  $V$  is the chamber volume; and  $T$  is the cycle period. Equation (1-1) is an explicit interpretation of Rayleigh's criterion, showing that instability is encouraged when the heat release fluctuates in phase with the pressure perturbation. If the energy input exceeds acoustic losses, then the system becomes unstable.

## 1.2 Motivation

Thermoacoustic instability plays an important role in various technical applications. We briefly consider several examples of the most significant exhibitions of this phenomenon: combustion instability in propulsion systems and low-pollutant lean flames; noise generation in industrial burners; enhanced combustion of heavy oils; and development of thermoacoustic engines.

Rocket and gas turbine engines can be susceptible to combustion instability, which is a particular case of thermoacoustic instability. Pressure and flow oscillations inside a motor can lead to unacceptable levels of vibration and enhanced heat transfer that degrade propulsive

efficiency, and damage or even destroy the system. Both solid and liquid fueled propulsion systems can be prone to instability, and this effect has been extensively studied for a long time (e.g., Culick 1988, Margolin 1999).

In recent years, strict regulations are being imposed on new combustion devices, requiring significant reduction of pollutant emission, in particularly  $\text{NO}_x$ . At low combustion temperatures, realized in lean flames, the emission decreases (Figure 1-2). However, flames tend to be unstable near the lean limit, and their coupling with combustor acoustics may result in combustion instability. This is a major problem and an active research topic in modern gas turbine industry (Correa 1998).

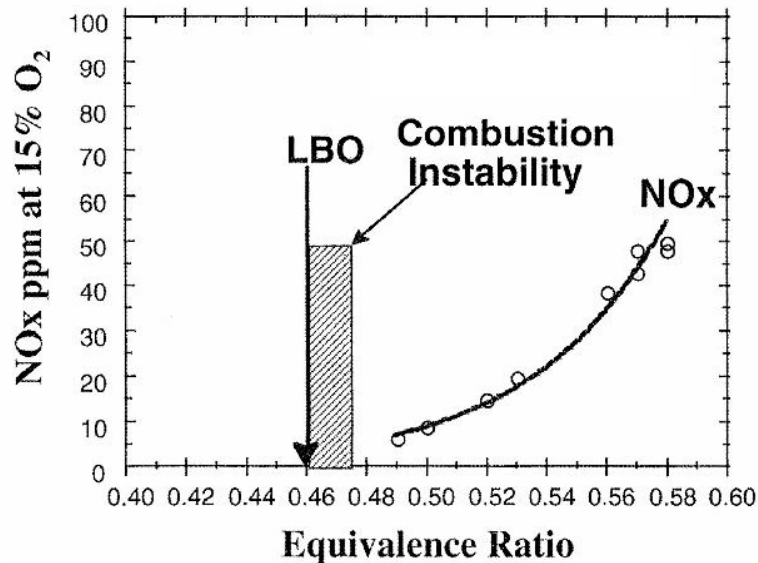


**Figure 1-2: Effect of equivalence ratio on  $\text{NO}_x$  production (from Rosfjord 1995).**

Another problem associated with acoustically unstable combustors is the intensive noise. Pun (2001) describes the unstable gas flares aimed at burning landfill gas, produced by decomposing material in LA county waste fields (Figure 1-3). When this system operates at the burning capacity exceeding 50% from the maximally possible, a loud, low-frequency rumbling is generated, unacceptable to people living near this facility. The tones excited correspond to eigen



acoustic modes of the flares; possible driving mechanisms are thermoacoustic instability, feed system coupling, and interaction between vortex shedding and chamber acoustics.



**Figure 1-3: Landfill flare station (from Pun 2001).**

Thermoacoustic instability is not always a negative phenomenon. Specially designed pulse combustors of a Rijke type use this effect to increase burning rate of heavy fuel oils (Bai et al. 1993). In conventional steady burners several problems usually arise with such fuels: incomplete combustion, soot emission, long flames, and wall deposits.

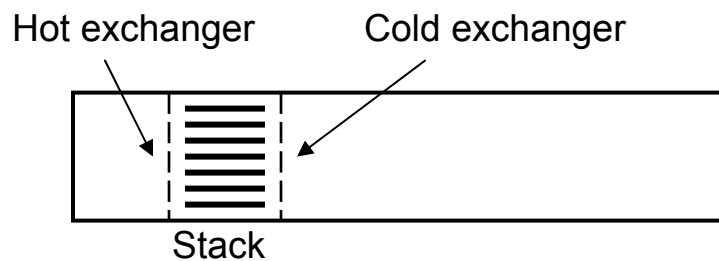


**Figure 1-4: Scheme of a thermoacoustic engine.**

The development of thermoacoustic engines is becoming an active research area. Based on thermoacoustic effects, these engines can serve as prime movers and refrigerators (Swift 1988, Garret and Backhaus 2000). In the first case, sound waves are generated when a sufficient temperature gradient is created in the stack (Figure 1-4), and resulting acoustic energy can be converted to electricity or applied for other purposes. If the temperature gradient is moderate and an external acoustic field applied, then heat can be pumped from a low-temperature source to a high-temperature sink, i.e., a refrigerating effect is produced.

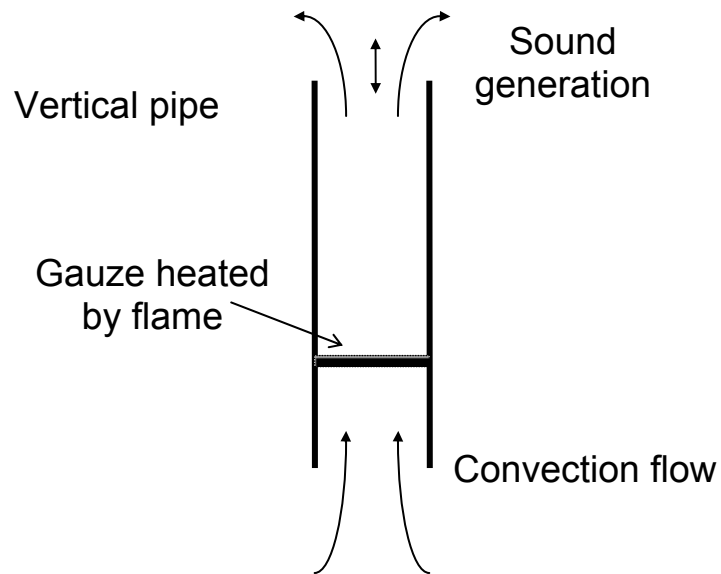


**Figure 1-5: Original configuration of the Rijke tube.**

### 1.3 Rijke tube

Thermoacoustic instability is a complex phenomenon, and to understand its nature some simplified models must be used. A Rijke tube is a convenient system for studying thermoacoustic instabilities both experimentally and theoretically. The original Rijke tube (Rijke 1859) consisted of a vertical pipe with a gauze, located in the lower half of the tube and heated by a flame (Figure

1-5). A mean flow in the tube appears due to natural convection. For sufficiently high temperature of the gauze, a high-intensity tone is generated. Explanation of the appearance of sound in a Rijke tube, using Equation (1-1), is given in Chapter 3.

Despite the simplicity of a vertical Rijke tube, it does not permit independent variation of the mean flow and the power supplied to a gauze. A horizontally located Rijke with a mean flow, provided by a blower, and the air-permeable gauze, heated by electric current, overcomes this deficiency (Figure 1-6). Another advantage of an electric Rijke tube is the possibility for precise control of the main system parameters in wide ranges: heater location, air flow rate, and heat power released. In our experiments, this type of a Rijke tube is employed. For a certain range of the main system parameters, the tube produces a tonal sound with frequencies close to the natural frequencies of the system.

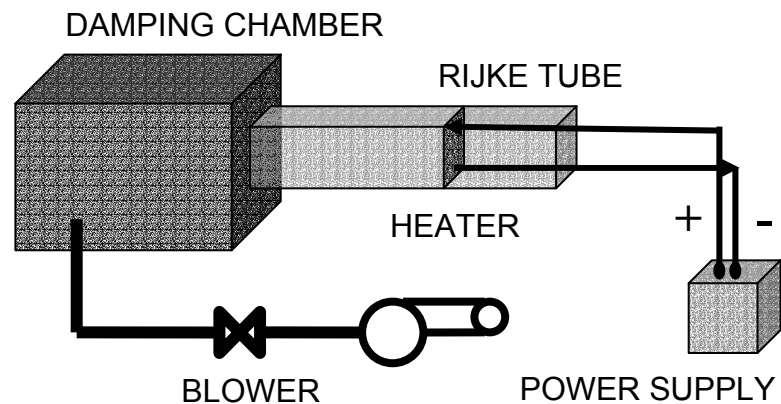


**Figure 1-6: Horizontal electric Rijke tube with a forced mean flow.**

## 1.4 Literature survey

Heat-driven sound generation in closed chambers belongs to thermoacoustics. This field includes interesting areas such as combustion instabilities (Culick 1988) and thermoacoustic engines (Swift 1988). Our study is dedicated only to a particular device, a Rijke tube, that exhibits major

phenomena associated with thermoacoustics. Extensive reviews on Rijke oscillations are given by Feldman (1968), Raun et al. (1993), and Bisio and Rubatto (1999). The major goals of experimental investigations of a Rijke tube are to determine transition to instability as a function of system parameters and to study excited regimes. The purposes of theoretical investigations are to model the stability boundaries and the limit cycles. In this section the papers of most interest and relevance to our study are briefly surveyed.

Higgins (1802) discovered singing flames when a jet of ignited gas was inserted into the tube open at both ends. The frequency of singing coincided with the natural frequency of the tube. Sound was produced only at certain ranges of system parameters.

Rijke (1859) discovered that a tonal sound was generated by sufficiently hot gauze when it was located in the lower half of an open-ended vertical tube. Oscillations were the most intensive at the heater position of one quarter of the tube length from a lower tube end. Sound generation was attributed to air expansion near the grid and contractions at the upper cooler tube section. However, this hypothesis was not sufficient to explain the oscillations.

Rayleigh (1945) proposed a criterion for the necessary condition of thermoacoustic instability: oscillations are encouraged when heat fluctuates in phase with pressure perturbation. Rayleigh assumed that this criterion is fulfilled in the Rijke tube and is the major reason for the experimental findings.

The first quantitative analysis of the Rijke phenomenon was made by Lehmann (1937). He assumed that air received heat from the grid only on the way forward; on the way back, at the reverse air motion, no heat transfer took place. Some consequences of his theory were not confirmed later by experimental results, and Feldman (1968) and Raun et al. (1993) concluded that Lehmann's theory is erroneous. However, in this study we will show how the idea proposed by Lehmann can be utilized in nonlinear modeling of the excited regimes of operation of the Rijke tube that produces results in accordance with experiments.

Neuringer and Hudson (1952) modeled Rijke oscillations and concluded that tone excitation is greatly dependent on the turbulence in the flow and the velocity gradient at the heater. Their results only partly agreed with experimental findings.

Putnam and Dennis (1953) derived a heat-driven wave equation. Rayleigh's criterion was verified by showing that instability is encouraged in a Rijke tube when the phase difference between pressure and heat release fluctuations was less than  $90^\circ$ .

Using conservation equations, Carrier (1955) applied linear perturbation analysis to obtain a system of dynamic equations. The corresponding eigenvalues, found numerically, defined stability properties of the Rijke tube. Carrier elaborated the response of the ribbon heating element to a fluctuating flow.

Starting from the first principles of fluid mechanics, Merk (1957) derived a mathematical model for thermoacoustic systems with concentrated heat sources and constant temperature sections. He introduced the transfer functions of the heater to the analyses of Rijke oscillations. In theoretical portion of our work, we will use the concept of transfer functions, implementing, however, more accurate approach to model real systems.

A simplified model was proposed by Maling (1963), based on the works by Putnam and Dennis (1953) and Carrier (1955). Maling represented a heat source by a delta function in one-dimensional formulation and obtained a considerably simpler stability equation.

Among experimental investigations dedicated to the study of stability boundaries in Rijke devices, the major papers are published by Saito (1965), Marone and Tarakanovskii (1967), Tarakanovskii and Steinberg (1972), Collyer and Ayres (1972), Katto and Sajiki (1977), and Madarame (1981). These papers contain a lot of information on transition to instability for various sets of basic system parameters. However, there were little discussions how these parameters were varied and how the order of variation influenced the stability boundaries. Experimental errors have not been reported in these works; and temperature measurements have been rarely accomplished; the exceptions are the recent papers by Finlinson et al. (1987) and

McQuay et al. (2000) on Rijke burners, where only a few system conditions can be tested. All mentioned factors, not sufficiently studied in the previous papers on Rijke tubes, strongly affect the actual transition to instability and have to be accurately assessed. That motivated the experimental study accomplished in our work.

Further progress in modeling the onset of Rijke oscillations has been reflected in several papers appeared since the 1980's. Madarame (1981) obtained unsteady temperature distribution near a heat source by solving a heat conduction equation. The amount of energy input supplied to oscillations was computed. The stability boundary agreed with experiments only when a special shifting was imposed on data.

Kwon and Lee (1985) reported results for the heat transfer of a cylinder in superimposed oscillating and steady flows. Employing the finite difference method, they calculated time-dependent heat transfer response of the cylinder to velocity fluctuations by treating the flow as incompressible and two-dimensional. The flow regime around a cylinder corresponded to an intermediate range of the Reynolds number when the Oseen approximation is already invalid and a boundary layer is not yet formed. They also derived a simplified analysis for thermoacoustic instability of a Rijke tube and presented a calculated stability curve in agreement with a specially selected configuration from the experiments by Katto and Sajiki (1977). The maximum thermoacoustic transformation efficiency was found to occur when a wire radius was on the order of the thermal boundary layer and mean flow velocity close to the thermal diffusion velocity.

Nicoli and Pelce (1989) derived a one-dimensional model for the Rijke tube, including effects of gas compressibility and variable fluid properties. Diffusive time was chosen to be small compared with the transit time across the grid. Velocity transfer function was computed, and stability boundary was modeled for the case of constant temperatures in tube sections.

Yoon et al. (1998) studied analytically the stability properties of generalized Rijke tubes with different phenomenological thermoacoustic response models. A solution methodology was based on modal analysis.

Ishii et al. (1998) carried out a numerical study of transition to instability of the heated air column in a simplified formulation. A comparison of growth rates and some temperature variation was made with their experimental results and those by Madarame (1981). The energy of driving and damping air column vibration was estimated and discussed for explaining the air column excitation.

A significant deficiency of all these works is the absence of a thermal analysis, which determines temperature distribution in a tube. Mode shapes and matching conditions on the heater, defining transition to instability, are dependent on the non-uniform temperature field. There are two papers that deal with non-uniform temperature profiles in Rijke burners. Raun and Beckstead (1993) developed an interpolating model for determining the average temperature profile based on the simplified energy equation and temperature measurements at the certain points in the burner. McIntosh and Rylands (1996) studied the influence of heat loss downstream the flame on instability regimes, applying the procedure similar to that suggested by Raun and Beckstead (1993).

Though less critical due to its small value, a heater impedance is usually neglected in modeling Rijke oscillations. Heat transfer characteristics of the heater are of great importance for stability properties. For some limiting values of the system parameters, analytical estimations can be obtained for particular heater geometry (Merk 1957, Bayly 1985, Nicoli and Pelce 1989); for flow conditions unsuitable for theoretical analysis, CFD is used (Kwon and Lee 1985).

Only a few works devoted to studying the nonlinear aspects of the Rijke tube, are available in the literature. Madarame (1981) carried out an extensive experimental investigation of the stability boundaries and unstable regimes; however, no hysteresis was reported, and no analysis was done to interpret the limit cycle properties.

Bayly (1986) developed a theory in the Oseen limit for the nonlinear heat transfer from the gauze in the presence of acoustic motion. Flow reversal and unfavorable phasing between heat and pressure fluctuations were cited as factors limiting instability development. The model also

predicted hysteresis effects, i.e., the dependence of the stability boundary between stable and unstable states on the direction of parameter variation.

Heckl (1988) demonstrated the application of active control to suppress instabilities in a Rijke tube. A special theory was developed for explaining the effect of the feedback system. In another paper by Heckl (1990), nonlinear effects in a Rijke tube were investigated experimentally for a few sets of system parameters, and a derived empirical model for the system stability was fitted to the experimental results.

Assuming simplified geometry and enhanced thermal conductivity, Hantschk and Vortmeyer (1999) applied a commercially available CFD code for simulation of the instability in a Rijke tube. Results agreed well with an experiment, although the comparison was made for only one system condition.

Yoon et al. (2001) constructed a two-mode model of acoustic behavior in a heated duct, applying some phenomenological law for the thermal response of a concentrated heater to velocity fluctuations and ignoring other factors. The results of parametric studies were presented.

A numerical study of unsteady thermoacoustic field in a Rijke type device was carried out by Entezam et al. (2002). Using some simplifying assumptions, they investigated a transient process of transition to instability and a saturation of limit cycle amplitudes. Results were reported for several sets of system parameters and no direct comparison was made with experiments; hence, the general validity of the numerical tool created is questionable.

## **1.5 Status of understanding of Rijke oscillations**

A Rijke tube is a simple experimental system convenient for the parametric study of thermoacoustic instability. Previous tests determined the general dependence of the behavior of this device on variations in primary parameters. For instance, in order to make the first acoustic



mode unstable, the heater must be located in the upstream half of the tube; the most favorable position is near one quarter of the tube length. For second mode excitation, the heater should be located either in the first or third quarter of the tube as measured from the upstream end. The larger the quantity of heat delivered to the air flow, the more prone to instability the system is, with all other parameters kept fixed. With a constant heater location and input power, a Rijke tube can always be made stable with a flow rate either sufficiently low or sufficiently high; i.e., there is a limited range of flow rates where thermoacoustic instability can be observed. Despite a number of previously reported experiments, there is a lack of accurate data with specified experimental errors and with an adequately described data acquisition process which could be used for quantitative comparison with thermoacoustic theories.

The previous studies of Rijke tubes with heating elements have established that the appearance of thermoacoustic instability is the result of the presence of unsteady heat release component  $\dot{Q}'$  that fluctuates in phase with the pressure perturbation  $p'$ . In this case, according to Rayleigh's criterion (1-1), there is a positive thermal-to-acoustic energy transformation. Since heat addition to air flow in systems with heating elements occurs commonly through convection, the unsteady heat transfer rate is a function of the velocity perturbation  $u'$  (in low Mach number flows). If the magnitude of acoustic velocity oscillations is small in comparison with the mean flow velocity  $u_0$  (linear regime) and the period of oscillations is infinitely large (quasi-steady regime), then the unsteady heat transfer rate is proportional to the velocity perturbation  $\dot{Q}'_{qs}(t) \sim u'(t)$ . The inertia of the heat transfer process leads to the appearance of a time delay in unsteady flows with a finite frequency of oscillation  $\dot{Q}'(t) \sim u'(t - \tau)$ , where the time delay  $\tau$  depends on the system properties. Therefore, an unsteady component of the heat transfer rate fluctuating in phase with pressure perturbation can arise, and the integral in Rayleigh's criterion (1-1) can become greater

than zero in a certain range of  $\tau$ , i.e.,  $\int_t^{t+T} p' \dot{Q}' dt > 0$ . Simplified modeling, based on the argument just discussed and similar to the analyses done so far in the literature, will be presented in Chapter 3. Since this theory does not take into account some important effects, such as the non-uniformity of the temperature field in the system, this model can serve only for illustrative purposes.

Thus, the qualitative reasons for Rijke oscillations are currently well understood with the uncertainty remaining in the unsteady heat transfer at the heater. However, there is lack of both experiments providing data with specified measurement errors and models capable of accurately predicting the transition to instability and the properties of unstable regimes of thermoacoustic devices. The present work attempts to advance in that direction.

## 1.6 Objectives

The purpose of this work is to overcome the deficiencies of the previous investigations of Rijke devices. The main objectives are

- to obtain accurate experimental data for transition to instability and excited regimes obtained within wide ranges of the main system parameters in the controlled environment of an electrical Rijke tube with a mean flow provided by a blower;
- to develop the mathematical model, incorporating heat transfer analysis, aimed at calculating stability boundaries, limit cycles, and history-dependent effects;
- to reveal which factors and system parameters are of major importance in accurately determining thermoacoustic instability.

Outline of the thesis:

Chapter 2 starts with a description of the experimental system. Then, the test procedures are discussed that allow us to obtain robust results suitable for comparison with modeling. Experimental data for stability boundaries are presented for three heater locations. A new effect, identified as hysteresis in the transition between stable and unstable states, is discovered. The limit cycle properties of the excited regimes of operation of the Rijke tube are reported.

Chapter 3 is devoted to simplified mathematical modeling (commonly used in the literature) of a Rijke tube, based on Rayleigh's criterion for acoustic eigen modes. Major assumptions and shortcomings of this approach are discussed.

Thermal modeling is presented in Chapter 4. Stability properties of the acoustic modes are dependent on the temperature field, which can be found only by utilizing heat transfer analysis.

Linear acoustic theory is applied in Chapter 5 to calculate stability boundaries in the Rijke tube. Non-uniform temperature distribution and all other major linear effects are taken into account. It is shown that theoretical results agree with experimental data much better than in the case when simplified modeling is used.

The nonlinear extension of this theory is developed in Chapter 6. Nonlinear effects are discussed and incorporated in the model. Nonlinear modeling explains the hysteresis phenomenon and predicts limit cycle properties.

Our findings and conclusions are summarized in Chapter 7.

A novel approach to the reduced-order modeling of combustion instabilities in the systems with vortex shedding, based on the derived analytical framework, is developed in Appendix.

The content of the thesis is partly presented in the author's papers (Matveev and Culick 2001, 2002a,b,c,d,e,f, 2003a,b).

## Chapter 2

# Experimental Apparatus and Results

### **2.1 Experimental apparatus and instrumentation**

The structure of the experimental apparatus, the Rijke tube, is shown in Figure 2-1. The horizontally placed Rijke tube is a square aluminum tube of 9.5 x 9.5 cm cross section and 1.0 m long. The thickness of tube walls is 3 mm. The mean air flow is provided by a blower, which sucks air in the tube. The fan allows us to control the mean flow rate, a major system parameter, precisely and independently of the thermal power release, which is also regulated. If the tube were kept vertically orientated, as in the original version by Rijke (Figure 1-5), then, first, it would be necessary to take into account a mean flow component caused by natural convection, and second, it would be difficult to provide low rates of mean flow at high levels of power. To exclude the influence of natural convection on a mean flow rate, the horizontal orientation of the Rijke tube has been implemented. A damping chamber, located between the tube and the blower, is intended to prevent interaction between the blower and tube acoustics. The chamber dimensions are 46 × 46 × 120 cm; its internal surface is covered by 1/2" pile carpet on 1/8" felt.

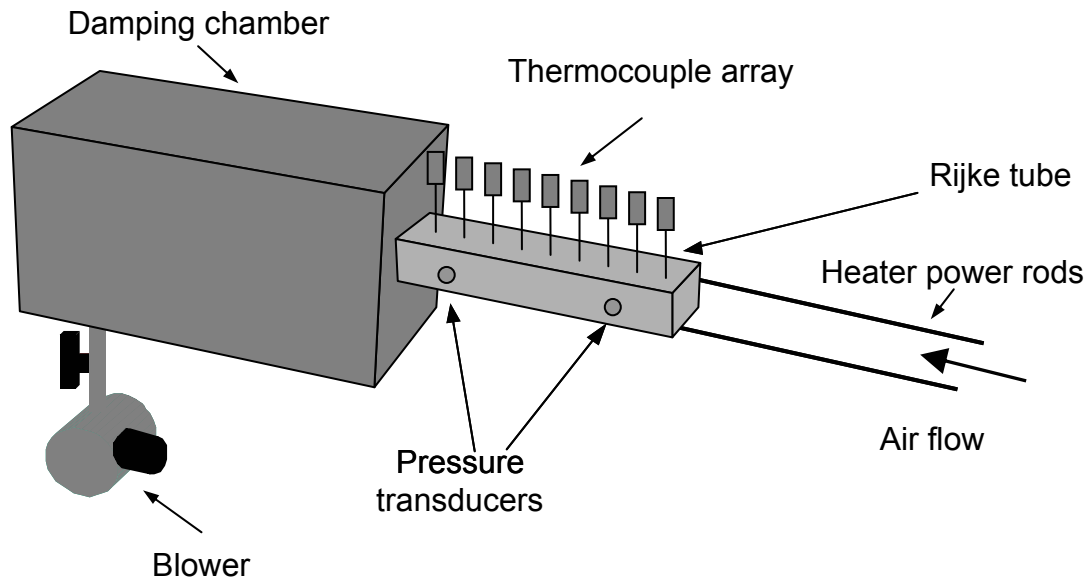


**Figure 2-1: Experimental setup of the Rijke tube.**

Since the major mystery about Rijke oscillations is associated with the heat transfer at the heater, it is desirable to select a heater with a heat transfer process that can be analytically modeled as precisely as possible. This suggests an array of parallel cylinders, located far from each other. In order to consider a heater to be infinitely thin in mathematical modeling (it would permit to apply the appropriate jump conditions), the cylinder diameter must be small, hence, a set of wires could be used. To measure stability properties of a Rijke tube in wide ranges of system parameters, a heater should also repeatedly withstand high temperatures for long time intervals and be able to release large amounts of thermal power (over 1 KW in our system) without geometry changes. Another desirable property is the ability to heat the air flow uniformly over a tube cross section. A square-weave 40-mesh made from nichrome is a suitable trade-off between these requirements. It has proved to be a reliable heating element, and the heat transfer resembles that of cylinders, accounting for a flow blockage effect. A wire diameter in the grid is

0.01". The gauze is brazed to two strips of copper, which are suspended on a square frame made from macor (machinable glass ceramic) in order to eliminate electric and reduce thermal contact with tube walls. The lay of the screen is parallel to the direction of electric current flow. Two copper rods with diameter 0.25", welded directly to the copper strips on the heater, connect the heater to the power source. The scheme of the heater assembly and the geometry of the frame are shown in Figure 2-2. Location of the heater can be easily changed within the tube.

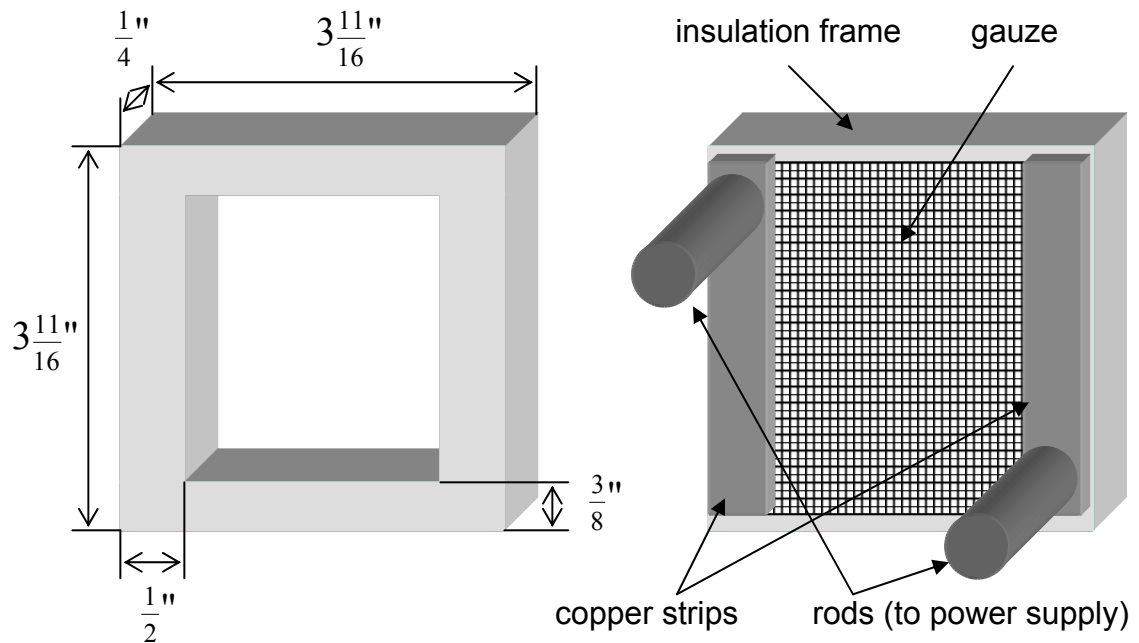


**Figure 2-2: Dimensions of the insulation frame and the heater assembly.**

The power source consists of two TCR-20T250 power supplies, each capable of producing 500 amps of current. The power supplies are load balanced and operate in parallel. The actual power supplied is dependent on the resistance of the nichrome grid, which changes with temperature. The power supplies are computer controlled using a software-implemented PI controller to stabilize the output power, although fluctuations on the order of  $\pm 1\%$  do occur with frequency 60 Hz. The control system for the power supply is discussed by Poncia (1998).

The mean air flow through the Rijke tube is provided by a GAST R1102 blower, operating at 3450 rpm with a maximum throughput of  $0.0127 \text{ m}^3/\text{s}$  at standard atmospheric conditions. The blower is operated at full capacity with a 2" by-pass ball valve controlling the amount of air drawn through the damping chamber, or from the atmosphere. The flow rate is measured using a laminar flow element (Meriam 50MW20) and a differential pressure transducer (Honeywell Microswitch). This measurement takes place between the damping chamber and the blower. The temperature measured with a thermocouple, located upstream of the laminar flow element, is the basis for correcting the air density and viscosity to produce accurate measurement of the air mass flow rate. The flow rate is determined from a calibration curve provided by the producer. A re-calibration procedure has been performed to convert the electronic measurement to a convenient curve for routine use. A large plastic shroud is placed above the entrance to the Rijke tube to minimize the effects of external air currents on the system.

Pressure transducers used in this experiment must be able to provide accurate measurements in a hot environment during long experimental runs. The transducers used were PCB model 112A04, coupled with a 422D11 charge amplifier and a 482A20 signal conditioner. Charge-mode

Sensitivity	100 mV/psi
Maximum Pressure	5000 psi
Linearity	< 1% FS
Temperature Range	-400 to +600 F
Flash Temperature	3000 F
Resonant Frequency	> 250 kHz
Rise Time	< 2 $\mu\text{s}$

**Table 2-1: PCB 112A04 pressure transducer properties with 422D11 charge amp.**

piezoelectric transducers were used, since the majority of the electronics is located in a separate charge amplifier, increasing the operating temperature range while retaining relatively high sensitivities. Important characteristics of the pressure transducers are listed in Table 2-1. The two pressure transducers are flush mounted in the tube at positions  $x/L = 0.15$  and  $x/L = 0.80$ . In most cases, one of the transducers is located on the cold side of the tube and another is on the hot side.

For measuring a temperature profile, an array of 15 type K thermocouples is suspended from the top of the tube to the centerline, at positions of  $x = 5, 10, 15, 22, 27, 30, 35, 40, 45, 50, 56.7, 63.3, 70, 76.7,$  and 90 cm. An additional thermocouple is located just before the laminar flow element that measures the mean flow through the tube. The spacing was selected to place more thermocouples nearer to the heat source when it is positioned at 25 cm from the upstream tube end, as well as to allow the heater to be located at key locations without interfering with the thermocouples. For validating the thermal modeling, some thermocouples are used at the exit and entrance cross sections for determination of averaged temperature in those sections. Since thermocouples have a relatively large time constant, they are multiplexed and sampled at 2 Hz. It is not possible for thermocouples to respond quickly enough at the acoustic time scales typical for our experiment. They are used solely for time averaged temperature measurements.

In order to provide accurate measurements of the acoustic pressures and other relevant parameters in the Rijke tube, a fast sampling system is required. The data acquisition system is based on a Pentium III 700 MHz computer. A Computer Boards' CIO-DAS1602/12 (12 bit) data acquisition board is installed in the machine, using the Sparrow program (Murray 1995) as the software interface. An EXP-16 expansion board accommodates 16 thermocouples in a multiplexed array and also provides cold junction compensation. The channels acquired are listed in Table 2-2.

The DAS1602/12 is operated in single-ended mode, giving a total of up to 16 analog input channels. It also contains two analog output channels, one of which is used to control the power supplies. In this configuration, data could be acquired in short bursts at over 8000 Hz, and for



extended periods of time streaming to the hard drive at over 4000 Hz. For this Rijke tube, the frequencies of the primary excited modes are approximately 180 Hz and 360 Hz. These frequencies and the waveforms are easily captured by the data acquisition system.

Channel	Measurement
0	System thermocouples
1	Cold junction compensation
2	Pressure transducer P1
3	Pressure transducer P2
4	Heater voltage
5	Flow rate (LFE pressure drop)
6	Heater current

**Table 2-2: Data acquisition analog measurements.**

## 2.2 Test procedure and data acquisition

In order to obtain robust data on the stability boundaries and the limit cycles in excited regimes, a careful methodology of data acquisition must be established. There are three basic parameters that can be controlled by the operator: heater position, air flow rate, and power supplied to the heater. At each operating condition, the pressure fluctuation, which is the output data of primary interest, can be recorded with a scan rate up to 8000 Hz. Additional information on the spatially resolved temperature profile along the tube and the temporarily resolved air flow rate, voltage and current is also available. In steady state, corresponding to a given triplet of the system parameters (heater location, air flow rate, and supplied power), one can analyze the pressure signal and declare

whether the system is in the stable or excited state; in the latter case, the limit cycle properties, i.e., amplitudes and frequencies of excited modes, can be extracted.

Since the two system parameters, air flow rate and heater position, are changed mechanically, they are fixed in the individual experimental runs, and the power is varied through the computer interface of the control system. At every steady-state system condition, characterized by a triplet of main parameters, data have been captured.

Stability boundaries are determined for three heater locations:  $1/4$ ,  $1/8$  and  $5/8$  of the tube length; the origin of the tube is taken to be at the open upstream end. These locations have been chosen with the intention of observing driving of the first mode ( $x/L = 1/4$ ), the second mode ( $x/L = 5/8$ ), and possibly the first two modes simultaneously ( $x/L = 1/8$ ). For each heater position, a set of mass flow rates values is selected to cover the range when transition to instability is possible. For each value of the mass flow rate, the power is varied, starting from zero, in order to reach a critical power when the transition to instability occurs.

Before commencing an experimental run, the tube is subjected to a warm-up procedure, to minimize temperature variations as the power input is increased. The warm-up depends on the actual conditions under which the experimental run will take place, based on anticipated stability boundaries. Typically, the power input will be set to approximately 200 W below the unstable point for a particular flow condition, and the tube run at that rate for 20 minutes. If the stability boundary is not known or incorrectly selected, a more conservative estimate of the stability boundary is used at the expense of increased duration for the experiment.

Following a change of power, the temperature field in the tube slowly responds. This unsteadiness, as well as finite power increments, can lead to initiation of the instability at lower power than it would be in the system with steady temperature distribution corresponding to a certain power level. It is observed in the experiments that the critical power obtained at large steps of power increments may significantly differ (to lower values) from the critical power obtained at small steps. To avoid this early initiation of instability, known as nonlinear triggering

(Burnley and Culick 2000), and to generate the results convenient for mathematical modeling, a quasi-steady procedure for power variation has been established. First, a settling time is imposed between power changes; during that period a steady temperature field is reached by the system. This time (of the order of a few minutes) is determined experimentally for different system configurations. Second, to obtain a critical power accurately, power increments should be made as small as possible; but this could lead to an unreasonable increase in the duration of the experiment. An iterative method with reduction of a power step has been implemented. Initially, large steps (50 W) are used for approximate location of the transition to instability; then this boundary is approached from below with smaller power increments, so that the accuracy in locating this transition is improved. A step in power variation is successively reduced until a converged value of the critical power is obtained; the minimally possible step corresponds to the intrinsic power oscillation of order 1%. Before data is acquired, the system parameters are held steady at each condition for approximately 4 minutes until the system temperature field has settled.

Since transition from the stable state to the unstable state does not coincide exactly with the reverse transition, another critical power is also determined, corresponding to the transition from the unstable to stable state. After excitation of the instability, several power increments are made in order to move from the transition point; then power is decreased, using the same (small) steps and settling time, until a stable state is achieved. Almost always, the critical power in the reversed direction is smaller than in the forward one. The presence of a large gap between the two critical powers may imply hysteresis of the stability boundary. However, that is not always the case: in the unstable regime, temperatures in the system increase due to acoustically enhanced heat transfer, leading to a change in the eigen mode properties and the mass flow rate. Hence the forward and reverse paths may correspond to different mass flow rates. Also, errors in the mass flow rate and power must be taken into account, since they can overlap the gap between those two

critical powers. Therefore, only by plotting the critical points with error bars on the power-mass flow rate diagram is it possible to determine whether hysteresis is present.

For each power step, a time-resolved measurement of the pressure (at two points), temperature (at fifteen points), a mass flow rate and a supplied power are recorded and filtered using a fifth-order Butterworth high-pass filter with a cutoff frequency of 20 Hz, to eliminate low frequency noise and environmental effects. The data files with recorded data are post-processed using a set of computer programs written in MATLAB environment. The examples of the pressure, power and mass flow rate fluctuations in time and the temperature profile along the tube centerline are given in Figures 2-3, 2-4, and 2-5.

The first case (Figure 2-3) corresponds to heater position  $x/L = 1/4$ , mean mass flow rate 3.35 gm/sec, and mean power delivered to the grid 956 W. The power values shown in the figure are larger since some fraction of power is lost in the feeding rods, and this loss is not subtracted from the full power depicted. Pressure signals from two transducers located in the upstream and downstream tube sections demonstrate a noisy character. It means that the system is in the stable state, and no sound is observed during the test at this system condition. The power signal possesses a low frequency component imposed on a pure noise. The presence of this oscillation is related to the AC/DC power supply system and the action of the power controller (Poncica 1998). The air flow rate fluctuations are attributed to the blower properties. The centerline temperature profile manifests a discontinuity at the heater location  $x = 25$  cm. The temperature field is not uniform in both cold and hot tube sections due to heat exchange between air flow and tube walls and power rods. The temperature profile exhibits non-monotonic behavior downstream the heater, which may be caused by transverse non-uniformity of the temperature field induced by recirculation zones behind the heating element and natural convection from the grid.

The temperature jump in the air flow at the heater location, as well as the temperature variation along the hot section, is comparable with the absolute temperatures of the system. That could lead to significant modification in the characteristics of the eigen acoustic modes, and hence affect

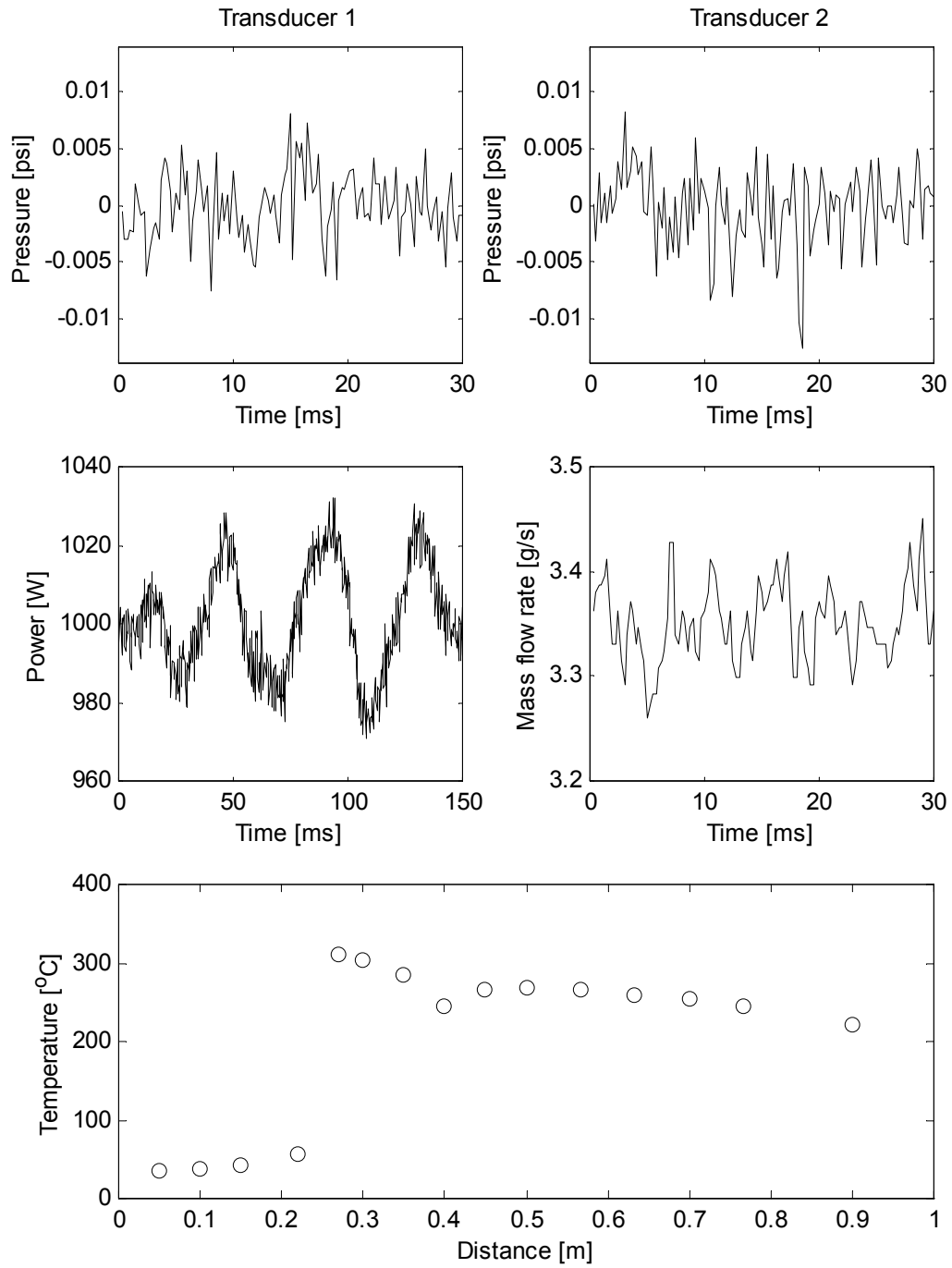


**Figure 2-3: Steady state recordings on the Rijke tube ( $x/L = 1/4$ ; stable case).**

system stability properties. Therefore, the measured non-uniform temperature profile shows the necessity for the heat transfer analysis when the system stability is to be calculated.

The second case, shown in Figure 2-4, corresponds to heater position  $x/L = 1/4$ , mean mass flow rate 3.08 gm/sec, and mean power delivered to the grid 1094 W. Notice that the difference in system parameters from those of the first case is only about 10%. However, the pressure perturbations recorded are drastically different. The pressure fluctuates with high amplitude, and the signals from both transducers have a regular shape with little variation from cycle to cycle. The system is in the unstable regime now with an excited eigen acoustic mode, and during the test a loud sound is heard. The pressure magnitude captured by transducer 2 exceeds that of transducer 1, because the second transducer appears to be positioned closer to the pressure anti-node. Sound waves in the tube affect heat transfer at the heater and modify recorded power variation in time. Despite the fact that the damping chamber is introduced between the tube and the flow meter, the oscillation of the measured air flow rate is noticeable and has the same frequency as pressure fluctuation. The temperature profile is qualitatively similar to that in the stable case. The overall temperature is greater due to higher power delivered and possible modification of the heat transfer rate due to presence of intensive oscillations in the flow.

The third case, shown in Figure 2-5, corresponds to heater position  $x/L = 5/8$ , mean mass flow rate 2.40 gm/sec, and mean power delivered to the grid 718 W. The system is unstable at this condition; however, different from the previous case, the heater is located in the downstream part of the tube. It is known from the earliest experiments on Rijke devices that excitation of the first mode becomes impossible at this heater position. Nevertheless, some investigators (Marone and Tarakanovskii 1967, Collyer and Ayres 1972) demonstrated the possibility of making the system unstable by exciting the second mode in this case. In our experiment, we observed the same phenomenon. The dominant frequency of pressure fluctuation is roughly twice that corresponding to the heater location at  $x/L = 1/4$ . The amplitude of the second mode and signal-to-noise ratio is lower, implying that the instability is less encouraged. Fluctuating components in the power

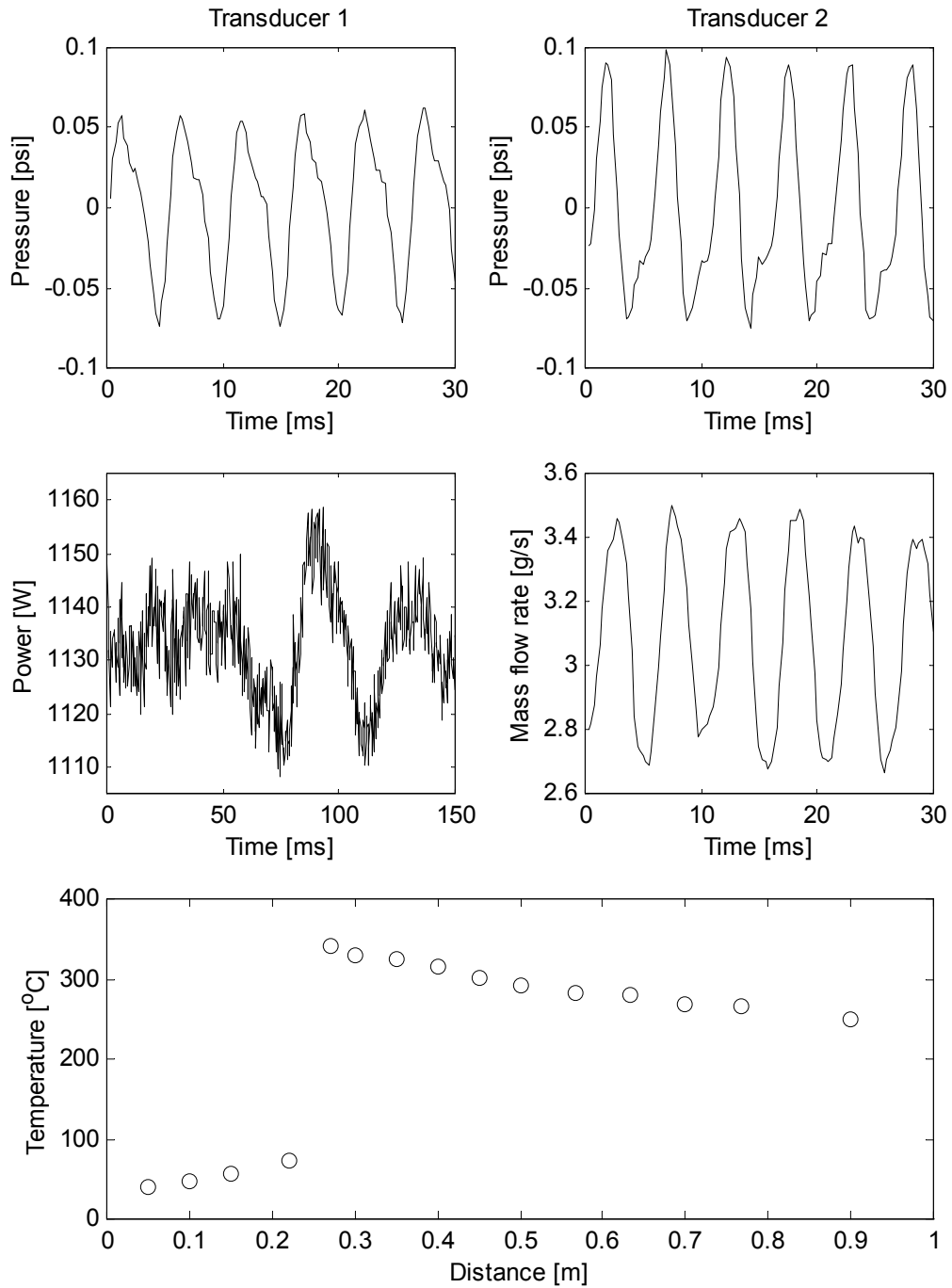


**Figure 2-4: Steady state recordings on the Rijke tube ( $x/L = 1/4$ ; excited case).**

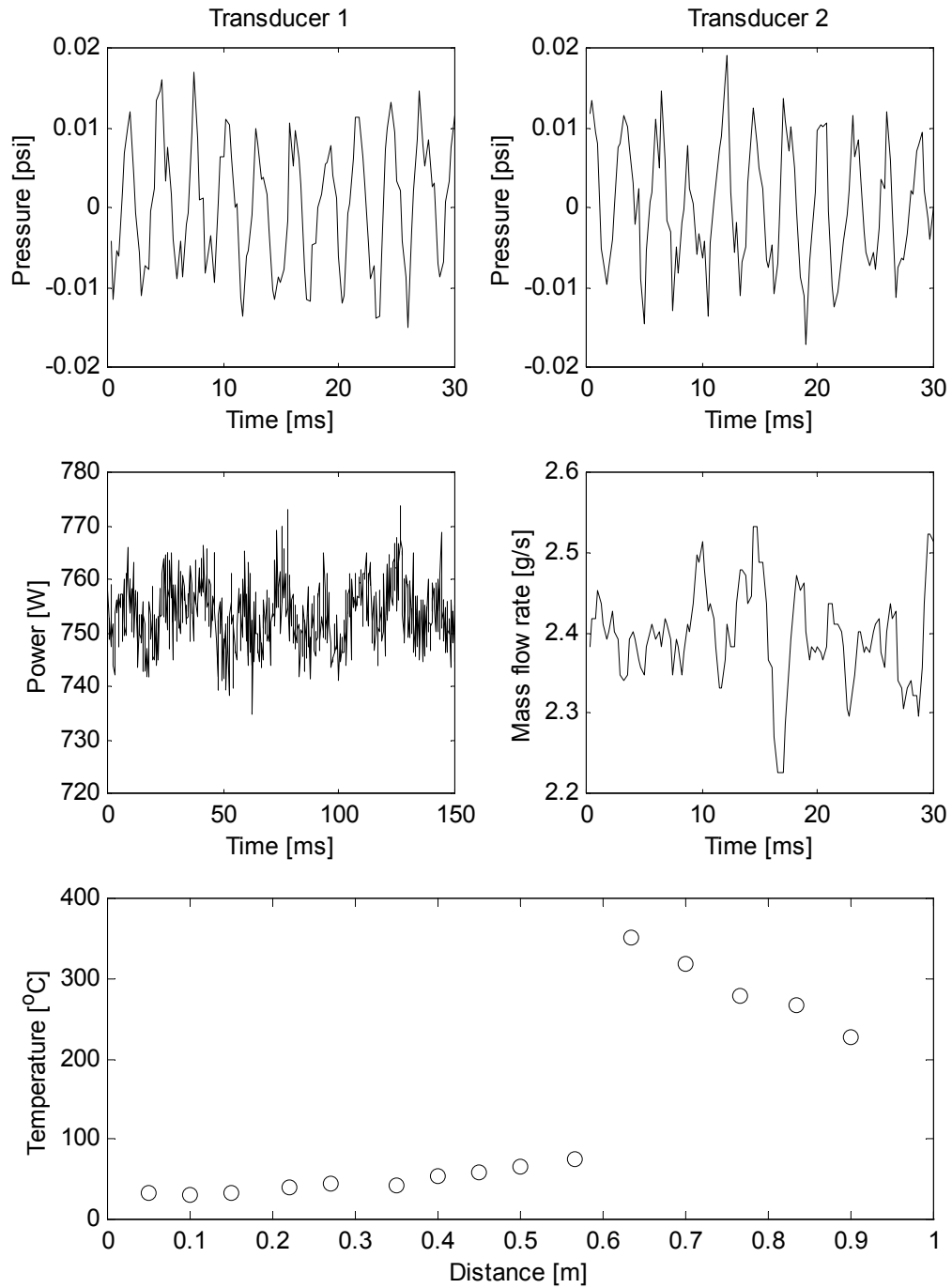


**Figure 2-5: Steady state recordings on the Rijke tube ( $x/L = 5/8$ ; excited case).**



supplied and the mass flow rate have the frequency of the pressure oscillation. The temperature profile is modified according to the displacement of the heating element; a jump is observed at  $x/L = 5/8$ .

Transition to instability of the Rijke tube, as well as its excited regimes of operation, are characterized by the appearance of limit cycles. The properties of limit cycles, namely, amplitudes and frequencies of the excited modes, can be found from information for the spectral content of the pressure signals. With a module available in MATLAB, Fast Fourier transform (FFT) analysis is used to generate the spectra. The power spectra of pressure signals, recorded by Transducer 1, are shown in Figure 2-6 for the considered cases; the vertical axis scale is arbitrary. The spectrum in Figure 2-6a corresponds to the stable state, shown in Figure 2-3. A typical noisy spectrum is observed with a small peak near the low frequency induced by the specificity of the power controller action. Figure 2-6b demonstrates the spectrum of the unstable state (as in Figure 2-4). The main peak corresponds to the excited first mode of the tube; other peaks of smaller magnitude show that higher harmonics of the first mode are present in the signal. When the heater is positioned in the downstream half of the tube, the second mode is responsible for instability with frequency about 360 Hz (Figures 2-6c and 2-5). The harmonic of this mode at twice the frequency is barely noticeable. The exact numbers for the amplitude and the frequency of the excited modes and their harmonics are reported in the next section where the limit cycles are analyzed.

In spite of the convenience of the FFT, this procedure modifies the signal properties, giving rise to the three pitfalls of the FFT, which are aliasing, leakage, and “picket fence” effect (Randall 1998). The first issue appears when there are significant signal components of the frequency above half the sampling frequency. The second problem is due to non-integral number of periods in the finite length records, so the power in a single-frequency component leaks into adjacent bands. The third effect results in a non-uniform frequency-weighting corresponding to a set of overlapping filter characteristics. In our case, the first two problems are not important for two

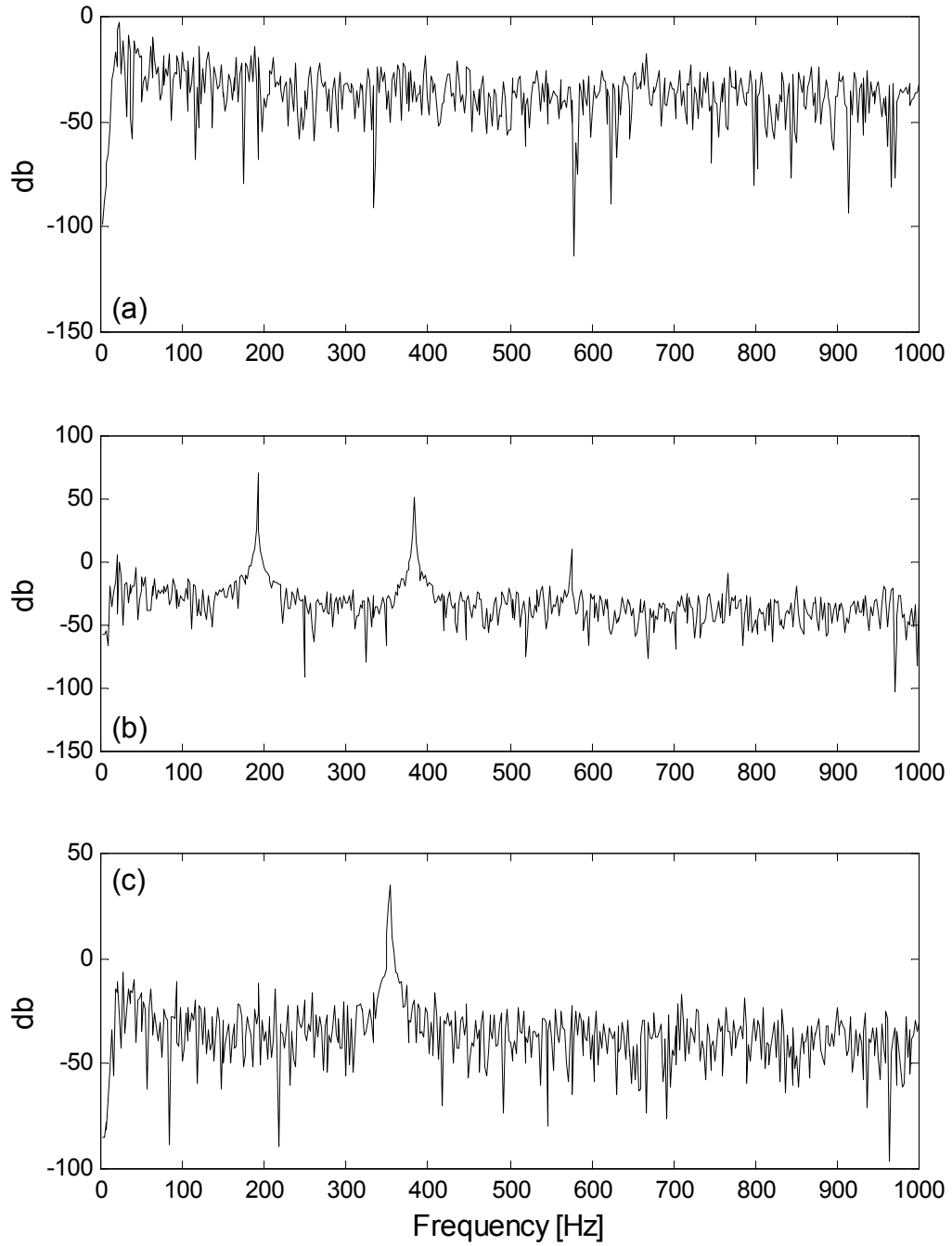


**Figure 2-6: Power spectra of pressure signals: (a) heater location  $x/L = 1/4$ , supplied power 956 W, mass flow rate 3.35 g/s; (b)  $x/L = 1/4$ , 1094 W, 3.08 g/s; (c)  $x/L = 5/8$ , 718 W, 2.40 g/s.**

reasons: first, there are no significant components in the signal of frequencies exceeding half the sampling frequency; and second, the number of periods in the recorded interval is so high that the leakage error is negligible. The “picket fence” effect, however, can greatly affect the post-processing data analysis, and special measures must be implemented in order not to lose the accuracy. We applied the recommendations of Jain et al. (1979) to determine the actual amplitude and the frequency of the excited harmonic. Let the two highest amplitudes, located next to each other in the spectrum, have amplitudes  $A_p$  and  $A_{p'}$ , and frequency scales  $p$  and  $p'$ . Then the exact harmonic frequency  $f$  and amplitude  $A$  are

$$(2-1) \quad f = \frac{A_p p + A_{p'} p'}{A_p + A_{p'}},$$

$$(2-2) \quad A = \max(A_p; A_{p'}) \frac{\pi f_d}{\sin(\pi f_d)},$$

where  $f_d = \min(A_p; A_{p'}) / (A_p + A_{p'})$ . The results for the amplitudes and frequencies of excited modes, given in the following sections, are calculated using Equations (2-1) and (2-2).

### 2.3 Stability boundaries for instability in the first mode

The primary goal of most investigations of Rijke devices is to determine the transition to instability as a function of the main system parameters. In this study we have the flexibility to vary three parameters: heater location, mass flow rate and power supplied to the heating element. The procedure for localizing the transition to instability is specified in the previous section: for the fixed heater location and the mass flow rate, the power is varied until the transition to instability is achieved. Figures 2-7 and 2-8 demonstrate the examples of such experimental runs for heater location  $x/L = 1/4$  and mass flow rates (a) 0.89 gm/sec, (b) 2.25 gm/sec, and (c) 3.15

gm/sec. The values of a mass flow rate are chosen to show different patterns of transitions between stable and excited regimes of operation of the Rijke tube.

RMS of the pressure fluctuation recorded by Transducer 1 is given versus the power delivered to the gauze in Figure 2-7. Dominant frequency in the signal within the interval near the first-mode natural frequency is presented in Figure 2-8. The changes in both RMS magnitudes and dominant frequencies determine the appearance of instability; the frequency also identifies which mode is unstable. As soon as the system transits to the excited regime, the magnitude of the pressure fluctuation significantly increases and the dominant frequency stabilizes at a certain level.

In case (a), typical for low flow rates, a noticeable sound is generated when the supplied power, varied in increasing manner, reaches a certain value. The transition, however, is not abrupt and not very well defined. At this particular flow rate, there is a power range, from 165 to 172 W, where a tone may appear and disappear, and beating in sound is heard. Recorded pressure fluctuation magnitudes at this transitional power range correspond to some arbitrary captured states. When the power exceeds 172 W, the sound does not disappear anymore, i.e., the system is in an excited state. On the way back, when the supplied power is decreased, the situation is similar; after a transitional regime the tone vanishes, hence, the system reaches a stable state.

At moderate flow rates, such as corresponding to case (b), the transitional process changes. When increasing power reaches a certain critical value, a stable tone of noticeable intensity abruptly appears. No intermediate ill-defined regimes are observed. With subsequent increase of power, the magnitude of the pressure fluctuation slowly increases. During the opposite (decreasing) variation of power, the system, going from an excited state, bypasses the critical value corresponding to the direct power variation without disappearance of the sound. The magnitude of the pressure signal decreases, and when another certain value of the power is achieved, abrupt transition from the excited to the stable state of the system occurs. Thus, the dependence of the critical power on the system history is observed. However, we cannot yet

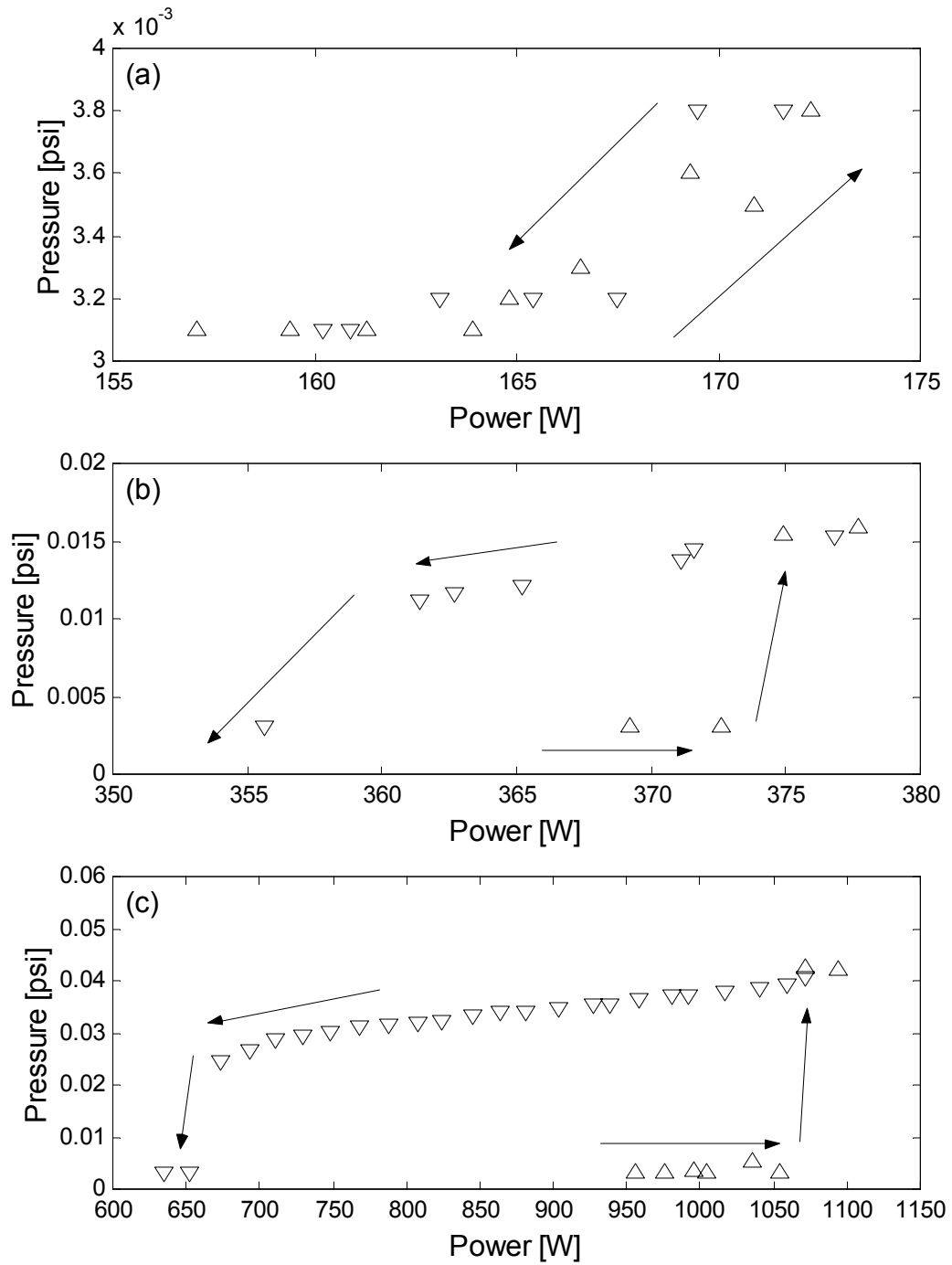


**Figure 2-7: RMS of pressure oscillation near the stability boundary:  $\Delta$ , power increase;  $\nabla$ , power decrease. Mass flow rate: (a) 0.89 g/s; (b) 2.25 g/s; (c) 3.15 g/s.**

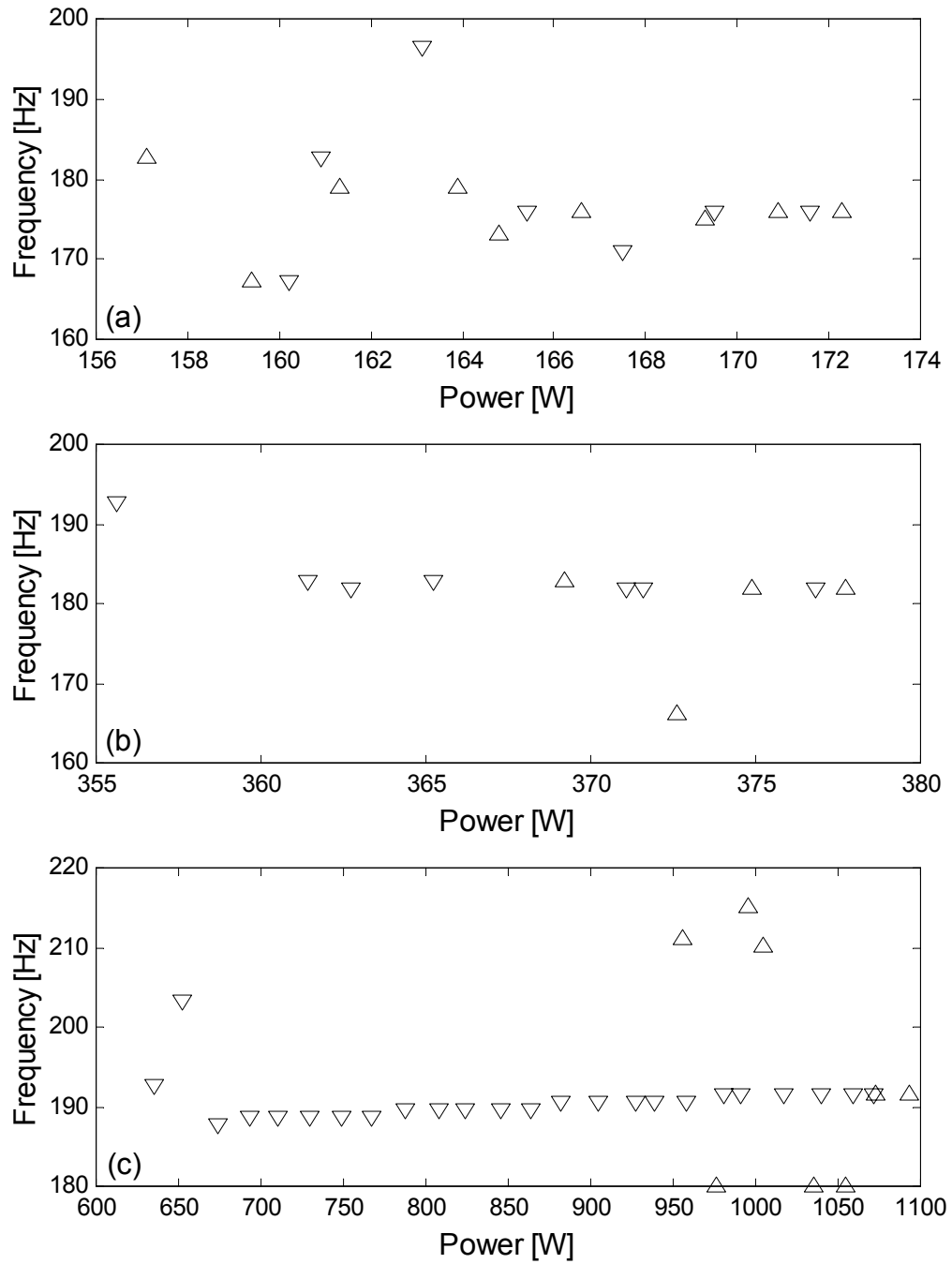


**Figure 2-8: Dominant frequency of pressure oscillation near the stability boundary:  $\Delta$ , power increase;  $\nabla$ , power decrease. Mass flow rate: (a) 0.89 g/s; (b) 2.25 g/s; (c) 3.15 g/s.**

judge whether this effect is a real hysteresis, i.e., when a system state at the same set of the basic parameters is not unique. The mass flow rate on the way back may be different, and intrinsic fluctuations of the power and the mass flow rate can overlap this gap between critical pairs of power and flow rate.

At high mass flow rates, as in case (c), the hysteresis loop is much more pronounced. The difference in the critical powers is comparable with the absolute power values. The qualitative pattern of the pressure dependence on the power variation is similar to case (b), although the magnitude of the signal is much bigger in the excited regime. The presence of the profound hysteresis at high mass flow rates testifies that two different system states, stable and excited, can exist at the same values of the main system parameters, and the choice of a particular state depends on the direction of parameter variations. Some kind of hysteresis in Rijke tubes has been mentioned in theses by Heckl (1985) and Poncia (1998); however, no papers with quantified data have followed these observations. The first documented results with regard to this phenomenon are presented and explained by the author (Matveev and Culick 2002 a,b,e).

Experimental runs aimed at finding the stability boundary, similar to the discussed above, are carried out for a set of mass flow rates, producing data on the transition to instability for three heater positions:  $1/4$ ,  $1/8$  and  $5/8$  of the tube length from the upstream end of the tube. The critical values of the system parameters are determined with experimental errors that are the maxima between the intrinsic variations of the parameters and the size of the intermediate regimes, such as discussed with regard to Figure 2-7a.

The cumulative data of the stability boundary for three heater locations are presented in Figures 2-9, 2-10, and 2-11. Both directions of power variation are studied. The results corresponding to the power increase are shown in bold lines; the results obtained for power decrease are represented by thin lines. In the first two cases, it is the first acoustic mode of the tube that is responsible for instability, in the last case – the second mode. The general shape of the stability curves of the Rijke tube is in accordance with previous investigations, e.g., by Marone and

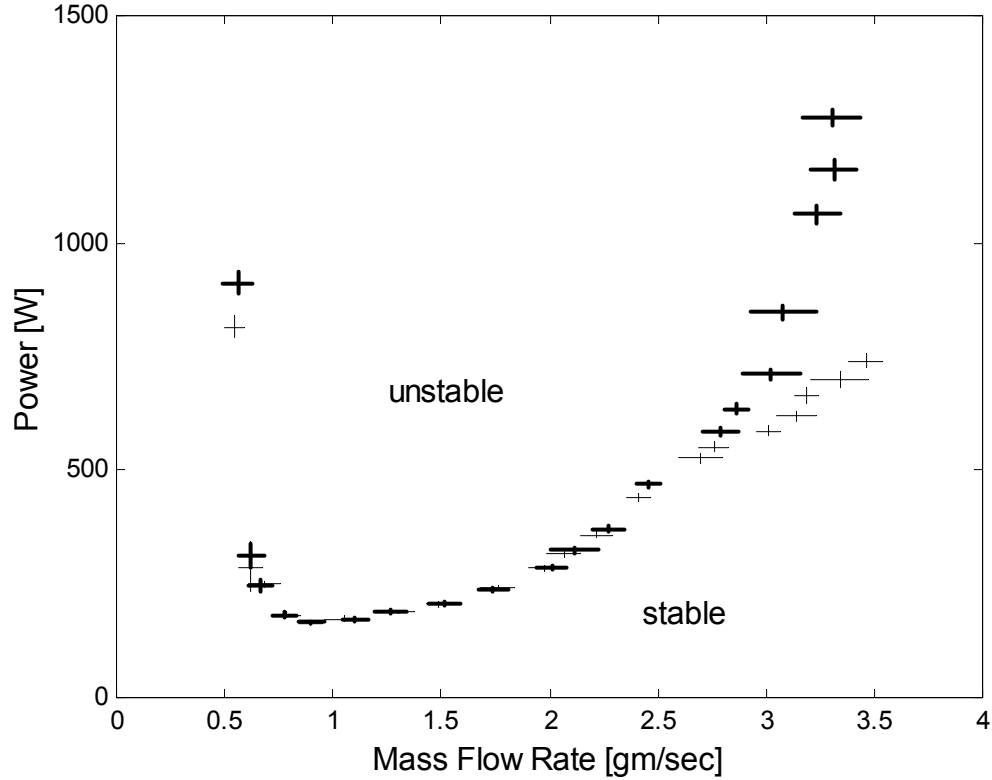


**Figure 2-9: Transition to instability for heater location  $x/L = 1/4$ .**

Tarakanovskii (1967), Katto and Sajiki (1977). The sizes of the crosses depicted are equal to experimental errors.

The location of the heater at  $x/L = 1/4$  (Figure 2-9) is close to the most favorable situation for initiation of the thermoacoustic instability, as Rijke noticed in the first experiments on this device. The dependence of the critical power, defining the transition between stable and excited regimes, on the mass flow rate has a distorted parabolic shape. At very low and high mass flow rates, this stability boundary goes steeply upward. In our system the maximally achievable power is about 1300 W, and the extreme flow rate limits (for instability to be seen) are about 0.5 and 3.5 gm/sec. A minimum value of the power needed to make the system unstable (near 160 W) is achieved at a mass flow rate around 0.9 gm/sec. The left wing of the stability curve grows steeply, while the right wing starts from gentle sloping followed by a steep curve. As we will see later, peculiarities



of the stability boundary shape greatly depend on the heat transfer processes in the system that affect properties of the acoustic modes and the thermal power released to the air flowing through the heater.

The experimental error bars have a tendency to increase with increasing mass flow rate and power. However, the relative noise component in the mass flow rate is generally greater at lower flow rates than at higher ones. That can be explained by the increasing importance of both air leakage in the system, e.g., via micro slits in the damping chamber, and the influence of incoming flow disturbances.

At flow rates exceeding 2.8 gm/sec, the stability boundary splits into two branches; one corresponds to increasing power variation, the other to decreasing power. This is a manifestation of the hysteresis effect. The higher the mass flow rate, the stronger is hysteresis. At moderate and low flow rates, the size of hysteresis loops is within the error bars, hence we cannot declare whether the hysteresis effect exists. Even if it does, hysteresis is small at these regimes. At the lowest recording we see that critical values are different for opposite variations of the power. However, since the stability curve is nearly vertical, this gap lies inside experimental errors, and hysteresis cannot be claimed there either.

From the experimental results, we could assume that the transition to instability at moderate flow rates is caused by linear system instability with a possible minor influence from nonlinear effects. Hysteresis is definitely a nonlinear phenomenon, and its explanation requires careful consideration of important nonlinear mechanisms.

Let us now consider the stability boundary obtained for heater position  $x/L = 1/8$  (Figure 2-10). From previous investigations, e.g., by Marone and Tarakanovskii (1967), we know that both the first and the second eigen acoustic modes of a tube can be responsible for transition to instability. Since this position is less favorable for excitation of the first mode, and generally it is more difficult to excite the second mode (acoustic losses increase with frequency growth), we can expect the stability boundary to move in the upward direction. Experiments do show this

tendency: the limiting mass flow rates are about 0.8 and 2.8 gm/sec, and the minimally achievable power needed to make the system unstable exceeds 200 W with the corresponding mass flow rates displaced to the right and equal to about 1.2 gm/sec.

The mode responsible for transition to instability in this case remains the first one. The second mode is still stable at this position of the heater; it is probably due to the relatively small length-to-diameter ratio of the tube, so the sound radiation losses from the open tube ends are too large for the second mode to dominate.

Although the hysteresis effect is observed during the tests at high mass flow rates, it is located in the region where the stability curve goes steeply upward, and is overlapped by the error bars. That does not allow us to claim unambiguously that hysteresis is present in this case.

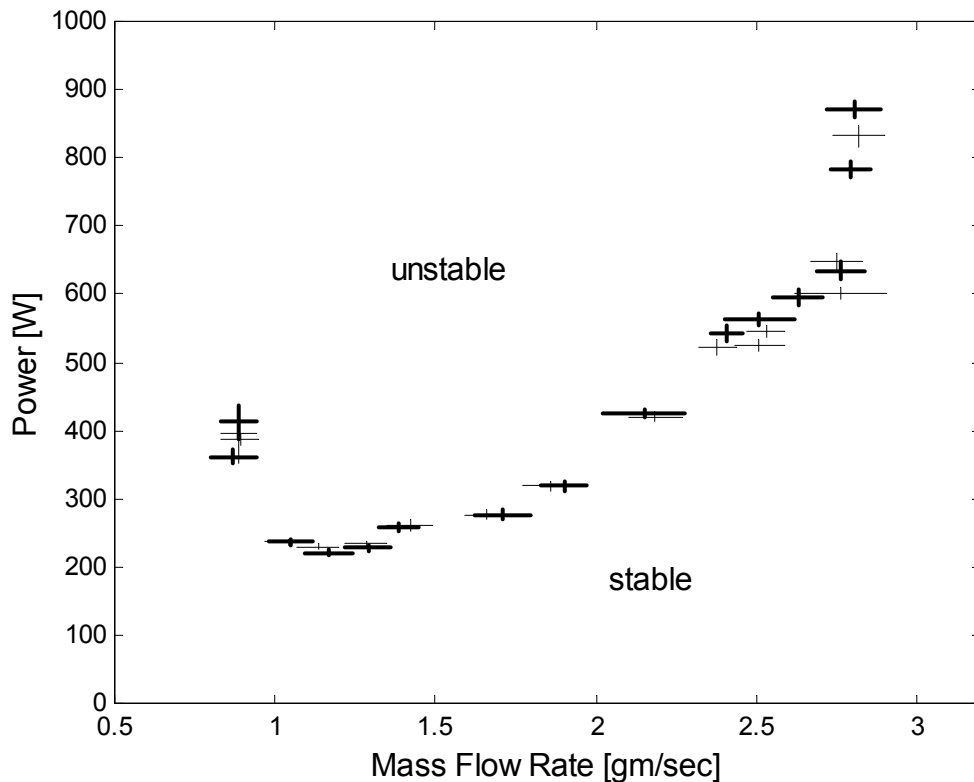


**Figure 2-10: Transition to instability for heater location  $x/L = 1/8$ .**

## 2.4 Stability boundary for instability in the second mode

To study Rijke oscillations in a broad spectrum of parameters and system states, it is highly desirable to be able to excite the system with a mode higher than the first one being responsible for instability. A heater location in the downstream section of the tube is not favorable for excitation of the first mode, and by positioning a heating element there, we intend to obtain the system instability in higher modes. A heater location is chosen to be  $5/8$  of the tube length; this point is known to be suitable for encouragement of the second mode development. However, during the tests no sound was generated at this condition in the accessible range of the power. The most likely reason is that acoustic losses are too large. To reduce them, we modified the damping chamber (Figure 2-1) by installing a rigid wall on the chamber internal back side; initially it was covered by a thick carpet as described in Section 2.1. We expected that the solid wall would decrease the absorption coefficient leading to reduction of total acoustic losses in the system. According to our expectations, the system did produce sound in this modified configuration, and it was the second mode that caused transition to instability.

The approach to localizing the stability boundary is similar to the preceding tests: for the fixed flow rate, the power is increased until the unstable state is discovered. The measured transition points with the appropriate experimental error bars are shown in Figure 2-11 for forward direction of power variation. A surprising distinction from the preceding runs is that the sound disappears when the power is further increased after transition to instability. Therefore, we are unable to produce the stability boundary corresponding to the reverse variation of the power; that is why only one set of data is given in Figure 2-11. The transition from the unstable to stable regimes for increasing power variation at high powers is not reported here; during the test we could not obtain a robust boundary.

Despite the reduction of acoustic losses in the system, the typical powers needed to obtain instability are greater than those shown in Figures 2-9 and 2-10. The possible reason is that the

losses increase significantly with a frequency, and since the second mode is excited, this factor makes the critical power to be high. Another reason may be due to different efficiency of conversion of thermal energy to acoustic energy, which also depends on frequency. However, within this study we did not measure thermoacoustic efficiency experimentally, and hence cannot judge this factor.

The extreme limits of mass flow rates, when instability is achievable, are about 1.6 and 2.6 gm/sec. The minimal power needed for excitation is around 650 W; the corresponding mass flow rate is 2.2 gm/sec. The stability boundary moves upward in the power-flow rate diagram, and contracts more in comparison with the cases when the heater is located in the upstream half of the tube. The shape of the stability boundary changes as well: a steeper branch is located on the right, and a gentle sloping is on the left from the minimum point.

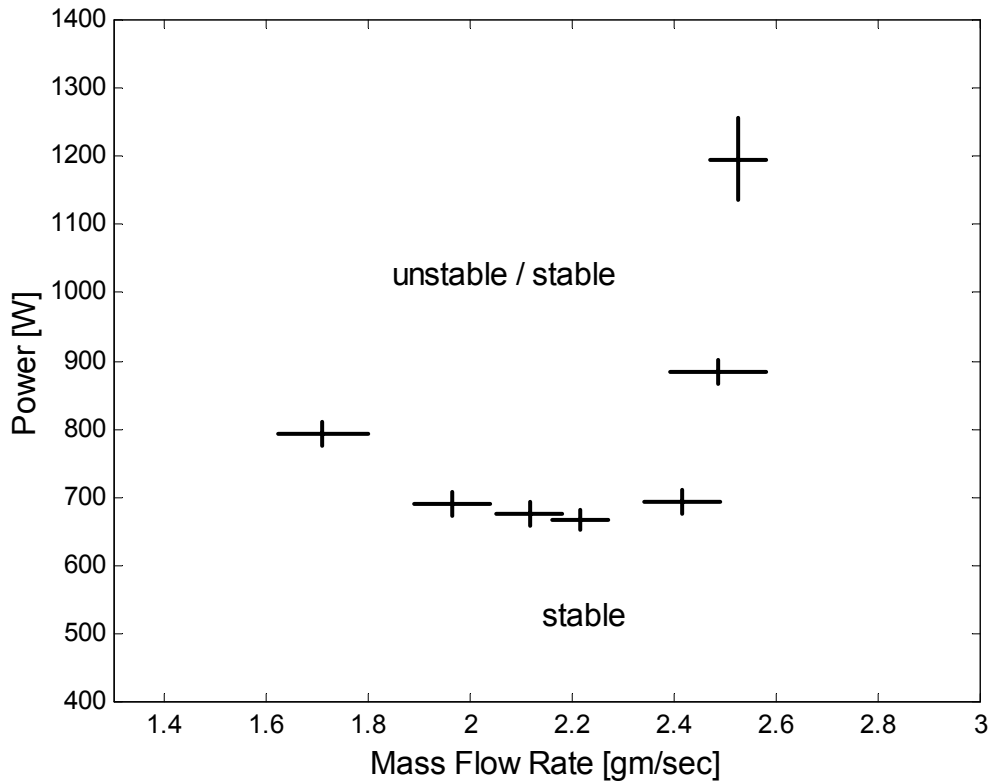


**Figure 2-11: Transition to instability for heater location  $x/L = 5/8$ .**

Besides information on the stability boundary in the main coordinates (heater location, flow rate, and supplied power), the properties of the acoustic modes in the transition between stable and excited regimes, such as a frequency and a growth rate, are of interest too, especially from the modeling point of view. These data would correspond to essentially transient processes. Test strategies, data acquisition and analysis must differ significantly from the procedures developed at this study, aimed at working with steady-state conditions. Therefore, we do not report here the information about growth rates, corresponding to the initial development of instability. Only experimentally and theoretically determined stability boundaries and steady state excited regimes are the subjects of this thesis; tests and modeling of the transient processes in the system can be investigated in a later work.

For illustrative purposes and qualitative comparison with linear modeling, information about the dominant frequencies in the pressure signals of the steady states obtained after transition to instability are reported in Figure 2-12. In cases (a) and (b), given for heater locations  $1/4$  and  $1/8$  of the tube length, the dominant frequency is around 180 Hz, corresponding to the first acoustic mode of the tube. In the third case (c) the heater is positioned at  $5/8$  of the tube length, and the second mode is dominant; a measured frequency is within 350–370 Hz interval. Noticeable data scattering is due to unequal deviation of the recorded system parameters from the actual stability boundary. The trends of the frequency apparent in Figure 2-12 are caused by variation of the characteristic temperature in the system. At high and low mass flow rates the power needed to excite the system is greater than that at the intermediate flow rate. The mean temperature correlates positively with the amount of power supplied; and the mode frequencies increase with the growth of characteristic temperatures.

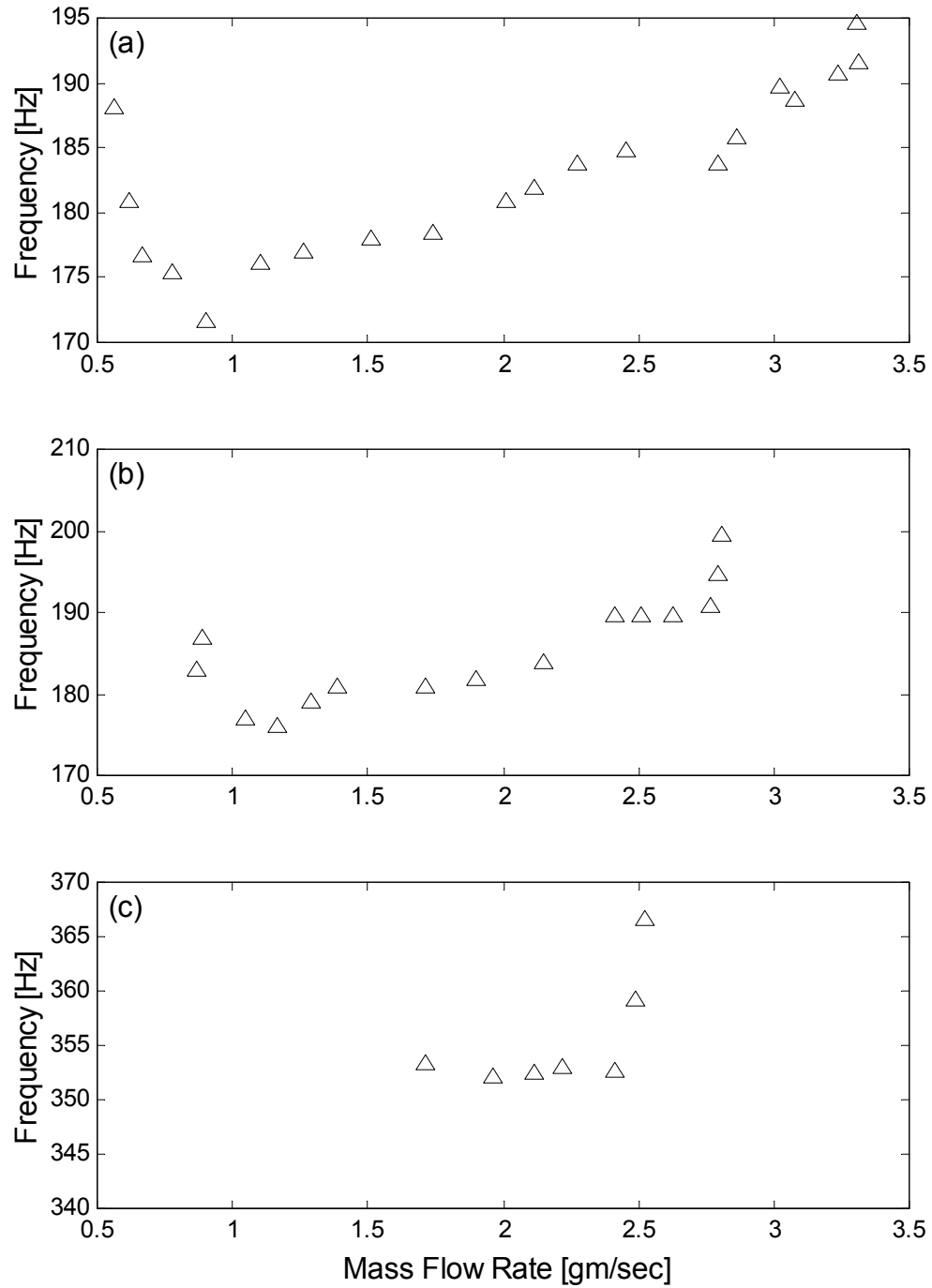


**Figure 2-12: Dominant frequency in the signal on transition to instability. Heater location: (a) 1/4; (b) 1/8; (c) 5/8 of the tube length.**

## 2.5 Limit cycles

This section is dedicated to experimental study of the excited regimes of operation of the Rijke tube. Since the Rijke tube behavior at heater location  $x/L = 1/8$  is qualitatively similar to that at  $x/L = 1/4$ , namely, the first mode is responsible for instability in both cases, we study the excited states only for two heater positions,  $1/4$  and  $5/8$  of the tube length, where different modes dominate in the unstable regime.

Recordings have been obtained for two fixed mass flow rates in both cases, and the power has been varied starting from the value, corresponding to the stable state near the stability boundary, to nearly 900 W. The signal generated at Transducer 1 is chosen for analysis, since thermal conditions near this sensor, located in the cold upstream tube section, vary much less than those at Transducer 2, where temperature changes in wide ranges for given power interval. By using the cold section sensor, an additional factor imposed by significant temperature variation is excluded.

When transition to instability was studied, the power was driven very slowly in order to obtain quasi-steady conditions. The duration of the experiment was acceptable, since only a small power interval in the vicinity of the stability boundary was studied. Investigating the unstable regimes, we want to cover much larger power ranges, so this quasi-steady procedure would lead to the unreasonable increase of test duration, hence it is not acceptable. We have to decrease the time between power increments. That inevitably produces some delay in the temperature field settling due to the system thermal inertia. The results for opposite directions of power variation will correspond, strictly speaking, to different conditions. However, the power is chosen to be varied with a moderate rate that produces only a small difference between these opposite variations. In any case, the accuracy of the results, obtained both experimentally and theoretically in this work for the excited regimes of operations of the Rijke tube, is accepted to be lower than the accuracy of the stability boundary. With regard to the limit cycles, we are mostly interested in understanding their properties and approximate modeling.

Pressure signals studied in this portion of the work are analyzed in accordance with the procedure explained in Section 2-2. Power spectra are obtained for steady state signals, and amplitudes and frequencies of the spectral peaks are calculated accounting for peculiarities of the FFT method. The noise component is subtracted from the amplitude values, so that in the stable state the intensity of the harmonics is zero. The results for the excited modes and their harmonics are presented in Figures 2-13 to 2-18. Filled markers correspond to the increase of the power supplied, empty markers – to the decrease of the power.

Figures 2-13 to 2-16 show the dependence of amplitudes and frequencies of the first mode (responsible for instability in this case) and its harmonics for the heater location  $x/L = 1/4$ . Appearance of higher harmonics can be explained by the fact that the velocity fluctuation with a finite amplitude inevitably produces higher harmonics in the heat release from the gauze due to a nonlinear law of the forced convective heat transfer. Another possible reason, nonlinear gas dynamics, is probably not important in our system, since the Mach numbers do not exceed  $10^{-3}$ ; at this value the nonlinear terms in a wave equation cannot generate higher harmonics of the amplitudes observed during the tests.

The amplitude of the first mode at mass flow rate 1.63 gm/sec has an increasing tendency with respect to the power supplied; this trend is more pronounced at lower power. In the high power range the amplitude's growth decelerates, since the fraction of a power that leaves from the gauze via thermal radiation increases at high temperatures, and hence the fraction of power transmitted to the air flow decreases. Irregularities in the recordings are probably related to the fluctuations in the main system parameters, which are larger in the high power range. The maximal intensity of the sound inside the tube is very high; at large supplied powers it exceeds 135 dB.

The amplitude of the first mode at the reverse power variation is generally lower than that at the power increase. This observation may relate to the system thermal inertia. The averaged temperatures in the air flow and especially in its portion in the hot tube section are higher during tests on the reversed path. That leads to the increase of the frequency and the larger distortion of



the mode shape (compared with a mode shape for constant temperature in the tube). The first effect enhances the acoustic losses, and the second effect displaces the mode from the most favorable distribution for thermoacoustic energy transformation.

The variation of the frequency of the first mode (Figure 2-14) is practically linear in the excited state. The frequency increases with the growth of the power, since temperatures and consequently the speed of sound increase. On the reverse path the frequency decreases for the same reason. The frequency value is higher during reversed power variation, due to the higher temperatures caused by the system thermal inertia.

Now let us look at the properties of the higher harmonics recorded at mass flow rate 1.63 gm/sec (Figures 2-13 and 2-14). The fact that these are harmonics of the first mode, but not the higher modes of the tube, follows from the frequency data. The spectral peaks are observed at the frequencies that are exactly integer multipliers of the first mode frequency. If there were higher modes excited, their frequencies in a non-uniform temperature environment would differ from the exact multipliers of the first mode frequency (though some mode frequencies would be close to those numbers).

From the figures presented, one can see that higher powers are required to generate higher harmonics. While the second harmonic is produced almost immediately after the excitation of the first mode, the power exceeding 300 W is needed for the appearance of the third harmonics, and over 700 W – for the fourth harmonic. The pattern of the harmonic amplitude dependencies on the supplied power is similar: initially, the amplitude is growing fast, reaching a maximum; then, it recedes and stabilizes at a certain level. During reversed power variation, amplitudes of the harmonics are lower than those on the way forward, similar to the first mode behavior.

Regarding values of the harmonic amplitudes with respect to that of the first mode, one can notice that in the regime from 200 to 400 W, the amplitude of the second harmonic is only about 30% less, and at higher powers, it is 3-5 times smaller than the amplitude of the excited mode.

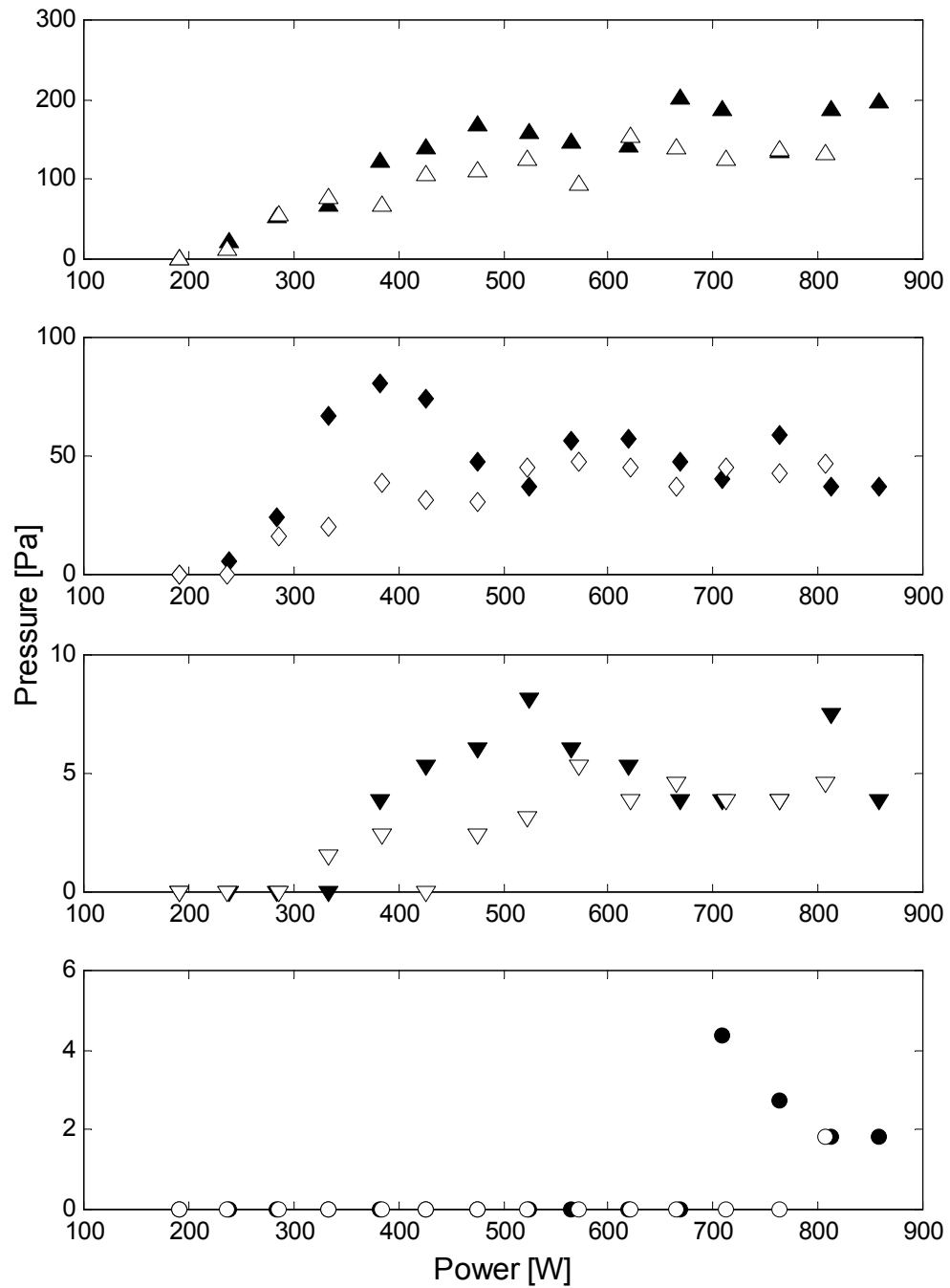


**Figure 2-13: Amplitudes of the excited mode and its harmonics of the Rijke tube in the unstable state. Mass flow rate 1.63 gm/sec;  $x/L = 1/4$ .  $\Delta$ , fundamental mode;  $\diamond$ , second harmonic;  $\nabla$ , third harmonic; o, fourth harmonic.**

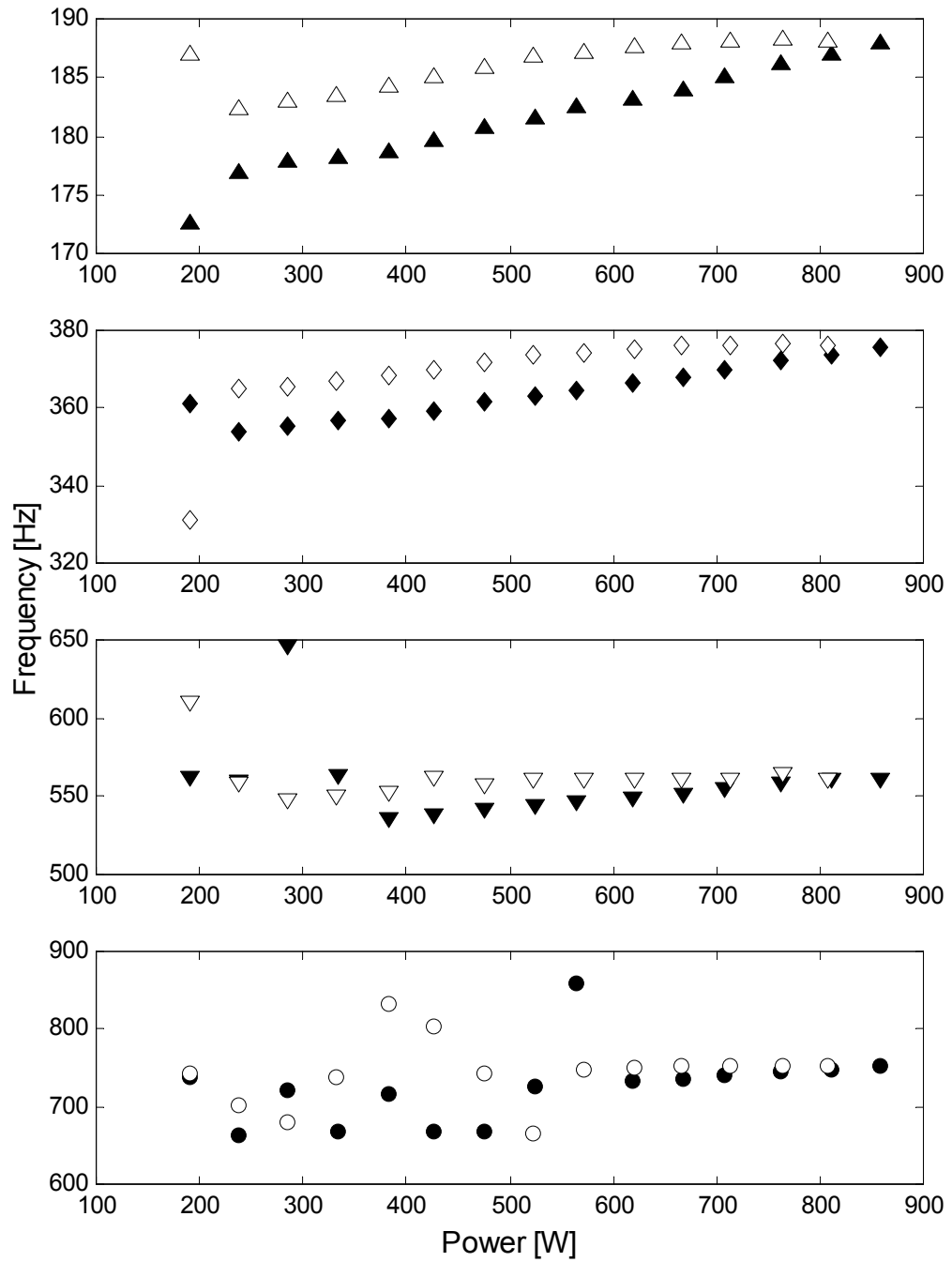


**Figure 2-14: Frequencies of the excited mode and its harmonics of the Rijke tube in the unstable state. Mass flow rate 1.63 gm/sec;  $x/L = 1/4$ .  $\Delta$ , fundamental mode;  $\diamond$ , second harmonic;  $\nabla$ , third harmonic;  $o$ , fourth harmonic.**

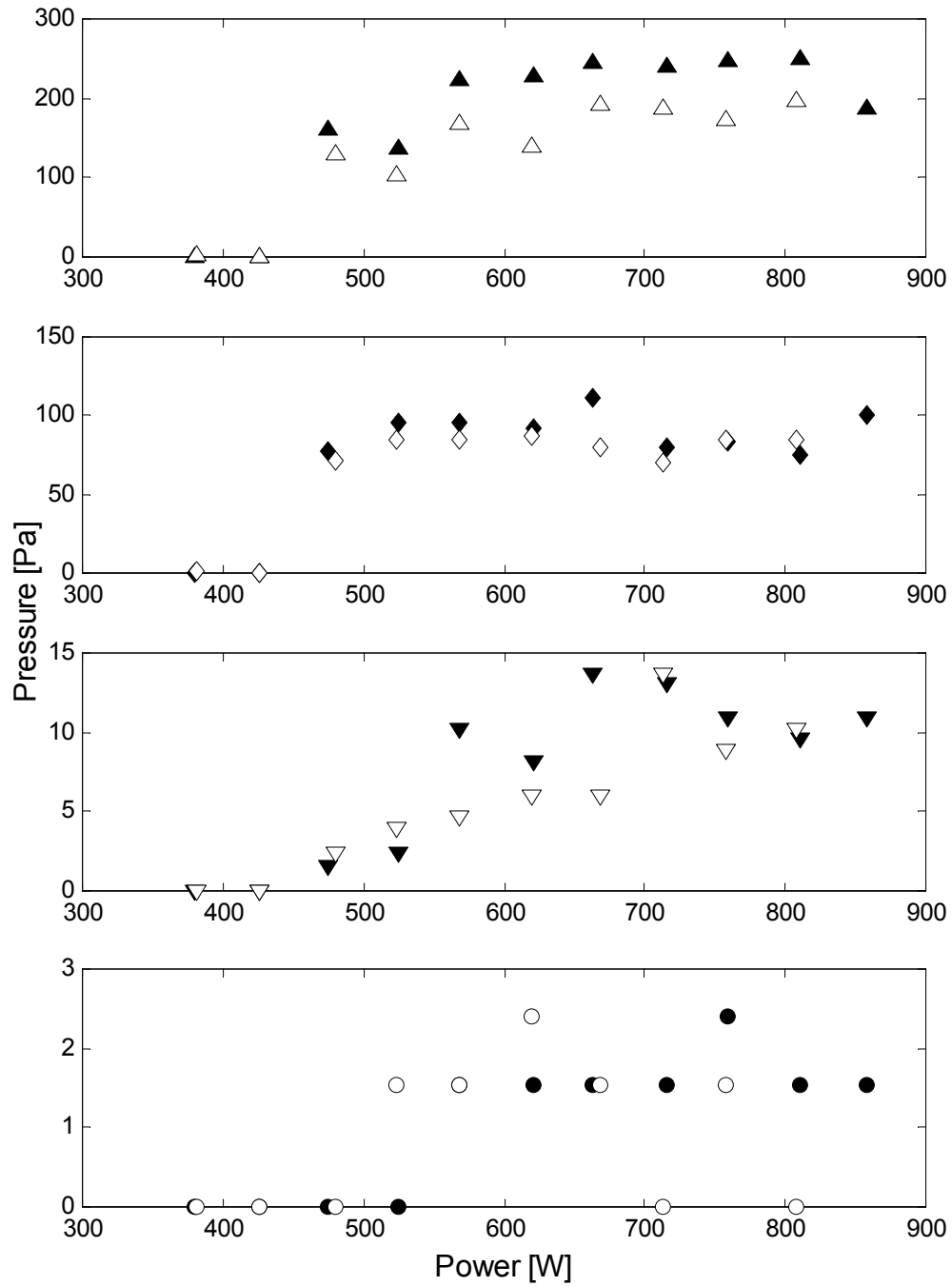


**Figure 2-15: Amplitudes of the excited mode and its harmonics of the Rijke tube in the unstable state. Mass flow rate 2.40 gm/sec;  $x/L = 1/4$ .  $\Delta$ , fundamental mode;  $\diamond$ , second harmonic;  $\nabla$ , third harmonic;  $\circ$ , fourth harmonic.**

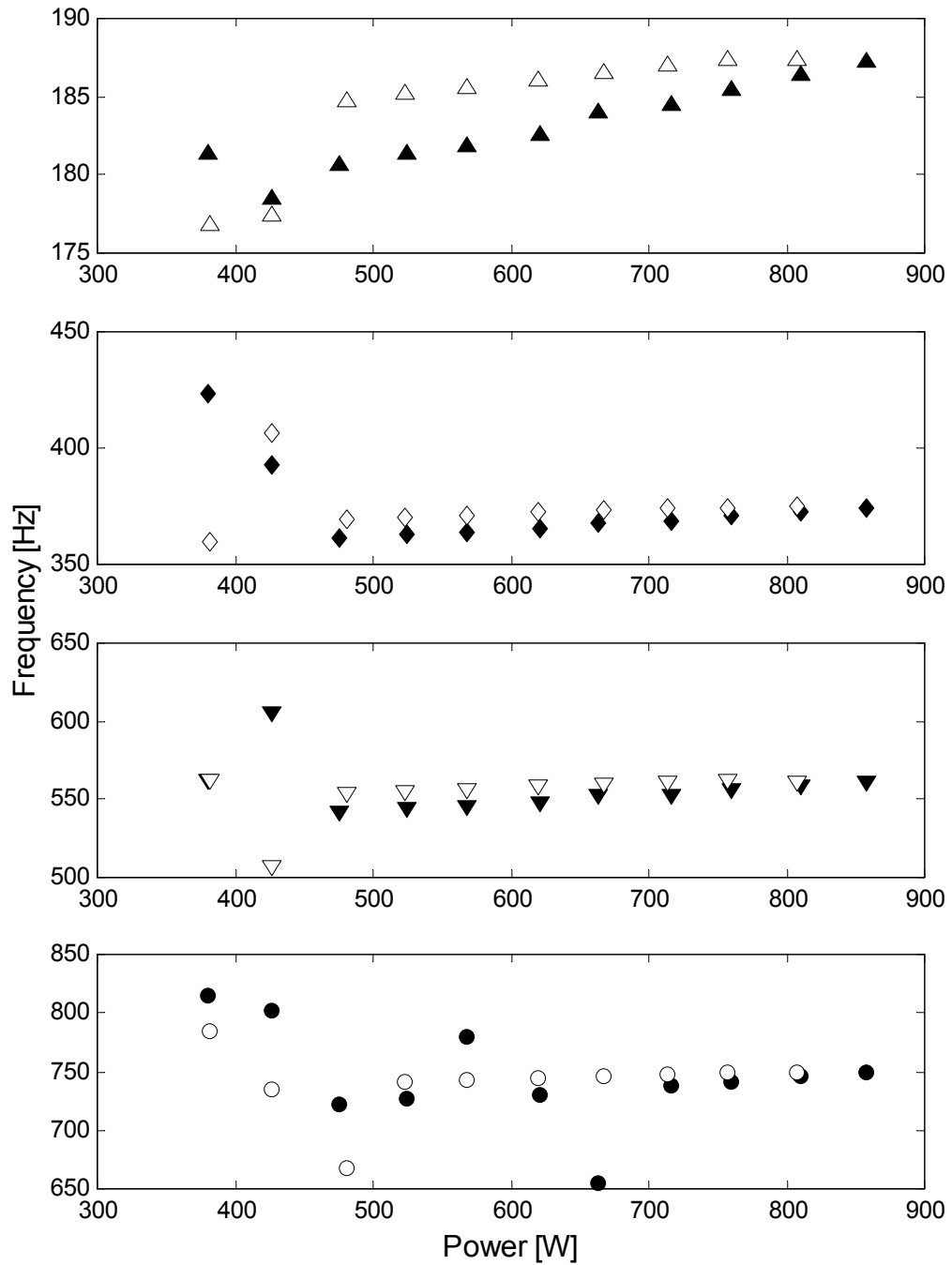


**Figure 2-16: Frequencies of the excited mode and its harmonics of the Rijke tube in the unstable state. Mass flow rate 2.40 gm/sec;  $x/L = 1/4$ .  $\Delta$ , fundamental mode;  $\diamond$ , second harmonic;  $\nabla$ , third harmonic;  $\circ$ , fourth harmonic.**

The third and the fourth harmonics reach only a small fraction of the second harmonic amplitude.

At mass flow rate 2.40 gm/sec (Figure 2-15 and 2-16), a pattern of the development of the first mode amplitude is somewhat different from the low flow rate case. The magnitude increases abruptly, and then changes insignificantly. This is similar to variation near the transition to instability discussed in the previous section. The absolute value of the amplitude is a few dB higher than that shown in Figure 2-13. The trend in frequency is similar to the previous case.

Behavior of the second and the fourth harmonic amplitudes also demonstrates initial abrupt increase and stabilization at a certain level; however, the development of the third harmonics is more complicated with some obvious regions of increased amplitude imposed on the otherwise linear dependence on power for both directions of power variation. Frequency data confirm again that the spectral peaks correspond to the harmonics of the excited modes, since their frequencies are the exact multipliers of the first mode frequency.

When the heater is moved to the downstream half of the tube ( $x/L = 5/8$ ), the second eigen acoustic mode of the tube is unstable. Higher losses associated with the increase of the frequency of the unstable mode require higher power to be delivered to the heating element, so the excited state in this case covers a smaller power range. The maximum level of power (900 W) is kept the same during these tests in order not to overheat the system components.

The stability boundary for this heater position is reported in the previous section with regard to only one direction of power variation, because sound is observed to disappear at higher power level. The additional goal of this section is to study how this effect occurs. The results for the amplitude and frequency of a dominant spectral component in the signal are shown in Figures 2-17 and 2-18 for two mass flow rates. Different from the case of heater location at 1/4 of the tube length, higher harmonics in the signal are not clearly recognizable from the background noise, and hence, are not reported here. The reason is again a smaller instability margin.

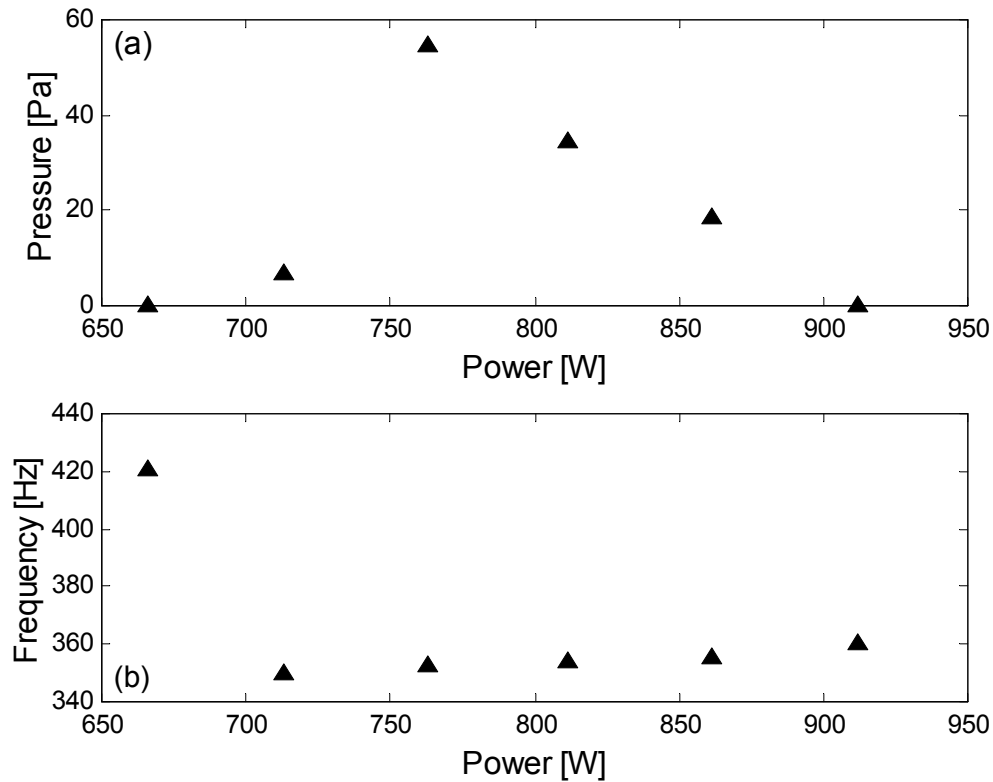


**Figure 2-17: Amplitude and frequency of the excited mode of the Rijke tube in the unstable state. Mass flow rate 2.05 gm/sec;  $x/L = 5/8$ .**

At mass flow rate 2.05 gm/sec, tone intensity grows steeply after crossing the stability boundary. There is an intermediate region similar to that observed in the transition to instability at low flow rates when heater location was  $x/L = 1/4$  (Figure 2-7). The maximum of the amplitude of the excited mode is recorded at power 760 W. It gradually recedes afterwards and eventually disappears at power near 900 W. The most likely reason for the transition to the stable regime at high powers is the distortion of the acoustic mode shape, so the maximally favorable heater position for excitation of the second tube mode displaces from the actual location of the heating element. Increase of the supplied power, as well as thermoacoustic power generation, cannot counteract this effect, since a significant portion of energy leaves the gauze via thermal radiation in the high power range. The behavior of the dominant frequency is similar to the previous case:

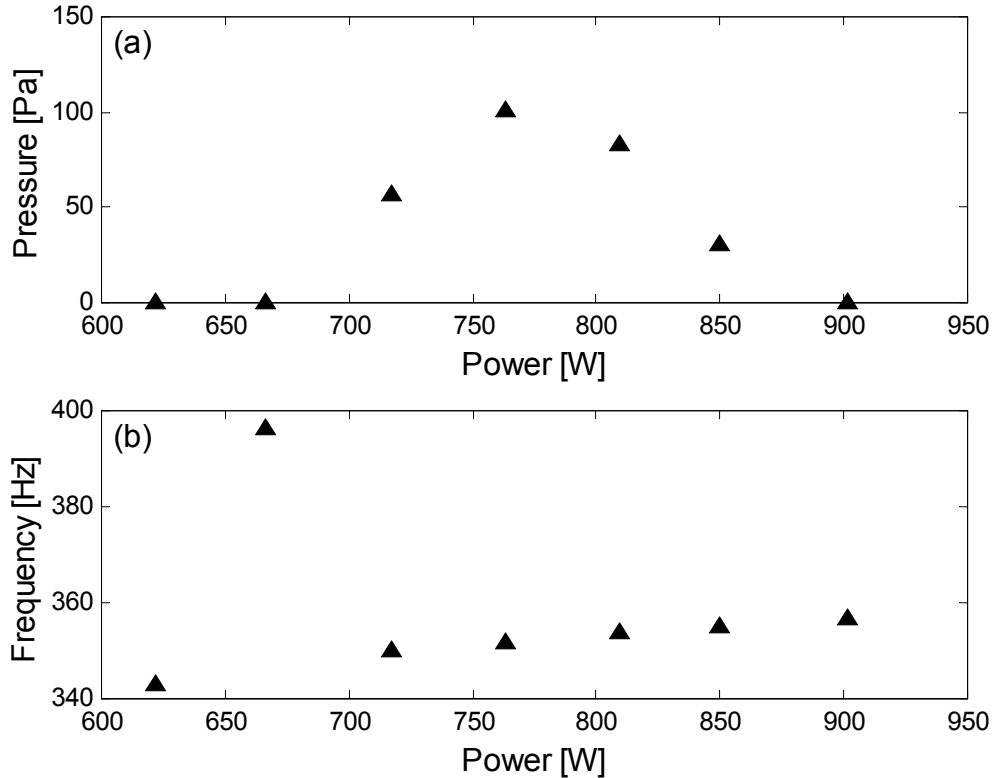


**Figure 2-18: Amplitude and frequency of the excited mode of the Rijke tube in the unstable state. Mass flow rate 2.21 gm/sec;  $x/L = 5/8$ .**

it increases with the growth of the power due to higher temperatures in the system.

Once sound disappears at a critical value of power (near 900 W), the tone is not produced either by increasing the power further or by decreasing it. That implies a strong history dependence, and a hysteresis loop in this case is quite different from that observed at the heater location  $x/L = 1/4$ . At higher mass flow rate, 2.21 gm/sec, the pattern is similar (Figure 2-18), although some details are different. Instability occurs earlier, and initially the tone intensity is growing with power. Then the mode amplitude reaches a maximum and starts declining. At power 900 W, the sound becomes unnoticeable. On the way back, no instability is observed either. The mode frequency increases monotonically versus power.



The non-trivial behavior of the properties of the excited modes and their harmonics, considered in this section, shows a complexity of the real system. The mathematical modeling intended to simulate the effects observed must be quite sophisticated to capture all these phenomena.

## 2.6 Summary of experimental results

A quasi-steady data acquisition procedure has been established to generate temporally and spatially resolved measurements of the properties of the Rijke tube. An iterative method has been employed to determine the transition to instability as a function of the primary system parameters. Stability boundaries were documented with specified uncertainties in the system parameters for three heater locations:  $x/L = 1/4$ ,  $x/L = 1/8$ , and  $x/L = 5/8$ . In the first two cases, it was found that the first acoustic mode caused transition to instability. In the third case, it was the second mode that became unstable. A hysteresis in the stability boundary was discovered for sufficiently high mass flow rates for the heater at location  $x/L = 1/4$ , and for all flow rates at  $x/L = 5/8$ . A significant non-uniformity in the temperature field inside the tube was observed for all system conditions (except those without power input). The properties of the limit cycles for the unstable regimes of operation of the Rijke tube were determined as functions of the main system parameters. At steady-state conditions, spectra of the acoustic signal clearly exhibited a major peak corresponding to the unstable eigen mode, as well as minor peaks at higher frequencies associated with higher harmonics of the self-excited mode. At heater locations  $x/L = 1/4$  and  $x/L = 1/8$ , the limit-cycle amplitudes and frequencies have shown tendency to grow with increasing input power. At  $x/L = 5/8$  the limit cycles disappear upon reaching a sufficiently high power, and the system transits to a stable state.

## Chapter 3

# Simplified Modeling

### 3.1 Objectives and assumptions

Two major objectives of analyses of Rijke oscillations are to determine a stability boundary as a function of main system parameters, and to model the excited regimes of operation, the limit cycles. In this chapter, we develop a simplified theory aimed at the first objective only; the second goal requires a nonlinear theory and will be a subject of Chapter 6.

Simplified modeling is carried out similar to previous investigations reviewed in Chapter 1. By comparing numerical results with experimental data, we will discuss characteristics of the stability boundary, judge the accuracy of a simplified approach and establish directions for theory developing aimed at achieving more accurate results. The geometry of the system to be modeled is shown in Figure 3-1. It is essentially a pipe open at both ends with a mean flow and a concentrated heat source. Although in our system a damping chamber is attached to the downstream tube end (Figure 2-1), its influence is ignored in simplified modeling. Typical assumptions, applied to reduce mathematical complexity of the modeling, are the following:

- (a) All time-averaged properties of an air flow are treated as constants along the tube. This variant of approximation is applied when the heat exchange between an air flow and tube walls is so high, that hot air, which crosses the heater, cools down very effectively, and the temperature along the entire tube can be roughly considered equal to the room temperature. Another variant of this assumption is to consider a step-like temperature field (with a jump at the heater). However, it is more valid in Rijke burners where a temperature jump is much bigger than that in the systems with an electric heater, as considered in this work. Therefore, we will assume for our simplest model that the temperature of air is constant along the entire tube and equal to  $T = 300 \text{ K}$ .
- (b) All heat released at the heater is transmitted to the air flow. That means that thermal radiation and losses through heat conduction to other structural elements, e.g., tube walls, are ignored.
- (c) Gas flow is one-dimensional, and a pressure drop over the tube is negligible.
- (d) Oscillations are small in amplitude, allowing us to consider only linear effects.
- (e) Disturbances to the acoustic oscillations are small, so that both thermoacoustic energy input and acoustic losses do not affect the mode shapes. Also, sinusoidal dependence of oscillations on time is assumed.
- (f) The thickness of the heat source is small compared to the acoustic wavelength. The source plane can be treated as discontinuity between two tube sections.
- (g) Gravity and other body forces are neglected.
- (h) Gas flow speed is small compared to the speed of sound.

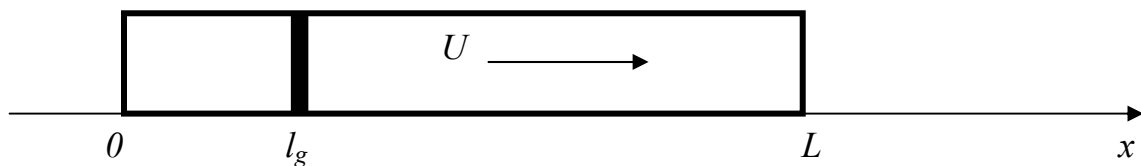


**Figure 3-1: One-dimensional Rijke tube with a concentrated heat source.**

### 3.2 Analysis

Since disturbances are assumed to be small, and the system properties are uniform, eigen acoustic modes are uncoupled. The system stability is determined by stability of individual modes: if any of the modes is unstable, then the entire system is unstable. Acoustic losses grow significantly with a frequency, hence, consideration of only the lowest modes is sufficient.

In an undisturbed system and under assumptions stated, the homogeneous wave equation is valid for pressure fluctuations  $p'$ :

$$(3-1) \quad \frac{\partial^2 p'}{\partial t^2} - a^2 \frac{\partial^2 p'}{\partial x^2} = 0,$$

where  $a$  is the speed of sound. Boundary conditions at the open ends, accounting for the end correction, are

$$(3-2) \quad p'(-l_e, t) = p'(L + l_e, t) = 0,$$

where  $l_e \approx 0.61R$  is the end correction (Levine and Schwinger 1948). The effective tube radius  $R$  is related to the side  $D$  of a square tube cross section as  $R = D/\sqrt{\pi}$ . Solutions to the wave equation are eigen acoustic modes of the system. Pressure and velocity perturbations, corresponding to the  $n^{\text{th}}$  mode, are

$$(3-3) \quad p'_n = A_n e^{i\omega_n t} \sin(k_n x),$$

$$(3-4) \quad u'_n = \frac{A_n}{\rho_0 a} e^{i(\omega_n t + \pi/2)} \cos(k_n x),$$

where  $A_n$  is the amplitude,  $\omega_n = n\pi a/L$  is the natural frequency, and  $k_n = \omega_n/a$  is the wave number.

Stability of an individual mode is determined by the net energy addition to the mode. The condition for the transition to instability is defined by the balance between thermoacoustic energy

input and acoustic losses (due to boundary layer and sound radiation through open tube ends) per period of oscillation. The first quantity can be expressed in the following form (Culick 1976)

$$(3-5) \quad \Delta E_{added} = \frac{(\gamma - 1)S}{\mathcal{P}_o} \int_{-l_e}^{L+l_e} dx \int_0^T p' \dot{Q}' dt ,$$

where  $S$  is the cross section area of the tube;  $T$  is the cycle period; and  $\dot{Q}'$  is the unsteady component of the heat transfer rate.

The unsteady heat transfer rate in the system with a thin heater can be represented by a transfer function  $Tr$ , following Merk (1957):

$$(3-6) \quad \frac{\dot{Q}'(t)}{\dot{Q}_0} = Tr \frac{u'_-(t)}{u_0} \delta(x - l_g) ,$$

where  $u'_-$  is the velocity fluctuation in the upstream tube section just before the heater; subscript 0 stands for mean values; and  $\delta$  is the delta function.

Generally, the unsteady heat transfer rate can be dependent not only on velocity but also on pressure perturbation. However, in the systems with flows at low Mach numbers and convective heat transfer, Equation (3-6) is adequate for description of the unsteady heat transfer rate.

The transfer function is complex-valued. Its absolute value is usually between 0 and 1. The phase delay  $\varphi$ , imposed on the heat transfer due to thermal inertia of the heater-flow system, does not exceed a quarter of period of an acoustic oscillation. The transfer function appropriate for our analysis is extracted from the results of CFD modeling of a flow with an oscillating component around a cylinder (Kwon and Lee 1985). The absolute value and the phase shift of this function for the assumed temperature and the wire radius corresponding to the heater used in our system are given in Figure 3-2 versus reduced speed of the mean incident flow,  $u_0^* = u_0 / \sqrt{\omega\chi}$ ;  $\chi$  is the thermal diffusivity. Since the transfer function is dependent on frequency, the transfer functions have different values for different modes. The magnitude of this function is zero when the mean flow is zero. The phase shift favorable for thermoacoustic

conversion goes to zero at high values of the mean flow velocity. That means there should be an optimal point in the intermediate range of the flow velocity, where the power needed to excite a system is minimal. Further discussion of the transfer function will be given in Chapter 5, where more sophisticated and more accurate modeling is accomplished.

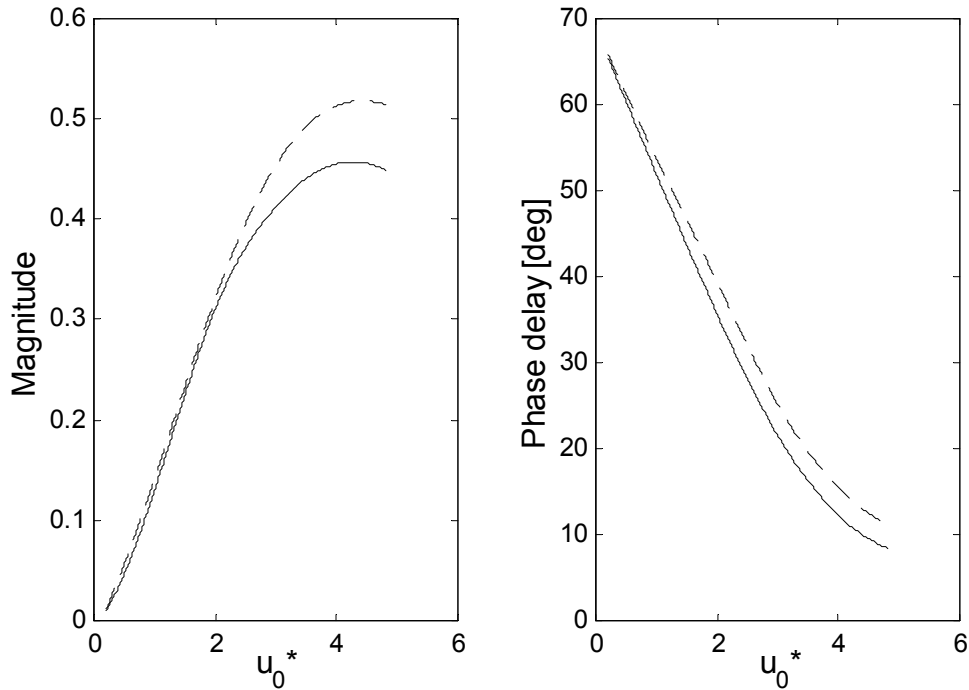


**Figure 3-2: Magnitude and phase delay of the transfer function. Solid line corresponds to the first mode; dashed line to the second mode.**

Substituting Equations (3-3), (3-4) and (3-6) into (3-5) and integrating over a chamber volume and a cycle period, we find that under the assumptions imposed the thermoacoustic energy added to the mode (index  $n$  is omitted) during one cycle of oscillation is

$$(3-7) \quad \Delta E_{added} = \frac{\gamma - 1}{2} \frac{\pi |Tr| PSA^2}{a^3 \rho_0 m \omega} \sin(\varphi) \sin(2kl_g),$$

where  $P$  is the power supplied to the heater; and  $m$  is the mass flow rate. Since the phase shift is less than  $90^\circ$ , a sign of the added energy is determined by the last multiplier in Equation (3-7), which in turn is dependent on the mode number and a heater location. From Equation (3-7), it

directly follows that the first mode can be excited only if the heater is in the upstream part of the tube and if  $0 < \varphi < \pi$ . The positions of the heater favorable for the second mode instability are the first and the third quarter of the tube, and so on for higher modes. This is in accordance with all previous studies (e.g., Rijke 1859, Raun et al. 1993) and the current experimental investigation.

Energy lost during one cycle of oscillation consists of components due to acoustic boundary layer presence inside the tube and sound radiation from open tube ends. They are calculated with standard approximate expressions (e.g., Howe 1998):

$$(3-8) \quad \Delta E_{bl} = \frac{\pi}{2\sqrt{2}} \frac{\Pi L A^2}{a^2 \rho_0 \sqrt{\omega}} \left( \sqrt{\nu} + (\gamma - 1) \sqrt{\chi} \right),$$

$$(3-9) \quad \Delta E_{sr} = \frac{1}{2} \frac{\omega S^2 A^2}{a^3 \rho_0},$$

where  $\Pi$  is the perimeter of a tube cross section, and  $\nu$  is the kinematic viscosity.

The critical value of the power, corresponding to the transition to instability when other system parameters are fixed, is found from the balance of thermoacoustic energy addition (3-7) and acoustic losses (3-8) and (3-9). This value is equal to

$$(3-10) \quad P_{cr} = \frac{m \left( \pi a \Pi L \sqrt{\omega} \left( \sqrt{\nu} + (\gamma - 1) \sqrt{\chi} \right) + \sqrt{2} \omega^2 S^2 \right)}{\sqrt{2} (\gamma - 1) \pi |Tr| S \sin(\varphi) \sin(2kl_g)}.$$

### 3.3 Results and discussion

Stability boundaries calculated using Equation (3-10) are presented in Figure 3-3 for three heater positions and for the first two modes that are unstable in our system. Note that under the assumption of a uniform temperature field, at heater locations 1/4 and 5/8 of the tube length, only one of these modes can be unstable. In the other case ( $x/L = 1/8$ ), both modes can potentially be

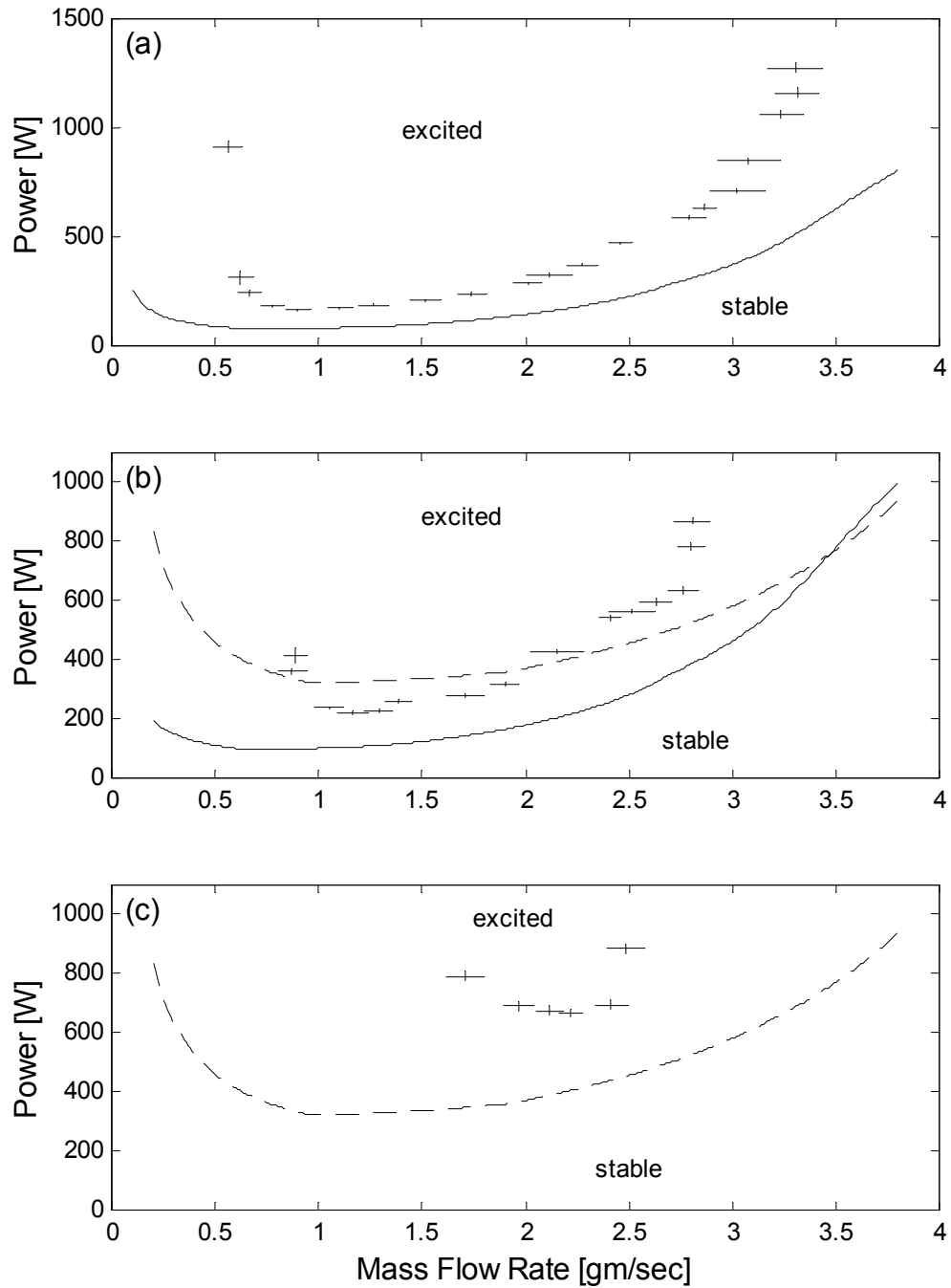


**Figure 3-3: Stability boundaries calculated by simplified modeling and compared with experimental data. Solid line corresponds to the first mode; dashed line to the second mode. Heater location: (a)  $x/L = 1/4$ ; (b)  $x/L = 1/8$ ; (c)  $x/L = 5/8$ .**



excited; however, the first mode is more prone to instability, consistent with experimental observations.

The general shape of the stability curves resembles a distorted parabola. It goes steeply upward at sufficiently low and high mass flow rates, and there is an optimal value of the flow rate when the power needed to excite the system is minimal. Since acoustic losses increase with a frequency, the stability boundary of the first mode is lower than that of the second mode, that is, less power is required to excite the instability. Also, the critical powers at heater location  $1/4$  of the tube length are lower than those at  $x/L = 1/8$ , because the last multiplier in denominator in Equation (3-10) is larger in the second than in the first case.

Concerning the accuracy in predicting the experimental data, one can see that the simplified modeling greatly underpredicts tests results. In the intermediate flow rate range, the error is about 100%. The calculated excited regime is much wider than that in reality, and the errors at high and low flow rates are significantly larger. We make comparison with experimental results corresponding to increasing power, since on the reversed path the system decays from excited states. Nonlinear phenomena, completely ignored in the simplified modeling, can affect the reverse transition.

Among the assumptions applied in computing the transition to instability (when flow fluctuations are really small) the only significant sources of errors must be due to the first two statements, (a) and (b) above, that ignore heat losses from the system. A non-uniform temperature profile causes the distortion of mode shapes that displaces the optimal point (from instability initiation point of view) for the heater location from its actual position. Therefore, assumption (a) should push the calculated stability boundary downward. Due to assumption (b) we ignored heat losses from the heater due to thermal radiation to environment and to heat conduction (through the insulation frame) to the tube walls. The consequence of this approximation is that a significant factor is not accounted for, namely, that a fraction of the power delivered to the gauze is not transmitted to the air flow. Hence, the stability curve computed by simplified formulation is again

displaced downward. Also, the frequencies of the modes must grow in the heated system followed by an increase in acoustic losses, an effect also ignored in the simplified modeling. The computed frequency values are 163 Hz and 326 Hz for the first and the second mode respectively. They are about 10 % lower than those observed during the tests.

Although the general behavior of the stability boundary is captured by simplified modeling, large quantitative errors are not acceptable for practical application of this theory. Since the most likely reason for discrepancies is the absence of heat transfer modeling, next chapter will be devoted to such an analysis. After determining the temperature field in the Rijke tube, we will attempt to apply a linear acoustic theory for a non-uniform medium to find the stability boundaries more accurately. That will be the subject of Chapter 5. Nonlinear phenomena, such as limit cycles and hysteresis at the stability boundaries observed during the tests, cannot be predicted by the linear simplified modeling. A nonlinear theory constructed on the basis of a linear model for a non-uniform medium will be developed in Chapter 6.

## Chapter 4

# Heat Transfer Analysis

### 4.1 Heat balance equations

Thermoacoustic instabilities in a Rijke tube are dependent on the properties of the eigen acoustic modes and on the processes of heat addition to an air flow. In previous investigations no significant attention has been paid to accurate estimation of the first factor, and no or very simplified heat transfer analyses are usually reported in the papers devoted to Rijke tubes. In the preceding chapter it was shown that the stability boundary cannot be predicted accurately when thermal modeling is ignored. Since the major objective of this work is to achieve accurate theoretical results, we have to carry out a detailed heat transfer analysis aimed at determining the temperature field and distribution of heat fluxes in the system. This information will be used later to study the stability of the system.

Although only longitudinal acoustic modes are of importance for the instability, the flow inside the Rijke tube in reality is three-dimensional; moreover, it can involve vortex shedding from obstacles, such as the insulation frame. The heat transfer process includes heat convection, heat

conduction, and thermal radiation. There are several distributed system components that exchange heat among themselves. In excited regimes of operation of the Rijke tube, the air flow is unsteady, and so also is the convective heat transfer, which plays an important role in these thermoacoustic instabilities.

The precise analysis of such a system would be based on direct numerical simulation of the flow, but due to the system complexity it is too expensive to be done accurately. Instead, our objective will be to construct an approximate quasi one-dimensional steady heat transfer model based on energy conservation equations and empirical correlations for heat transfer rates. This model will deliver the temperature field and the heat fluxes, averaged in time, which define mode shapes and mean heat addition to the air flow. Modification of heat transfer rates in excited regimes due to a significant oscillating component in the flow will be discussed in Chapter 6.

The structural model of the Rijke tube used for thermal analysis is given in Figure 4-1. It consists of an aluminum rectangular tube; a heating element in the form of a gauze; rods, through which electric power is delivered; an insulating gasket between the grid and walls of the tube; ambient air; and air flow through the tube (from left to right).

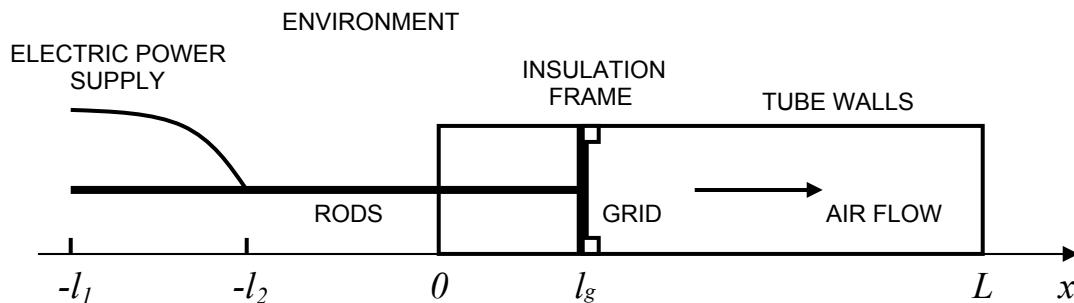


**Figure 4-1: Structural model of the Rijke tube for heat transfer analysis.**

The following types of heat transfer are taken into account:

(a) Forced convection between:

the grid and the air flow; the rod parts inside the tube and the air flow; and the tube walls and the air flow.

(b) Natural convection between:

the ambient air and the tube; the ambient air and the rod parts outside the tube; and the air flow and the rod parts inside the tube.

(c) Heat conduction:

in the horizontal direction inside the tube walls; between the grid and tube walls through insulation frame; and along the rods.

(d) Thermal radiation exchange:

outside the tube between the tube walls and environment; and inside the tube between the grid, the tube walls and environment.

Equations for the heat balance are formed for the grid and for the elements of the tube, rods and air inside the tube as functions of the horizontal coordinate. The symbol  $T$  in the following analysis designates the mean cross-section temperature for each structural element. Subscripts  $g$ ,  $a$ ,  $t$ ,  $r$ ,  $e$ , and  $c$  stand respectively for the grid, the air flow, the tube walls, the rods, environment, and the damping chamber. Superscripts  $(fcon)$ ,  $(ncon)$ ,  $(cond)$ , and  $(rad)$  designate forced convection, natural convection, heat conduction, and thermal radiation. Energy conservation for the grid states that the electric power released  $P_g$  leaves the grid as heat transferred to the air flow via convection; to the tube walls via heat conduction through the insulation gasket; to the rods via heat conduction; and to the tube walls and environment as thermal radiation

$$(4-1) \quad P_g = \dot{Q}_{ga}^{(fcon)} + \dot{Q}_{gt}^{(cond)} + \dot{Q}_{gr}^{(cond)} + \dot{Q}_g^{(rad)}.$$

The net flux of heat conduction through the element of the tube wall along the horizontal line is balanced by forced convection to the internal air flow, natural convection to the ambient air, a radiation component, and conduction from the grid. This balance is expressed as

$$(4-2) \quad \frac{\lambda_t S_t}{4D_t} \frac{d^2 T_t}{dx^2} = q_{ta}^{(fcon)} + q_{te}^{(ncon)} + q_t^{(rad)} - q_{gt}^{(cond)},$$

where  $\lambda_t$  is the tube material conductivity (for aluminum  $\lambda_t = 225 \frac{W}{mK}$ );  $S_t$  is the cross-section area of the tube walls;  $D_t$  is the side of the tube; and  $q$  is a heat flux. A similar equation applies to the rods except that additional power  $P_r$  is released in the rods due to electric current; radiation losses are ignored due to small rod sizes; and for the segments of the rods outside the tube a mixed convection occurs:

$$(4-3) \quad \frac{\lambda_r S_r}{\pi D_r} \frac{d^2 T_r}{dx^2} = q_{ra}^{(mix)} + q_{re}^{(ncon)} - P_r,$$

where  $\lambda_r$  is the rod conductivity (for copper  $\lambda_r = 400 \frac{W}{mK}$ ).

The net heat transported by convection of air flow inside the tube is balanced by forced convective exchange with rods, tube walls and a grid, which is considered to be very small in the horizontal direction:

$$(4-4) \quad m_a c_p \frac{dT_a}{dx} = 4D_t q_{ta}^{(fcon)} + \pi D_r q_{ra}^{(mix)} + \dot{Q}_{ga}^{(fcon)} \delta(x - l_g),$$

where  $m_a$  is the mass flow rate and  $c_p$  is the heat capacity (for air at  $T = 300K$  it is equal to  $1005 \frac{J}{kgK}$ ). All geometrical dimensions are given in Chapter 2-1, where the experimental setup is described. Since the temperature varies significantly in our system, local air properties are treated as functions of a local temperature.

We neglect natural convection between the air flow and the grid according to the criterion recommended by Mills (1992), since  $Gr / Re_{Dg}^2 \ll 1$  in our system, where  $Gr$  is the Grashof

number and  $Re$  is the Reynolds number. The Grashof number is defined as  $\frac{\Delta T g D_g^3}{T V^2}$ , where  $\Delta T$

is the temperature difference between the grid and the air flow,  $g$  is the gravitational acceleration; and  $Re = \frac{uD_g}{\nu}$ , where  $u$  is the local flow velocity.

Plots defining different convection regimes for fully developed internal flows in horizontal tubes are given by Metais and Eckert (1964); they show that the regimes of interest to our system are either forced or mixed (forced-natural) laminar convection. The air flow inside the tube before the grid is far from fully developed and the air flow near the tube walls behind the grid is disturbed by vortex shedding from the insulator frame; thus we assume that enhanced forced convective heat transfer dominates natural convection inside the tube. A Peclet number for the air flow inside the tube is much less than one, so that heat conduction in the air can be neglected in comparison with convective heat transfer.

The following boundary conditions are imposed. No heat transfer is assumed to occur at the ends of the tube

$$(4-5) \quad \left. \frac{dT_t}{dx} \right|_{x=0} = \left. \frac{dT_t}{dx} \right|_{x=L} = 0.$$

The same condition is valid for the left side of the rods; on the right side rod temperature is equal to the grid temperature

$$(4-6) \quad \left. \frac{dT_r}{dx} \right|_{x=l_1} = 0, \quad T_r|_{x=l_g} = T_g.$$

The temperatures of the environment  $T_e$  and air flow at the entrance  $T_a(0)$  are supposed to be known. They can be different since parts of the heated rods are located outside the tube entrance and the air sucked into the tube is heated up. The damping chamber walls are made from weakly conductive wood, and the temperature inside the damping chamber is taken equal to the temperature of an air flow at the tube exit.

Thus, the system of partial differential equations and appropriate boundary conditions are derived for heat transfer analysis in the system including all major structural components. To close the problem, we need expressions for the heat fluxes.

## 4.2 Correlations for heat transfer rates

In this section we list the empirical correlations for the heat transfer terms on the right-hand side of heat balance equations. The relation for power transferred from the heated grid to the air flow is reported by Torszynski and O'Hern (1995). Since the Reynolds number range studied coincides with ours, we use this result:

$$(4-7) \quad \dot{Q}_{ga}^{(fcon)} = \frac{T_g - T_a}{T_a} \frac{a^2}{\gamma - 1} \frac{(1 - k_1) S_g}{1.01} \frac{\mu}{D_g} \frac{\text{Re}_{Dg}^{0.5}}{\text{Pr}^{0.6}},$$

where  $a$  is the sound speed;  $S_g$  is the area covered by the gauze;  $\mu$  is the viscosity; Pr is the Prandtl number; Re is the Reynolds number based on the wire diameter  $D_g$ ; and  $k_1$  is the open area fraction. The averaged velocity of the incoming flow is used for the Reynolds number. Air properties in this equation are estimated for the temperature of air in the incoming flow  $T_a$ .

Conduction heat transfer from the grid to the tube walls is approximated by the formula for one-dimensional heat transfer, since the insulator size is small,

$$(4-8) \quad \dot{Q}_{gt}^{(cond)} = \lambda_m S_m \frac{T_g - T_t(l_g)}{H_m},$$

where  $S_m$  is the area of contact between the insulating frame and tube walls;  $H_m$  is the thickness

of the frame; and heat conduction coefficient for mecor is  $\lambda_m = 1.46 \frac{W}{mK}$ . The convective heat

transfer rate from the surface with area  $S'$  is often expressed through a Nusselt number, based on a characteristic size  $l$



$$(4-9) \quad \dot{Q} = Nu_1 \lambda_a S'(T' - T) / l,$$

where  $T'$  and  $T$  are the temperatures of the surface and ambient air.

To estimate the natural convection on the parts of the rods that are outside the tube, an expression for Nusselt number correlated by Churchill and Chu (1975) is used,

$$(4-10) \quad Nu_{Dr}^{(ncon)} = 0.36 + \frac{0.518(Gr_{Dr} Pr)^{1/4}}{[1 + (0.559 / Pr)^{9/16}]^{4/9}}.$$

Air properties in the expressions for Nusselt numbers are estimated at the film temperature, i.e., the average value of the surface and ambient temperatures. Convective heat transfer between the parts of the rods located inside the tube and the air flow is of mixed type. The Nusselt number  $Nu_{Dr}^{(ncon)}$  responsible for natural convection is found from Equation (4-10); the Nusselt number for forced convection for rods in parallel flow is given by Hatton et al. (1970)

$$(4-11) \quad Nu_{Dr}^{(fcon)} = (0.293 + 0.568 Re_{Dr}^{0.409}) \left( \frac{T_a + T_r}{2T_a} \right)^{0.154}.$$

Since both natural and forced convection is important for this heat transfer of mixed type, we make use of the recommendation by Churchill (1990) to determine the Nusselt number for mixed convection,

$$(4-12) \quad (Nu_{Dr}^{(mix)} - 0.3)^4 = (Nu_{Dr}^{(fcon)} - 0.3)^4 + (Nu_{Dr}^{(ncon)} - 0.3)^4$$

External natural convection from the Rijke tube itself can be described by the expression given by Lienhard (1973) for horizontal square cylinders:

$$(4-13) \quad Nu_{2Dt} = 0.48k_2 (Re_{2Dt} Pr)^{1/4},$$

where the coefficient  $k_2$  was equal to unity in the original expression. The tube in our system has attached metallic elements, such as fittings for thermocouples and supporting beams. Some additional heat loss takes place by heat conduction through these elements, followed by natural convection to the environment from them. The geometry of these elements does not allow us to

apply any correlation for enhanced heat transfer. We will find  $k_2$  by fitting calculated results to available experimental data for our system.

Heat exchange between air flow inside the tube and tube walls is quite complex. In the tube section before the grid, a simultaneously developing flow of low Reynolds numbers is present. Wibulswas (1966) tabulated the Nusselt number as a function of reduced coordinate  $x' = x / (D_t \text{Re}_{D_t} \text{Pr})$  along the tube for rectangular ducts with isothermal walls. In our system the tube is made from aluminum with high heat conduction coefficient, so that we can assume isothermal boundary conditions and apply Wibulswas's correlation given in Table 4-1.

$Nu$	3.75	4.39	4.88	5.27	5.63	5.95	6.57	7.1	7.61	8.06	8.50	8.91	9.30
$(x')^{-1}$	10	20	30	40	50	60	80	100	120	140	160	180	200

**Table 4-1: Dependence of Nusselt number on reduced distance for simultaneously developing flow. From Wibulswas (1966).**

In our Rijke tube the main heat source is the grid, which is attached to the insulating frame. The air flow is disturbed by the grid, and, what is more important, vortex shedding occurs from the step formed by the insulating frame, since the Reynolds number based on the step height is of order of several hundreds. Another confirmation of the presence of a disturbed layer along the tube walls after the heater is that laminar flow cannot produce such a sharp decrease in flow temperature as observed in our experiment (see Figure 4-3). There is no accurate correlation available in the literature for the convective heat transfer in such a flow, because of the system complexities, namely, a rectangular tube, three-dimensional frame, flow disturbed by the grid, presence of obstacles (thermocouples), and effects of natural convection on the flow just after the heater. We look for a correlation with the Nusselt number in the form commonly applied for turbulent flow, i.e., proportional to the Reynolds number in the power of 0.8,

$$(4-14) \quad Nu_{Dt} = k_3 Re_{Dt}^{0.8},$$

where the value of  $k_3$  is estimated for the best agreement between the calculated and experimental results. The procedure to determine coefficients  $k_2$  and  $k_3$  will be discussed in Section 4.5.

### 4.3 Thermal radiation model

The accurate analysis of thermal radiation in the Rijke tube is a very complex problem since it would involve radiation from the heater of a grid geometry. However, in the system treated here the temperatures are not so high to make thermal radiation a significant component of heat transfer, except for very high supplied power and very low flow rate. Therefore, we try to construct an approximate model accounting for thermal radiation. A closed rectangular chamber, such as shown in Figure 4-2, is considered for simulation of the tube section after the grid. The left side represents the hot surface of temperature  $T_g$ , the right side 2 is the surface at environment outside the tube with temperature  $T_e$ , and the longitudinal sides 3–5 are the tube

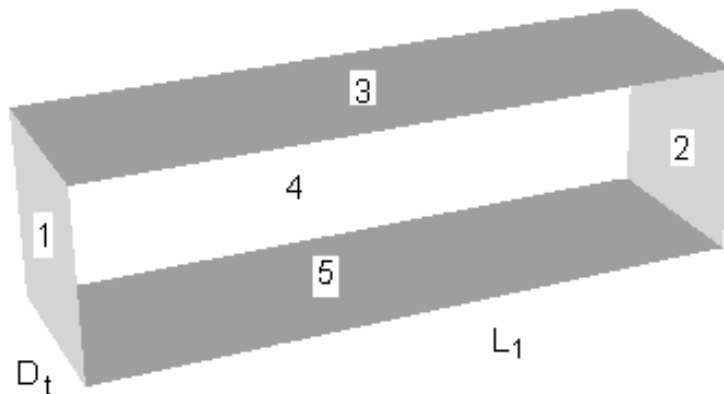


**Figure 4-2: Model of the downstream tube section for thermal radiation analysis.**

walls. Again, due to strong heat conduction in the tube walls, we assume for radiation analysis that the longitudinal surfaces have uniform temperature  $T_t$ .

Since a heating element does not cover entirely the tube cross section, a correction for heat fluxes is introduced to take into account the unblocked area. A similar configuration is considered for the tube section before the grid, but with opposite locations of the hot and cold ends.

For this simplified system a standard thermal analysis is applied following Mills (1992). Indices 1,2,3,4,5 designate respectively the hot surface, the cold surface, and three longitudinal surfaces. Equations for radiosities are

$$(4-15) \quad \begin{aligned} J_1 &= \varepsilon_1 E_{b1} + (1 - \varepsilon_1)(J_2 F_{12} + 4J_3 F_{13}), \\ J_2 &= E_{b2}, \\ J_3 &= \varepsilon_3 E_{b3} + (1 - \varepsilon_3)((J_1 + J_2)F_{31} + J_3(F_{35} + 2F_{34})). \end{aligned}$$

The view factors are calculated in the following way

$$(4-16) \quad \begin{aligned} F_{12} &= \frac{2}{\pi XY} \left\{ \ln \left[ \frac{(1 + X^2)(1 + Y^2)}{1 + X^2 + Y^2} \right]^{1/2} - X \tan^{-1} X - Y \tan^{-1} Y + \right. \\ &\quad \left. + X(1 + Y^2)^{1/2} \tan^{-1} \frac{X}{(1 + Y^2)^{1/2}} + Y(1 + X^2)^{1/2} \tan^{-1} \frac{Y}{(1 + X^2)^{1/2}} \right\}, \\ X &= Y = \frac{D_t}{L_1}; \end{aligned}$$

$$(4-17) \quad \begin{aligned} F_{13} &= \frac{1}{\pi X} \left\{ X \tan^{-1} \frac{1}{X} + Y \tan^{-1} \frac{1}{Y} - (X^2 + Y^2)^{1/2} \tan^{-1} (X^2 + Y^2)^{-1/2} + \right. \\ &\quad \left. + \frac{1}{4} \ln \left[ \left( \frac{(1 + X^2)(1 + Y^2)}{1 + X^2 + Y^2} \right) \left( \frac{X^2(1 + X^2 + Y^2)}{(1 + X^2)(X^2 + Y^2)} \right)^{X^2} \left( \frac{Y^2(1 + X^2 + Y^2)}{(1 + Y^2)(X^2 + Y^2)} \right)^{Y^2} \right] \right\}, \\ X &= 1, Y = \frac{L_1}{D_t}; \end{aligned}$$

$$(4-18) \quad F_{31} = F_{13} \frac{D_t}{L_1}.$$

View factor  $F_{35}$  is calculated by Equation (4-16), substituting  $X = L_1 / D_t$  and  $Y = 1$ ; and view factor  $F_{34}$  is found from Equation (4-17) at  $X = Y = D_t / L_1$ . Black body emissive powers are

$$(4-19) \quad E_{bi} = \sigma T_i^4.$$

Solving Equations (4-15), we find radiosities. Radiant heat fluxes are calculated by the expression

$$(4-20) \quad \dot{Q}_i^{(rad)} = \frac{\varepsilon_i S_i}{1 - \varepsilon_i} (E_{bi} - J_i).$$

In order to take into account the fact that the heater does not cover an entire cross section of the tube, the effective heat fluxes are estimated by multiplying the fluxes by the correction factor  $S'_1 / S_1$ , where  $S'_1$  is the area of the heater projection on the vertical plane. Another heat transfer rate from the outside surface of the tube walls to the environment due to thermal radiation is estimated by the expression

$$(4-21) \quad \dot{Q}_t^{(rad)} = \varepsilon_t \sigma S_t (T_t^4 - T_e^4).$$

#### 4.4 Computational procedure

Thus, the correlations for all heat transfer rates are now complete. Substituting them into Equations (4-1)-(4-4) and applying the boundary conditions (4-5)-(4-6), a closed system of equations is obtained for temperatures of the air flow, the tube walls and the rods as functions of horizontal coordinate  $x$ , plus an unknown value of the grid temperature. The system is solved numerically. Longitudinal structural elements are divided into a number of small intervals of length  $\Delta x$ . The spatial derivative for the fluid temperature is approximated by the upwind scheme

$$(4-22) \quad \frac{dT_a}{dx} \approx \frac{T_a^{(j)} - T_a^{(j-1)}}{\Delta x},$$

and the second-order difference scheme is used for the second spatial derivative for the temperature in solid structures

$$(4-23) \quad \frac{d^2 T_{t,r}}{dx^2} \approx \frac{T_{t,r}^{(j-1)} - 2T_{t,r}^{(j)} + T_{t,r}^{(j+1)}}{(\Delta x)^2}.$$

Upper indexes in the brackets relate to the numbers of the cross sections where the appropriate temperatures are estimated. The right-hand sides of Equations (4-1)-(4-4) are nonlinear due to radiation terms and dependence of heat transfer coefficients on air properties, which are the functions of temperature. To solve this system, an iterative procedure is applied. First, the temperature vector is composed

$$(4-23) \quad \underline{T} = \{T_a^{(1)}, \dots, T_a^{(N_a)}, T_t^{(1)}, \dots, T_t^{(N_t)}, T_r^{(1)}, \dots, T_r^{(N_r)}, T_g\},$$

where  $N_i$  is the total number of intervals in a corresponding system element. In our system  $N = 200$  is found to be sufficient to produce necessary accuracy.

Then, some temperature distribution  $\underline{T}_0$  is guessed for the structural components. It is used for calculation of the heat transfer coefficients and the thermal radiation terms, and a linear system is formed for the temperatures that enter Equations (4-1)-(4-4):

$$(4-24) \quad \underline{\underline{M}}(\underline{T}_0) \times \underline{T} = \underline{\underline{B}}_1 + \underline{\underline{B}}_2(\underline{T}_0).$$

This linear system is solved by standard methods. A new temperature field is applied for calculating nonlinear terms, and the linear system is solved again. This process is repeated until the temperature functions stop changing; in this way a converged solution is found. At each step, the local air properties are determined from a look-up table as functions of a local temperature.

Notice that there are limits on the applicability of this method. When the temperature of the grid becomes very high, which corresponds to extremely low flow rates or high supplied power, the iteration scheme does not produce a converged solution due to strong nonlinearity in the

radiation terms which are proportional to the fourth power of the temperature. Also, even if a converged solution is obtained in the regimes of high grid temperature, i.e., when radiative heat transfer becomes one of the dominant factors, the accuracy of such a solution deteriorates due to approximate modeling of thermal radiation.

#### **4.5 Tuning of heat transfer model**

In the model developed here, there are two unknown coefficients  $k_2$  and  $k_3$  that are supposed to be found through comparison with experimental data. To provide such data, a set of experimental runs was completed on the Rijke tube system in the characteristic range for the system variables. Data are recorded at three levels of power (near 144, 384, and 672 W), three mass flow rate regimes (near 0.6, 2.0, and 3.7 gm/sec), and one heater location (1/4 of the tube length). Given the complexity of these experiments only a few tests were carried out.

The temperature of the air flow at the tube exit and the temperature of tube walls in the hot portion of the pipe were averaged over the cross sections. Two examples of the experimental results as well as the calculated temperature profiles are shown in Figure 4-3. Fitting is accomplished for the wall temperature in the hot section and mean air flow temperature at the exit cross section. For illustrative purposes, the temperature of the air flow at the center line is shown. Note that the center line temperature can significantly deviate from the mean cross-section temperature at high mass flow rates. There is a hot core on the center line of the flow since the grid heats incident air more effectively at the center line than at the boundaries, and the heat exchange with tube walls affects mostly the air layers adjacent to the walls. Temperature uniformity over a cross section cannot be achieved due to the small residence time of air pockets in the tube at high flow rates.

The values  $k_2 = 0.4$  and  $k_3 = 1.7$  are found to produce satisfactory accordance between results of experiments and the model. The deviation between experimental measurements and theoretical calculations is presented in Table 4-1 for a set of system parameters (heater position is fixed at  $x/L = 1/4$ ). Discrepancies are expressed in percents with respect to the absolute temperature.

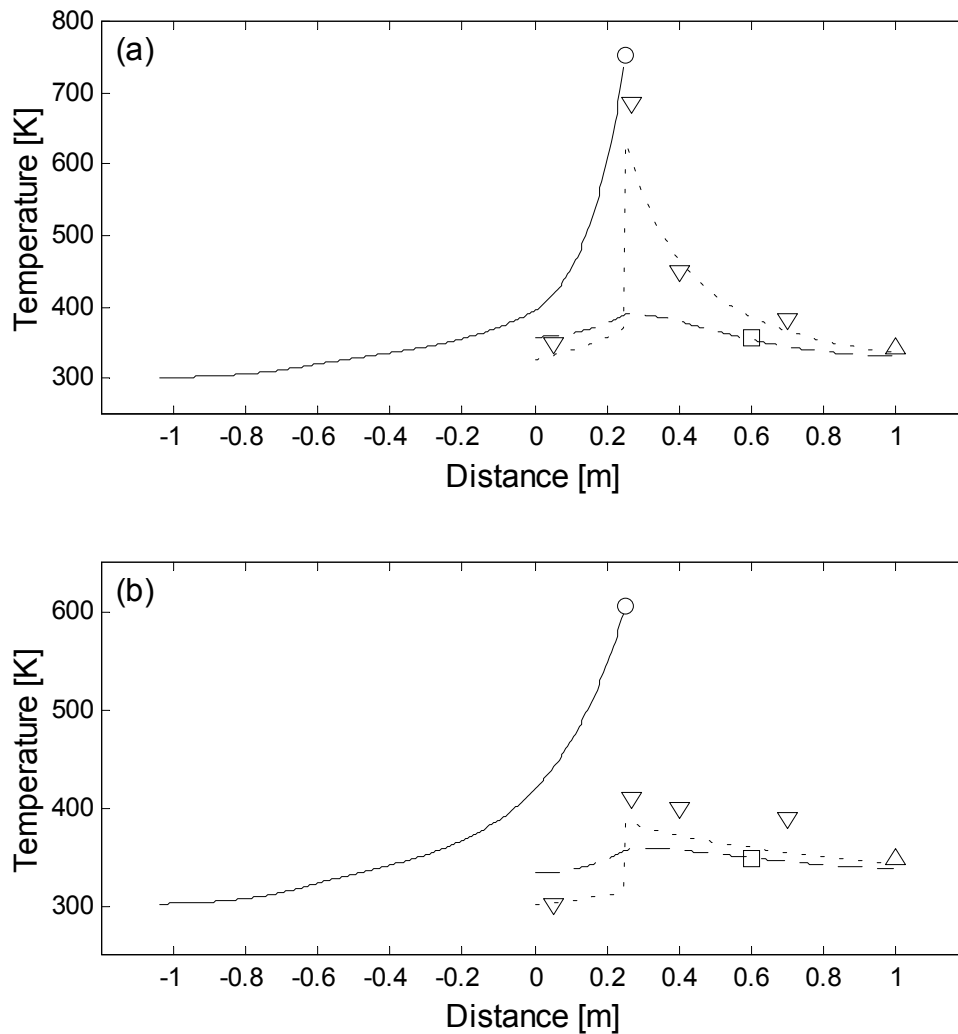


**Figure 4-3: Calculated temperatures in structural components: solid line, rods; dashed line, tube walls; dotted line, air flow; o, grid. Measured temperatures: □, tube walls; ∇, air flow (centerline); Δ, air flow (averaged over cross section). System parameters: (a) 385 W, 0.57 gm/sec; (b) 383 W, 3.76 gm/sec.**



During the test, characteristic temperatures are not strictly constants in time; they oscillate with amplitude about 1.5%. Most of the calculated results at low and moderate levels of power coincide with experimental findings within the error of measurement. At high power and low flow regimes, as well as in excited states, deviations slightly exceed experimental error. It appeared to be impossible to find a converged solution for the regime with the highest power and lowest mass flow rate. Given the complexity of the system and imposed approximations, the agreement between theoretical and test results is considered to be satisfactory.

Test number	1	2*	3	4*	5	6	7	8
Power, W	383	384	385	671	673	145	143	144
Flow rate, gm/sec	3.76	2.00	0.57	1.88	3.52	0.65	2.35	3.91
(A) error, %	1.4	3.0	1.5	1.6	4	2.3	1.6	1.4
(B) error, %	0.3	1.4	0.9	3.1	2.1	2.2	0.3	0.3

**Table 4-2: Discrepancy between measured and calculated temperatures. \* - tests 2 and 4 are carried in the excited regime. (A) air flow at the tube exit; (B) tube walls in the hot section.**

Thus, the mathematical model developed here is able to predict temperature profiles reliably for the system parameters in the ranges of the primary interest, and gives an approximate estimation for extreme regimes.

## Chapter 5

# Linear Theory

### 5.1 Wave equation

The purpose of this chapter is to develop a theory that will predict transition to thermoacoustic instability more accurately than can be done using the simplified modeling discussed in Chapter 3. To improve accuracy, we relax the first two assumptions given in Section 3.1, namely, the results of the heat transfer analysis (described in Chapter 4) will be used to determine the effective power released from a heater to an air flow, and a non-uniform temperature field along the tube will be taken into account in analyzing stability of acoustic modes. Since the goal here is to model transition to instability when all disturbances can be considered small, other assumptions of Section 3.1 remain valid. In this section a derivation of the wave equation in a non-uniform medium is given.

The starting point is the fluid mechanics conservation equations for mass, momentum and energy for an air considered as a perfect gas:

$$(5-1) \quad \frac{\partial \rho}{\partial t} + \nabla \cdot (\rho \underline{u}) = \rho \Omega,$$

$$(5-2) \quad \frac{\partial}{\partial t} (\rho \underline{u}) + \nabla \cdot (\rho \underline{u} \underline{u}) = -\nabla p + \rho \underline{B} + \nabla \cdot \tau,$$

$$(5-3) \quad \frac{\partial p}{\partial t} + \underline{u} \cdot \nabla p = -\gamma p \nabla \cdot \underline{u} + (\gamma - 1) \dot{Q} + \rho a^2 \Omega,$$

where  $B$  is the specific body force;  $\tau$  is the viscous stress tensor;  $\dot{Q}$  is the heat addition rate per unit of volume; and  $\Omega$  is the volumetric source intensity per unit of volume. The energy equation (5-3) is written in a convenient form with respect to pressure (Culick 1988); heat conduction is neglected.

The fluid is considered to be inside the tube beyond the outer edge of the boundary layers formed at the tube walls, so that viscous stress can be ignored. Boundary layer thickness is much smaller than the tube diameter. It is also assumed that body forces are negligible. Since only longitudinal acoustic modes are important in our system, we make the formulation one-dimensional with the x-axis parallel to the tube center line in the direction of a mean flow:

$$(5-4) \quad \frac{\partial \rho}{\partial t} + \frac{\partial}{\partial x} (\rho u) = \rho \Omega,$$

$$(5-5) \quad \frac{\partial}{\partial t} (\rho u) + \frac{\partial}{\partial x} (\rho u^2) = -\frac{\partial p}{\partial x},$$

$$(5-6) \quad \frac{\partial p}{\partial t} + u \frac{\partial p}{\partial x} + \gamma p \frac{\partial u}{\partial x} = (\gamma - 1) \dot{Q} + \rho a^2 \Omega.$$

Pressure, density and velocity in the air flow, as well as heat addition and volumetric source, are represented as sums of averaged and small-amplitude fluctuating parts

$$(5-7) \quad p(x, t) = p_0 + p'(x, t),$$

$$\rho(x, t) = \rho_0(x) + \rho'(x, t),$$

$$u(x, t) = u_0(x) + u'(x, t),$$

$$\dot{Q}(x,t) = \dot{Q}_0(x) + \dot{Q}'(x,t),$$

$$\Omega(x,t) = \Omega'(x,t),$$

where the time-averaged component of the volumetric source is zero.

The steady part of the pressure is assumed to be constant along the tube; losses in the mean flow due to friction at the tube walls are negligible. Acoustic perturbations in the Rijke tube occur in the presence of a mean flow; however, the Mach numbers of both mean and oscillating flows are very small in our system (less than  $10^{-3}$ ), so both  $u_0$  and  $u'$  are considered as small values. Entropy waves may become an important source of thermoacoustic instabilities (Culick 1988); however, at low Mach numbers and moderate temperature gradients characteristic for our system, the entropy waves can be excluded from consideration (Dowling 1995).

Substituting Equations (5-7) into (5-4)-(5-6) and simplifying them, a linear system is obtained for fluctuating components

$$(5-8) \quad \frac{\partial p'}{\partial t} + \rho_0 \frac{\partial u'}{\partial x} + u' \frac{\partial \rho_0}{\partial x} = \rho_0 \Omega',$$

$$(5-9) \quad \rho_0 \frac{\partial u'}{\partial t} + \frac{\partial p'}{\partial x} = 0,$$

$$(5-10) \quad \frac{\partial p'}{\partial t} + \gamma p_0 \frac{\partial u'}{\partial x} = (\gamma - 1) \dot{Q}' + \rho a^2 \Omega'.$$

Combining Equations (5-9) and (5-10), the wave equation for the pressure perturbation in the Rijke tube is obtained

$$(5-11) \quad \frac{\partial^2 p'}{\partial t^2} - a^2 \frac{\partial^2 p'}{\partial x^2} + \frac{a^2}{\rho_0} \frac{\partial \rho_0}{\partial x} \frac{\partial p'}{\partial x} = (\gamma - 1) \frac{\partial \dot{Q}'}{\partial t} + \rho_0 a^2 \frac{\partial \Omega'}{\partial t}.$$

This is a main equation for our analysis. Notice that speed of sound  $a$  and density  $\rho_0$ , as well as a density gradient, are functions of the horizontal coordinate directed along the tube.

The difference from a conventional wave equation in a uniform medium is the presence of the term responsible for spatial variation of density. Its value is determined from the steady heat

transfer analysis discussed in the previous chapter. The forcing term responsible for thermoacoustic instability is proportional to the time derivative of heat release. The damping term, due to heat conduction and viscosity in the acoustic boundary layer and sound radiation at the tube open ends, is represented by the term proportional to the time derivative of the distributed volumetric source.

To analyze the stability of solutions of Equation (5-11) that define the stability of the entire Rijke tube system, boundary conditions and models for the terms on the right-hand side need to be developed.

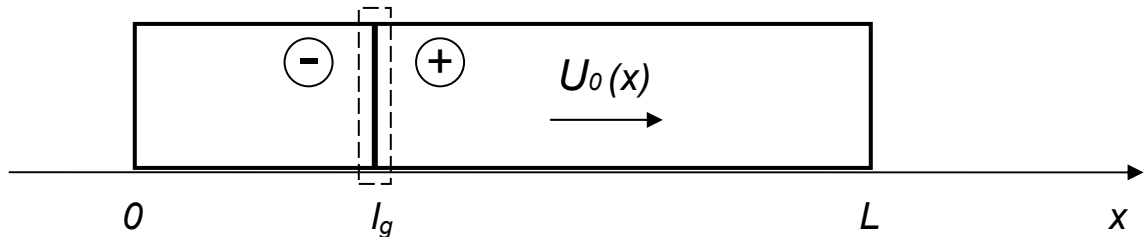


**Figure 5-1: Duct with one-dimensional flow and a plane heat source.**

## 5.2 Damping mechanisms

The geometry of the system is similar to that considered in Chapter 3 and is shown in Figure 5-1. The objective of this section is to come up with mathematical expressions for possible mechanisms of attenuation. There are three major linear damping sources in Rijke tubes. The first is due to acoustic boundary layers at the tube walls. It can be expressed through a volumetric source on the right-hand side of Equation (5-11). The second mechanism is sound radiation from the open upstream tube end and from the downstream end, which is connected to a damping chamber. Acoustic radiation losses are incorporated into the model via boundary conditions for

Equation (5-11) at the tube ends. The third factor is the convection of the sound from the tube by the mean flow.

The normal component of the acoustic particle velocity  $v_\delta$  at the outer edge of the boundary layer near the wall is defined to relate to pressure disturbance as follows

$$(5-12) \quad v_\delta = -Yp',$$

where acoustic admittance  $Y$ , which includes both thermal and shear stress admittances, can be expressed for a perfect gas (Howe 1998) by the formula

$$(5-13) \quad Y = e^{-i\frac{\pi}{4}} \frac{\sqrt{\omega}}{a^2 \rho} (\sqrt{\nu} + (\gamma - 1)\sqrt{\chi}),$$

where  $\nu$  is the kinematic viscosity,  $\chi = \lambda / c_p \rho$  is the thermal diffusivity ( $\lambda$  being the thermal conductivity). Therefore, the volumetric source (per unit of volume) responsible for acoustic boundary layer losses is

$$(5-14) \quad \Omega(x, t) = \frac{\Pi v_\delta(x, t)}{S} = -\frac{4Y(x)p'(x, t)}{D_t},$$

where  $\Pi$ ,  $S$  and  $D_t$  are the perimeter, area, and side of the tube square cross section.

Consider now the boundary conditions for Equation (5-11) at  $x = 0$  and  $x = L$ . At the tube ends, acoustic pressure and velocity fluctuation are related via the impedance  $Z$ :

$$(5-15) \quad p' = Zu'.$$

The upstream end ( $x = 0$ ) is an unflanged open tube end, and the corresponding impedance for the modes with wavelength much greater than the tube diameter is (Levine and Schwinger 1948)

$$(5-16) \quad Z_1 = -\frac{\rho\omega^2 R^2}{4a} - i\rho\omega l_{oe},$$

where the equivalent tube radius is related to the side of a square section as  $R = D_t / \sqrt{\pi}$ ; and the open end correction is  $l_{oe} \approx 0.61R$ . The downstream tube end ( $x = L$ ) is connected to the

damping chamber. The impedance at this end  $Z_2$  can be expressed through the impedance on the left end of the chamber  $Z_3$  and the end correction for such a junction (Gurbatov and Rudenko 1996):

$$(5-17) \quad Z_2 = \left( \frac{D_t}{D_c} \right)^2 Z_3 + i\rho\omega l_{tc},$$

where  $D_c$  is the size of the damping chamber cross section; and  $l_{tc}$  is the effective length of the junction, similar to the open end correction  $l_{oe}$ . Ingard (1953) has tabulated  $l_{tc}$ ; in our system this parameter is equal to  $0.71D_t$ . The chamber impedance is expressed in terms of the chamber attenuation and the load on its right side (Gurbatov and Rudenko, 1996)

$$(5-18) \quad Z_3 = a\rho \frac{\cosh(ikL_c)Z_4 + \sinh(ikL_c)a\rho}{\sinh(ikL_c)Z_4 + \cosh(ikL_c)a\rho},$$

where  $k$  is the complex-valued wave number;  $L_c$  is the chamber length; and  $Z_4$  is the impedance of the rear wall of the damping chamber. The wave number for sound propagation in pipes with dissipation can be expressed as follows (Gurbatov and Rudenko, 1996)

$$(5-19) \quad k \approx \frac{\omega}{a} - i \left( \frac{b\omega^2}{2a^3\rho} + \frac{1}{D_c} \sqrt{\frac{\pi\mu\omega}{2a^2\rho}} \right),$$

where  $b$  is the effective viscous coefficient:

$$(5-20) \quad b = \frac{4}{3}\mu + \xi + \frac{(\gamma-1)\lambda}{c_p},$$

where  $\mu$  is the dynamic shear viscosity;  $\xi$  is the bulk viscosity;  $\lambda$  is the thermal conductivity; and  $c_p$  is the specific heat capacity.

The impedance of the rear wall of the damping chamber  $Z_4$  can be expressed via the reflection coefficient  $R$

$$(5-21) \quad Z_4 = a\rho \frac{1+R}{1-R}.$$

The chamber rear wall is covered by a carpet, described in Section 2.1. The properties for such a material are given by Knudsen and Harris (1950). Data for the appropriate reflection coefficient as a function of frequency are presented in Table 5-1.

$f$ , Hz	128	256	512	1024
$R$	0.943	0.927	0.794	0.755

**Table 5-1: Reflection coefficient of the chamber rear wall as a function of frequency.**

In experimental series with the heater location  $x/L = 5/8$ , the rear wall of the chamber was made rigid to reduce acoustic losses. In that case, the reflection coefficient is  $R = 1$ , and the corresponding chamber impedance is  $Z_3 = a\rho \coth(ikL_c)$ .

Now let us estimate the remaining possible damping mechanism due to interaction between mean and oscillating flows in an open-ended tube. According to the study by Ingard and Singhal (1975), the acoustic power loss due to convection by the air current can be expressed as follows

$$(5-22) \quad W_c = \frac{5.33}{8} MSa\hat{u}^2 \rho,$$

where  $M$  is the Mach number; and  $\hat{u}$  is the amplitude of the acoustic velocity at the open end. Notice that this power loss is proportional to the Mach number, which is very small in our system (less than  $10^{-3}$ ). Indeed, it appears that the contribution by the mean flow to the total acoustic damping can be neglected in comparison with the first two mechanisms (which are of the same order of magnitude). Thus, all damping factors have been considered and relevant mathematical expressions have been derived.



### 5.3 Matching conditions at the heater

In this section, the matching conditions for the acoustic variables at the heater are considered. Since the dominant unsteady heat addition, leading to development of thermoacoustic instability, takes place at the heater, these conditions are of major importance for determining the system behavior. The thickness of a heated gauze in our system is very small in comparison with the other characteristic dimensions; hence the grid can be assumed to be infinitely thin, so that the jump conditions for acoustic variables at the heater can be applied (Figure 5-1).

Pressure perturbations just in front of and behind the gauze are related through its impedance

$Z_g$  :

$$(5-23) \quad p'_+ - p'_- = Z_g u'_p,$$

where  $u'_p$  is the area-averaged velocity through the gauze. Subscripts + and – stand for the upstream and downstream vicinity of the gauze. Using data given by Dickey et al. (2000), the grid impedance  $Z_g$ , estimated for the dimensions of the gauze employed in our system, appears to be so small that a jump in acoustic pressure across the heater is less than 0.1% with respect to the magnitude of the fluctuating component of pressure; and the effective length correction is about three orders of magnitude smaller than the tube end correction. The final results for the stability boundary are not very sensitive to such a small discontinuity in the acoustic pressure, and the effects due to uncertainties in the system parameters and errors in thermal modeling exceed those due to the pressure jump at the heater. Therefore, to exclude these insignificant factors, pressure perturbations are assumed to be equal at both sides of the heating element, i.e.,  $p'_- = p'_+$ .

Different from the pressure, the acoustic velocity fluctuations are not the same in the upstream and downstream vicinities of the heater because of the heat addition. Following Merk (1957), we will derive an equation for oscillating velocity at the thin heater. Apply the interface energy

balance in the heater vicinity (Figure 5-1), keeping only the essential contributions (heat conduction in the air is not important for a given system):

$$(5-24) \quad (c_p T u \rho)_+ - (c_p T u \rho)_- = \dot{Q} / S,$$

where  $\dot{Q}$  is the heat transfer rate from the heater to an air flow.

Representing the variables as sums of steady and small oscillating components (Equation 5-7), using the equation of state for a perfect gas  $p = RT\rho$ , and linearizing Equation (5-24), we obtain

$$(5-25) \quad c_{p+} p'_+ u_{0+} + c_{p+} p_{0+} u'_+ - c_{p-} p'_- u_{0-} - c_{p-} p_{0-} u'_- = (c_{p-} - c_{v-}) \dot{Q}' / S,$$

where subscript 0 stands for mean values. Taking into account the equality of pressure disturbances at both sides of the heater, the equation for velocity perturbation is derived

$$(5-26) \quad \frac{u'_-}{u_{0-}} + \left( \frac{c_{p+} T_+}{c_{p-} T_-} - 1 \right) \left( \frac{\dot{Q}'}{\dot{Q}_0} - \frac{p'_-}{p_0} \right) = \frac{c_{p+} T_+}{c_{p-} T_-} \frac{u'_+}{u_{0+}}.$$

To put the driving Equation (5-26) in general form, Merk (1957) introduced the complex-valued transfer functions, dependent on frequency, that define the response of a heat source to fluctuations in velocity and pressure immediately upstream of the source. It was shown also that at low Mach numbers the dependence of unsteady heat release on pressure perturbations can be neglected. Therefore, the transfer function pertinent to our study is defined as follows

$$(5-27) \quad \frac{\dot{Q}'}{\dot{Q}_0} = Tr \frac{u'_-}{u_{0-}}.$$

Substituting Equation (5-27) into (5-26) gives the matching conditions for velocity fluctuations at the heater:

$$(5-28) \quad u'_+ = \frac{c_{p-}}{c_{p+}} \left( 1 + \left( \frac{c_{p+} T_+}{c_{p-} T_-} - 1 \right) Tr \right) u'_-.$$

The next section is dedicated to selection of the transfer function  $Tr$  and discussion of its properties.

Besides heat addition to an air flow from a heater, there is also heat exchange between an air flow and tube walls that could possibly affect thermoacoustic characteristics of the Rijke tube due to the first term on the right-hand side of Equation (5-11). Because of the inertial properties of unsteady thermal boundary layers, the convective heat transfer rate between an air flow and tube walls must have a small time delay with respect to the instantaneous velocity at a given cross section of the tube. Since the heat transfer in the hot tube section significantly dominates over that in the cold section, we discuss only the section downstream from the heater.

By analogy with a cooling source positioned inside a Rijke tube, it follows (Equation 3-10) that such heat extraction from the air flow discourages the first mode instability development in the upstream half of the tube, and encourages in the downstream half, i.e., the influences from both tube portions are partly compensated when the heater is located in the first half of the tube. When a heater is positioned in the second half of the tube, and the second mode is responsible for instability, there are again the tube portions upstream from the heater where energy inputs to the acoustic mode have opposite signs. Noting also that convective heat transfer between an air flow and tube walls is minor in comparison with that between an air flow and a heater, and that no relevant models for our system geometry are available in the literature, we will ignore the influence of the convective heat transfer between an air flow and tube walls on the development of thermoacoustic instability.

## **5.4 Transfer function**

In this section, a transfer function between velocity fluctuations immediately upstream of the heater and unsteady heat release, defined by Equation (5-27), is discussed. This function is a very important characteristic in determining thermoacoustic instability appearance. Also, the largest uncertainties in the system are usually associated with the transfer function since it is dependent

on many factors, such as the heater geometry, fluid properties, flow regimes, and even history of the system. Analytical solutions in real systems are usually not possible for this function.

The heater in our system is a nichrome mesh composed of a set of wires. Its specifications are given in Chapter 2. Since a wire can be seen as a cylinder, and flows around isolated cylinders have been studied extensively, it is natural to prescribe a transfer function of a cylinder to the heater in our system with corrections due to some important effects, e.g., a partial blockage of the flow.

Different regimes of the flow around a cylinder with steady and oscillating components exist. When a characteristic size of the object is much less than an acoustic wavelength and the Mach number is small, the flow can be treated as incompressible (Stuart 1966). This approximation is valid in our system. In incompressible flows there are three main non-dimensional numbers that define the characteristics of the heat transfer function in the linear range, i.e., when the amplitude of oscillating velocity is much smaller than a mean flow velocity. These numbers are Reynolds number  $\frac{uD}{\nu}$ , Strouhal number  $\frac{\omega D}{u}$ , and the Prandtl number  $\frac{c_p \mu}{\lambda}$ ;  $D$  being a diameter and  $\omega$  being a frequency of oscillating flow. If temperature variations are not very large, which is typical for electric Rijke tubes, the Prandtl number can be considered constant.

Lighthill (1954) calculated the heat transfer function for a cylinder when Reynolds number is greater than 10 (i.e., boundary layer is present) and Strouhal number is less than 20. Bayly (1985) derived this function for the limit of low Peclet number (Oseen's regime), when the Reynolds number is much smaller than unity at Prandtl numbers of order of one. However, in our system the Reynolds number varies between 1 and 6, so that neither the Oseen approximation nor the boundary layer formulation is valid. In this intermediate regime, the analytical expression for the heat transfer function cannot be obtained, and results of numerical simulation of the flow with heat transfer must be used.

The most suitable for our system are the data obtained by Kwon and Lee (1985) for the heat transfer of a cylinder in superimposed oscillating and steady flows. Employing a finite-difference method, they calculated time-dependent heat transfer response of the cylinder to the velocity fluctuations by treating the flow as incompressible and two-dimensional. The reported results cover most of the range of the Reynolds number observed in our experiment. Prandtl number is constant and equal to 0.69.

It is shown by Kwon and Lee (1985) that thermoacoustic power generation is most effective when dimensionless mean flow velocity  $u_0^* = u_0 / \sqrt{\omega \kappa}$  and wire radius  $r^* = r \sqrt{\omega / \kappa}$  are around unity, meaning that at low and high mass flow rates it is more difficult to initiate instability than in some intermediate regime. The amplitude of dimensionless velocity fluctuation  $u' / \sqrt{\omega \chi}$  was always equal to unity. At low flow rates the assumption of small oscillating velocity with respect to the mean flow velocity is not strictly met; that can be a potential source of errors. Since no information is available in the literature for the transfer function in that range, we use the results reported, keeping in mind the possible inaccuracy in a low flow rate regime. The normalized unsteady heat release was described in the form of parametric plots for the absolute value and for the phase shift with respect to the velocity fluctuation. In our modeling, those functions are tabulated and transformed into the transfer function. For a particular system state, its value is found by interpolation. The magnitude and phase delay of the transfer function obtained in this way are shown in Figure 5-2 for the ranges of non-dimensional parameters characteristic for our system.

At low mean flow velocity the magnitude of the transfer function goes to zero, as does the phase delay at high flow rates. Thermoacoustic energy conversion is not effective at both limits, and there is some optimal value of the flow rate when this conversion is maximal. That means the stability curve should resemble a parabola, which is in accordance with data recorded in the tests.

The heating element in our system is a grid composed of cylinders. In order to apply the results obtained by Kwon and Lee (1985) for an isolated cylinder, the effective velocity of the incoming flow must be modified. First, due to finite dimensions of the insulating frame the flow velocity increases before encountering the heater. Second, the influence of neighboring cylinders on the heat transfer can be estimated with a help of the blockage factor  $\theta$  (Zukauskas 1987), which takes into account flow acceleration between cylinders. The effective velocity  $u_{ef}$ , substituted into heat transfer rate correlations, is related to velocity  $u$  in the incident flow as follows

$$(5-29) \quad u_{ef} = \frac{(1+\theta)S_1}{S} u,$$

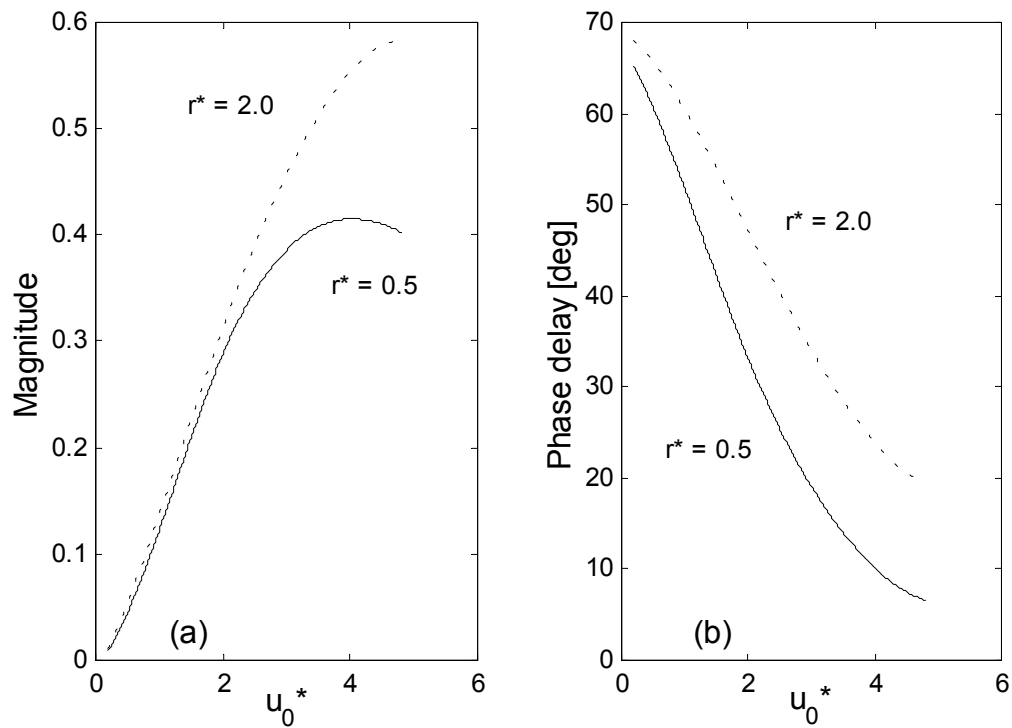


**Figure 5-2: Magnitude and phase delay of the transfer function  $Tr$ .**

where  $S$  is the tube cross-section area;  $S_l$  is the open area of the frame; and  $\theta$  is the closed fraction area of the gauze projection on the cross-section plane. Numerical values for these dimensions are given in Chapter 2, where the experimental system is described.

It appears that information available for the transfer function does not cover the entire region of system parameter variations. This function has to be extrapolated to the range of high mass flow rates. Thus, recalling also the possible errors due to nonlinearity at a low flow rate, we conclude that the transfer function is probably not accurate at both low and high mass flow rates.

## 5.5 Computational procedure

The system stability is defined by the stability of individual acoustic modes, which are solutions of wave equation (5-11). If all modes are stable, then the system is stable. If at least one mode is unstable, then the system is unstable. Although there is an infinite number of modes, only the lowest modes need to be checked for possible instability, because modal damping grows quickly with a frequency, as seen from Equations (5-13) and (5-16).

The mathematical formulation of the problem is closed now. To determine the system stability at a certain set of main system parameters, the first step is to calculate temperature field and the heat transfer rate at the heater to the air flow utilizing the heat transfer analysis developed in Chapter 4. Then, using the results of thermal modeling as parameters for the wave equation (5-11), the solutions (acoustic modes) can be found numerically applying a procedure similar to that described by Raun and Beckstead (1993).

The solution for the wave equation (5-11) is assumed to have form

$$(5-30) \quad p'(x, t) = e^{\sigma t} \psi(x),$$

where  $\sigma$  is a complex number; and  $\psi(x)$  is the complex-valued mode shape. Substitution of pressure perturbation (5-28) into wave equation (5-11) and appropriate boundary and matching

conditions (5-15), (5-23) and (5-28) produces an ordinary differential equation for the mode shape with unknown parameter  $\sigma$ . The value of  $\sigma$  is calculated iteratively by using Newton's method to match the impedances on the right side of the tube. Each nontrivial solution corresponds to a certain eigenvalue  $\sigma = \alpha + i\omega$ ; its real part  $\alpha$  is the growth rate and the imaginary part  $\omega$  is the frequency of the appropriate acoustical mode. If for a given set of system parameters, a growth rate of one of the modes is positive, then the system is unstable.

Let us now discuss the details of this numerical procedure. The algorithm of finding solutions of a wave equation in a stratified medium is standard (e.g., Kapur et al. 1972). Substituting Equation (5-30) into (5-11) and using the equation of state for a perfect gas  $p = RT\rho$  and the expression for volumetric source intensity (5-14), we get the equation for a mode shape

$$(5-31) \quad \sigma^2 \psi - a^2 \psi_{xx} - \frac{a^2}{T} T_x \psi_x = -\frac{4a^2 Y \rho}{D_t} \sigma \psi,$$

where  $Y$  is defined by Equation (5-13), and the zero index is omitted from coefficients of Equation (5-31).

The first term on the right-hand side of Equation (5-11) does not appear in (5-31), since the only significant unsteady heat release component that oscillates in phase with the pressure fluctuation is assumed to occur at the heater, entering the matching condition (5-26) only.

To apply boundary and matching conditions, the relation between acoustic velocity and pressure fluctuations is used

$$(5-32) \quad u' = ip'_x / \omega \rho_0.$$

Therefore, at the tube ends the following expression follows Equation (5-15)

$$(5-33) \quad \psi \Big|_{x=0,L} = \frac{iZ_{L,R} \psi_x}{\omega \rho} \Big|_{x=0,L}.$$

The matching conditions at the heater are obtained from Equations (5-23) and (5-28)

$$(5-34) \quad \psi(l_{g-}) = \psi(l_{g+}),$$



$$(5-35) \quad \psi_x(l_{g+}) = \frac{c_{p^-} T_-}{c_{p^+} T_+} \left( 1 + \left( \frac{c_{p^+} T_+}{c_{p^-} T_-} - 1 \right) Tr \right) \psi_x(l_{g-}).$$

Thus, the ordinary differential equation (5-31) for a mode shape is derived with boundary conditions (5-33)-(5-35); the unknown parameter  $\sigma$  is an eigenvalue in this problem. The system is solved numerically by discretizing the space similar to the method used in heat transfer modeling (Chapter 4). The tube length is divided into  $N$  intervals ( $N = 200$  in this study) with left side coordinates  $x_j$  and interval size  $\Delta x$ . Finite-difference schemes of the second order are applied to approximate the mode shape and its derivatives:

$$(5-36) \quad \begin{aligned} \psi(x_j) &= \psi_j, \\ \psi_x(x_j) &\approx \frac{\psi_{j+1} - \psi_{j-1}}{2\Delta x}, \\ \psi_{xx}(x_j) &\approx \frac{\psi_{j+1} - 2\psi_j + \psi_{j-1}}{\Delta x^2}. \end{aligned}$$

The same schemes are employed for temperature field discretization. Equations (5-36) can be applied only for internal points in the problem domain. One-sided schemes have to be used for the boundary conditions:

$$(5-37) \quad \begin{aligned} \psi(0) &= \psi_1, \\ \psi_x(0) &\approx \frac{-3\psi_1 + 4\psi_2 - \psi_3}{2\Delta x}, \\ \psi(L) &= \psi_{N+1}, \\ \psi_x(L) &\approx \frac{\psi_{N-1} - 4\psi_N + 3\psi_{N+1}}{2\Delta x}. \end{aligned}$$

In the case of the matching conditions, the situation is slightly different. The heater plane coincides with one of the points, say  $x_{n_g}$ . We choose the values of the discretized functions at

this point to correspond to the downstream side; hence the schemes for matching conditions, derived by using Newton's polynom (Kosarev 1995), are the following:

$$(5-38) \quad \begin{aligned} \psi(l_{g-}) &= \psi_{n_g-3} - 3\psi_{n_g-2} + 3\psi_{n_g-1}, \\ \psi_x(l_{g-}) &\approx \frac{3\psi_{n_g-3} - 8\psi_{n_g-2} + 5\psi_{n_g-1}}{2\Delta x}, \\ \psi(l_{g+}) &= \psi_{n_g}, \\ \psi_x(l_{g+}) &\approx \frac{-3\psi_{n_g} + 4\psi_{n_g+1} - \psi_{n_g+2}}{2\Delta x}. \end{aligned}$$

Thus, the system of  $N + 1$  equations is composed for  $N + 1$  variables  $\psi_i$  and the unknown  $\sigma$ . Since the system is uniform with respect to  $\psi_i$ , these variables can be multiplied by an arbitrary constant. Our problem is linear, so the absolute scale of the mode shape magnitude is not important. Of primary interest to us is the eigenvalue, whose real part determines the mode stability and its imaginary part is the mode frequency.

The method to solve the system is the following. Some value is prescribed for the mode shape function at the upstream boundary of the domain. Another value is guessed for the eigenvalue. It is convenient to select real part of the eigenvalues equal to zero and imaginary part corresponding to the expected mode frequency. Then the system (for mode shape variables  $\psi_i$ ) can be solved explicitly going from left to right in the numerical domain. When the right boundary is reached, the downstream boundary condition is checked. If it is not fulfilled with the prescribed accuracy, another eigenvalue is selected and the system is solved again. This procedure is repeated until the required accuracy at the downstream tube end is achieved. That occurs when a mode shape is converged to the solution of the wave equation (5-11), simultaneously fulfilling appropriate boundary and matching conditions. Thus, both mode shapes and an eigenvalue are found.

The example of the calculated two lowest mode shapes, corresponding to heater location  $x/L = 1/4$ , mass flow rate 2 gm/sec, and power supplied 300 W, is shown in Figure 5-3. The

first mode appears to be unstable for the given parameters; the growth rate is  $0.12 \text{ sec}^{-1}$ , and the frequency is 176.0 Hz. The second mode is stable with decay rate  $-19.0 \text{ sec}^{-1}$ , and frequency 350.8 Hz. A small break in the imaginary part of mode shapes, appearing due to the matching condition (5-25), can be noticed at the heater location.

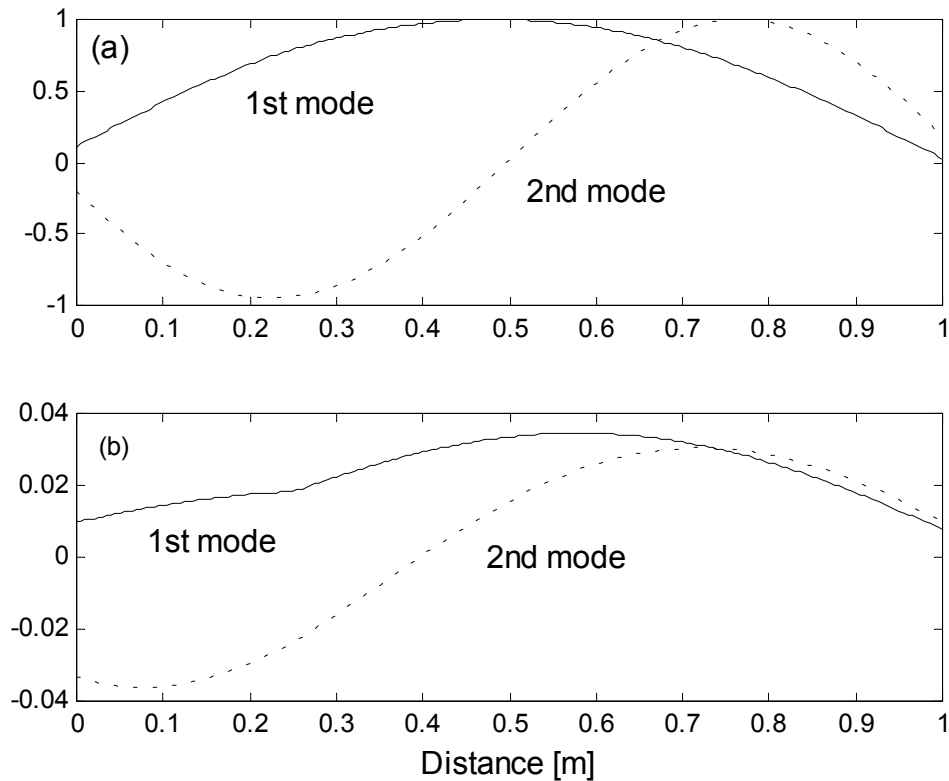


**Figure 5-3: Mode shapes of the first (solid line) and the second (dotted line) modes: (a) real component; (b) imaginary component.**

The outline of the algorithm for calculating a stability boundary is shown in Figure 5-4. First, a heater position of interest is chosen. Then a set of mass flow rates is selected, and the critical power values that define transition to instability are to be found for this set. Some value of the power supplied is chosen, and the heat transfer analysis developed in Chapter 4 is applied to determine both the temperature profile along the tube, and the mean power that is transmitted from the grid to the air flow by convective heat transfer. The temperature field is computed

iteratively. After this, the lowest modes are tested for stability. For each mode, an iterative procedure to determine a mode shape and an eigenvalue is applied. If at least one of the modes is unstable, then the system is unstable; otherwise, the system is stable at given the mass flow rate and the power supplied. Another power value is selected: a lower value, if the system was found to be unstable, and a higher value in the opposite case. The system stability is calculated at a new power value. In this manner, the critical power is determined at the boundary between stable and unstable states of the system. The same procedure is repeated for other mass flow rates and heater locations.

Notice that the algorithm contains six embedded cycles, and three of them are iterative. Although it looks quite complicated and time consuming, a set of computer programs written in the MATLAB environment allows us to calculate stability boundaries very effectively. The time spent for calculation is much less than that would be needed for completing a detailed CFD study of the system in consideration.

```

Heater Location {           % regular cycle
  Mass Flow Rate {         % regular cycle
    Power Supplied {       % iterative cycle
      Heat Transfer Analysis { % iterative cycle
        Acoustic Mode {   % regular cycle
          Stability         % iterative cycle
        }
      }
    }
  }
}

```

**Figure 5-4: Structure of numerical algorithm for determining stability boundary.**

## 5.6 Results and discussion

Stability boundaries computed by means of the method developed in this chapter for three heater locations are shown in Figures (5-5) to (5-7). Numerical results are compared with the experimentally determined transition to instability designated by crosses whose sizes correspond to experimental errors. The test results plotted are taken for the stability boundary obtained for the increase of power supplied. This way of power variation is associated with linear transition to instability similar to that found by the modeling. In the case of power decreasing, the system travels through the transition from an excited state, where both the temperature field, modified by the presence of an oscillating flow, and the various nonlinear effects can influence the stability boundary. Nonlinear phenomena are the subject of the next chapter.

Comparing Figures (5-5)–(5-7) and Figure 3-3, where numerical results obtained by simplified modeling are presented, we can notice a great improvement achieved in accuracy of theoretical results. In simplified modeling, the predicted stability curve corresponds to the power level no more than half as large as that recorded during the tests. When a sophisticated model is applied, the agreement is much better. In the intermediate flow rate regime and moderate power levels, numerical results coincide with experimental data within the uncertainties in system parameters. That means that the developed model can be applied for practical purposes of designing and analyzing real-world devices, where thermoacoustic instability can appear. In extreme ranges of system parameters, where assumptions for some parts of the modeling are violated, errors are larger, although the qualitative behavior is captured.

Let us now thoroughly compare experimental data and the results obtained by the theory developed in this chapter. At the heater location  $x/L = 1/4$  (Figure 5-5), the agreement is perfect for flow rates exceeding 1.7 gm/sec: the calculated stability curve crosses error bars of measured data. Critical powers in this range increase with a flow rate. At lower mean flow velocities, some discrepancy is observed. In the range 0.6–1.7 gm/sec, the computed stability

curve is higher than the measurements, and the minimal power value, at which instability can be appear, is over predicted. At even lower flow rates, the stability boundary starts to increase steeply, and experimental records demonstrate a higher rate of this increase than that corresponding to the modeling. The major factors that cause errors at a low mean flow velocity are threefold. First, data used for modeling the transfer function in this regime correspond to strongly nonlinear case, where the acoustic velocity exceeds that of the mean flow; hence, these data may be inappropriate for calculating the linear transition to instability. Second, at low flow rates and high power levels, the role of natural convection and thermal radiation are larger, leading to the errors noted in the heat transfer analysis (Chapter 4). The accompanying inaccuracy in the convective heat transfer rate and acoustic mode shapes can affect the computed stability curve. The third factor is the possible leakage in the damping chamber. At a low mean flow

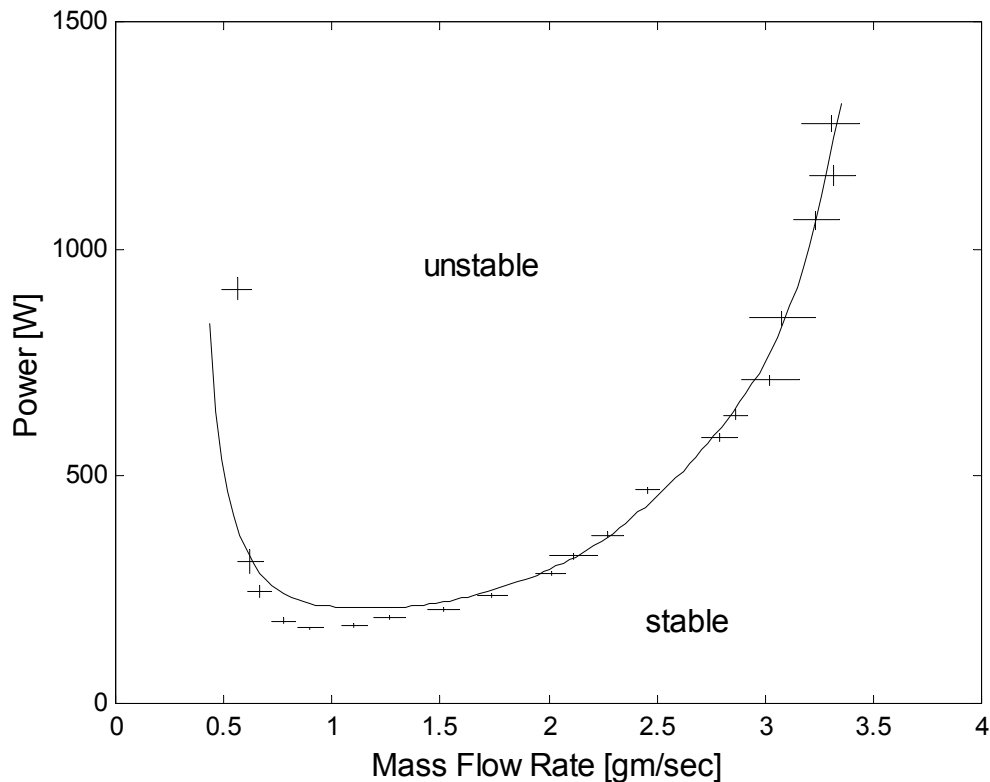


**Figure 5-5: Comparison of the experimental (crosses) and calculated (solid line) results for transition to instability. Heater location  $x/L = 1/4$ .**

velocity, its influence can grow so that the reported flow rates might be displaced from the actual ones. Despite these possible effects, the stability curve can be considered to be in good agreement with experimental data at heater location  $x/L = 1/4$ .

At another heater position  $x/L = 1/8$  (Figure 5-6), the behavior of the stability boundary is qualitatively similar to the preceding case, although the minimal value of the critical power corresponds to higher flow rate, and the whole curve is pushed upward. That is due to less favorable heater location in accordance with Equation 3-10. The agreement between calculated and measured results is satisfactory in the range of the mass flow rate between 1.0 and 2.8 gm/sec; the discrepancy only slightly exceeds error bars. Beyond this range, the experiments

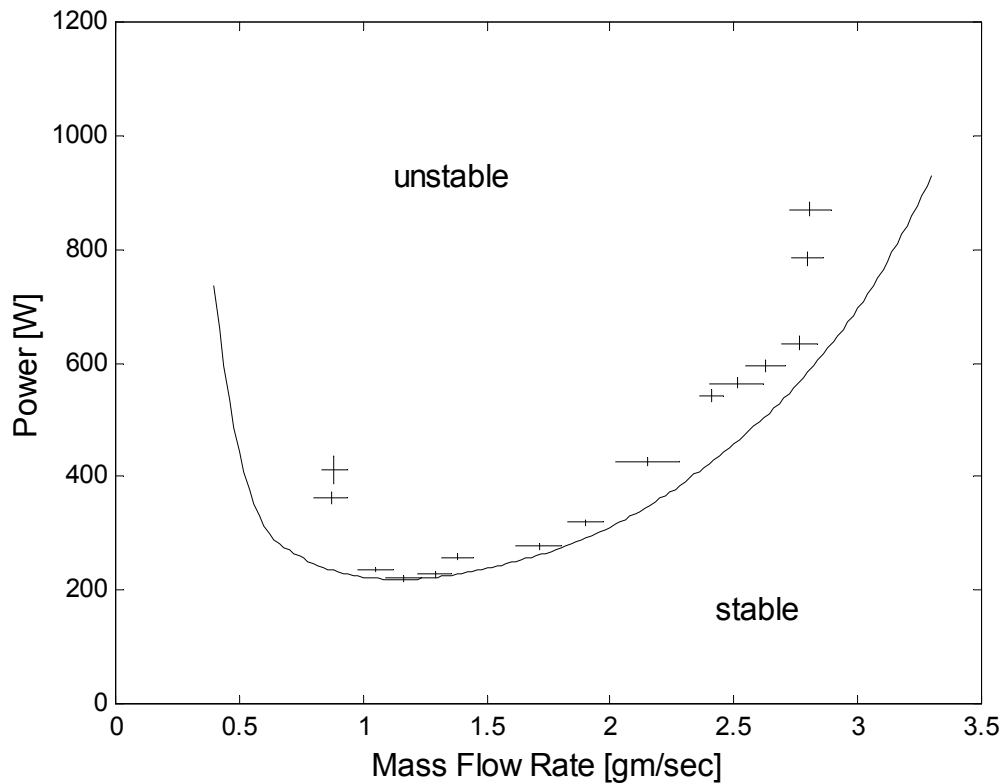


**Figure 5-6: Comparison of the experimental (crosses) and calculated (solid line) results for transition to instability. Heater location  $x/L = 1/8$ .**

demonstrate near-vertical behavior of the stability curve. The calculated boundary does not show this rate of increase, although the stability curve also goes steeply upward. The possible reason for higher errors is that the thermal modeling, which is a sub-model in the stability analysis, has been optimized for heater location  $x/L = 1/4$ , so heat transfer rates may be slightly different at other heater positions. The discrepancy in the stability boundary may be aggravated due to the fact that the first mode shape is steeper at point  $x/L = 1/8$ , hence, any inaccuracy in the mode shape would result in higher errors. Also, since the heater is located significantly closer to an open tube end, the one-dimensional assumption and edge effects can influence the results, compromising the accuracy in this case.

The stability boundary corresponding to the heater position  $5/8$  of the tube length is presented in Figure 5-7. Recall that only one direction of power variation (increase) has been used to determine transition to instability in this case, since the system appeared to be strongly history dependent. The stability boundary is again modeled well enough only in the intermediate range of flow rates, namely, 2.2–2.4 gm/sec. This range is much narrower than that in the previous cases. At lower mean flow velocity, the discrepancy is growing gradually. At higher flow rates, experimental boundary is nearly vertical, and the modeled curve is far from being so steep. For the considered heater location, the critical powers needed to trigger oscillations are significantly higher than those for heater locations in the upstream half of the tube. This power level provides higher characteristic temperatures in the system. Hence, the heat transfer analysis produces the results with significantly higher uncertainties, and can be used only for estimation purpose. Also, the mode that is responsible for instability at heater location  $x/L = 5/8$  is different from the previously considered cases. It is the second mode, and its frequency is roughly as twice as high as that of the first mode. For such a frequency, the assumption of slender Rijke tube, used in acoustic analysis, becomes strained; and the damping chamber narrowness is definitely not valid.



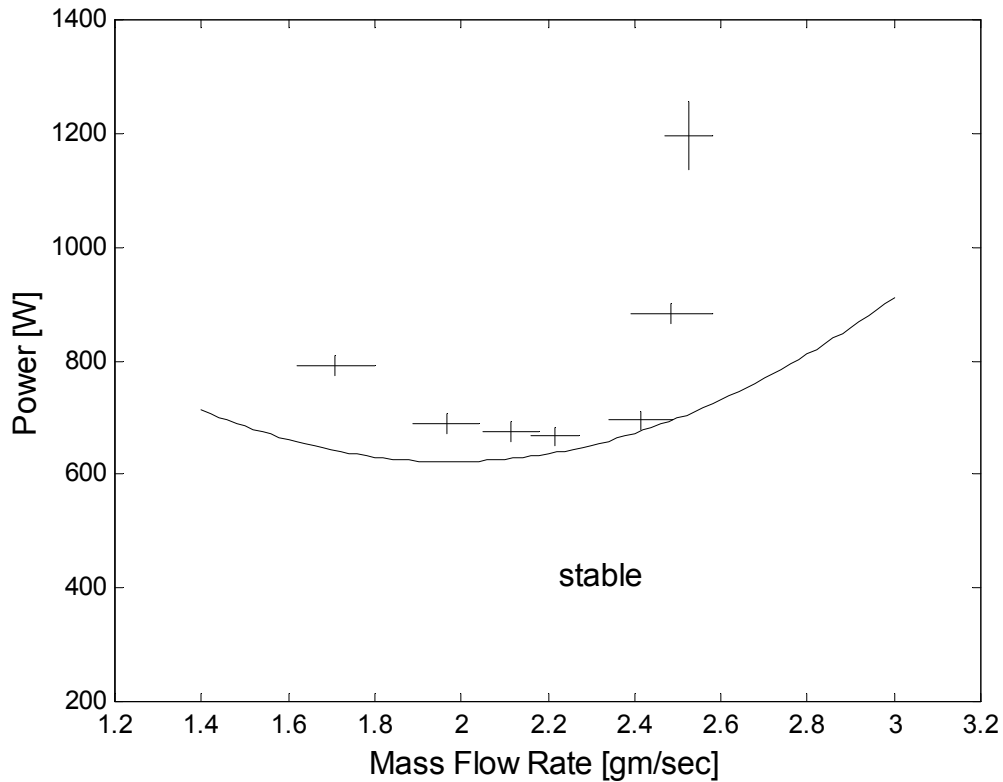


**Figure 5-7: Comparison of the experimental (crosses) and calculated (solid line) results for transition to instability. Heater location  $x/L = 5/8$ .**

As a consequence of all these factors, the discrepancy between the calculated and measured stability curve at the heater position  $x/L = 5/8$  is much more pronounced than those in the previous cases. However, the computed boundary can be used for approximate estimations of transition to instability, at least in the range of flow rates close to that where the minimal critical power is positioned.

The frequencies of the acoustic modes on the verge of instability are also of interest for model validation and practical purposes. The calculated values of these critical frequencies are shown in Figure 5-8 for three studied heater locations. Experimentally recorded dominant frequencies, given in the same figure, correspond to the excited states recorded after transition to instability. The test data scattering is due to unequal locations of these points from the stability boundary.

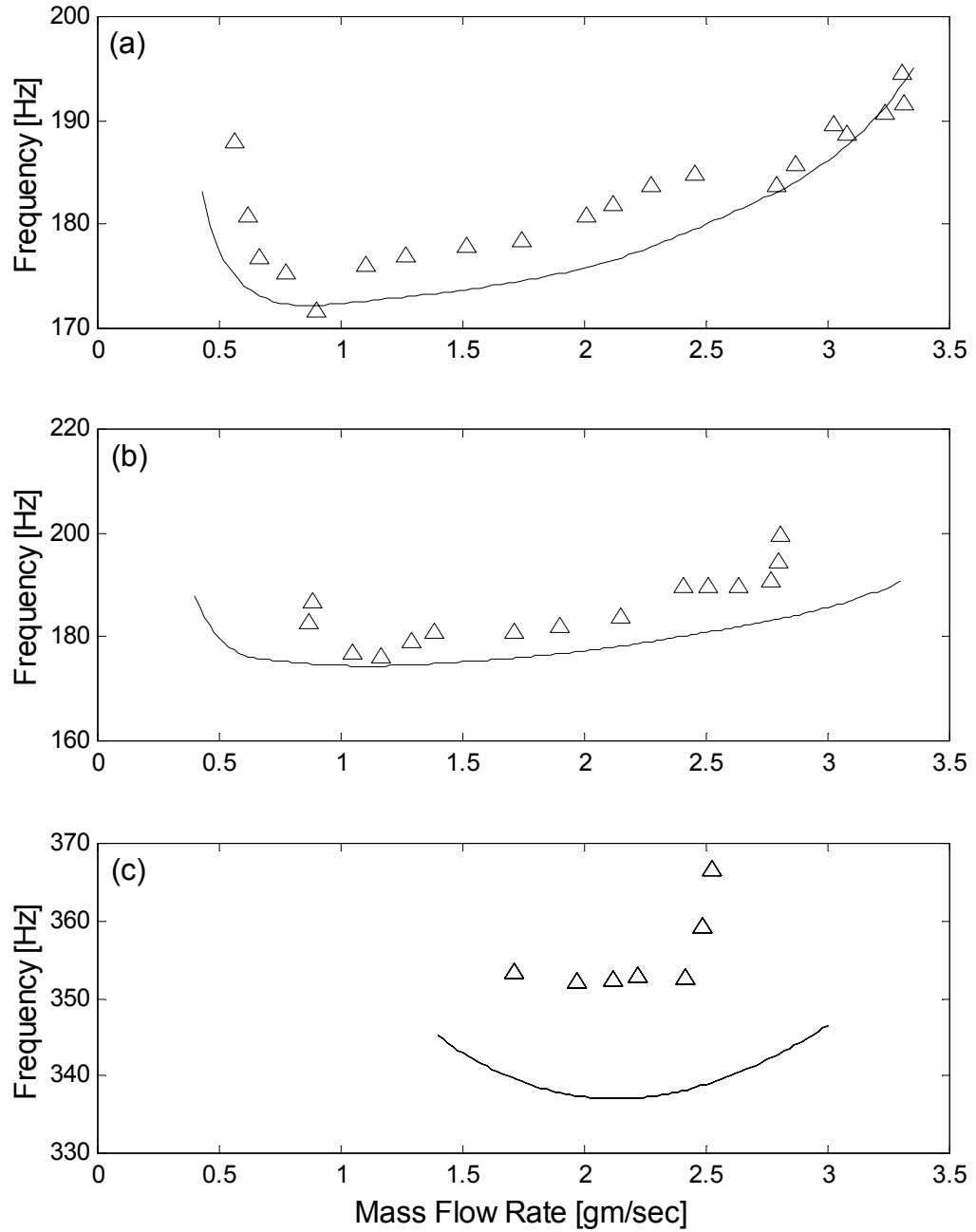


**Figure 5-8: Curves, calculated frequency of the unstable mode at the transition to instability;  $\Delta$ , measured dominant frequency in the signal after the transition to instability. Heater position: (a) 1/4; (b) 1/8; and (c) 5/8 of the tube length from the upstream end.**

Both experimental and theoretical values manifest the same tendency. Precise comparison of the measured frequencies and the frequencies calculated by the linear model is not appropriate and is not a purpose of this chapter, since the measured frequencies correspond to the excited steady states that are significantly affected by nonlinear effects and by the modified temperature field, when the acoustic velocity is comparable with the mean flow velocity.

Thus, in this chapter we have developed a linear theory capable of predicting transition to instability in the Rijke tube with axial temperature gradient for specified boundary conditions and the heat transfer function of the heater with negligible thickness. The results of the modeling demonstrate good agreement with experimental data for the ranges of system parameters where the model assumptions are fulfilled.

## Chapter 6

# Nonlinear Modeling

### 6.1 Nonlinear effects

The primary purpose of this chapter is to model the hysteresis effect and the limit-cycle properties of the Rijke tube and to compare results with experimental data reported in Chapter 2. Nonlinear mathematical modeling, developed here, is essentially an extension of the linear theory derived in Chapter 5.

Exact nonlinear modeling of the Rijke tube would require a prohibitively detailed CFD analysis due to the system complexity. Our goal is to stay within the approach of reduced-order modeling, retaining the factors of the most importance. The complex processes involved are approximated introducing reasonable assumptions and hypotheses, whose validity is subsequently judged by comparing results with experimental data. Modeling of limit cycles and hysteresis requires a nonlinear theory. Before constructing such a theory we estimate which nonlinear effects are of major importance.

During the experimental study we observed that after the transition to instability the amplitude of a dominant mode was quickly stabilized at a level comparable with the mean flow magnitude. Further increase of the supplied power led to gradual increase of the oscillation magnitude. Therefore, the Mach number of the oscillating flow component is of order of that of the mean flow, i.e., about  $10^{-3}$ . It is known that in open tubes, such as the case here, nonlinear effects in acoustic waves become effective only in the third-order theory, while the flow separation at the tube edges is a second-order effect, i.e., dominates over the nonlinearity of the gas dynamics inside the tube (Disselhorst and Van Wijngaarden 1980).

The ratio of the nonlinear to the linear component in sound radiation losses from the open tube end, estimated by Heckl (1990) using Chester's model (Chester 1981), is  $8a\bar{u}'/(D\omega)^2$ , where  $\bar{u}'$  is the averaged absolute value of the acoustic velocity at the tube end, and  $D$  is the tube diameter. This ratio is around one hundredth in the unstable regimes for the Rijke tube in consideration. Nonlinear sound radiation is too weak to limit the acoustic amplitudes of the excited modes at the levels recorded experimentally.

Thus, neither nonlinear gas dynamics nor nonlinear boundary conditions at the tube ends are of importance for determining the limit cycle properties. The fact that the magnitude of the oscillating velocity estimated in the vicinity of the heater tends to be stabilized near the mean flow velocity (slightly exceeding it) in the unstable regimes, and grows slowly with the increase of the supplied power, suggests that *flow reversal* at the heater location is critical for nonlinear modeling. When the flow is reversed, i.e., the total velocity is negative, application of Equation (5-27) may result in convective heat transfer directed from the cooler flow to the hotter grid, which is impossible. Therefore, Equation (5-27) is not valid for the nonlinear case, and must be modified. In this work we show that the proper adaptation of the linear transfer function to the nonlinear regime seems to explain all major nonlinear effects observed experimentally.

## 6.2 Heat transfer in pulsating flow

Let us first consider a simpler situation, namely, heat transfer from a heated isothermal object (a sphere or a cylinder in cross flow) to a flow having mean and acoustic components. When the characteristic size of the object is much less than an acoustic wavelength and the Mach number is small, the flow may be treated as incompressible (Stuart 1966). The commonly used form for the convective heat transfer rate in a steady flow, valid over a wide range of the Reynolds number, is

$$(6-1) \quad \dot{Q}_0 = k\sqrt{u_0} ,$$

where  $k$  is a coefficient proportional to the difference between the temperatures of the flow and the object. The heat transfer rate from the grid employed in the Rijke tube is based on the empirical correlation obtained by Torczynski and O'Hern (1995), obeying the law (6-1). Notice that the heat transfer rate does not depend on the direction of the velocity. If a quasi-steady approximation is invoked, implying that the momentary heat transfer rate is calculated assuming that the momentary flow velocity is constant in time, then the heat transfer rate can be found with the formula

$$(6-2) \quad \dot{Q}^{qs} = k\sqrt{|u|} ,$$

where  $\dot{Q}^{qs}(t) = \dot{Q}_0^{qs} + \dot{Q}'^{qs}(t)$  and  $u(t) = u_0 + u'(t)$ ; index  $qs$  stands for the quasi-steady assumption. The expression (6-2) can potentially produce large errors if the total velocity is so small that the square root law is not valid. If the velocity perturbation is small with respect to the mean flow velocity, then Equation (6-2) can be transformed into Equation (5-27), and the corresponding transfer function will be  $Tr_{lin}^{qs} = 1/2$ .

In the nonlinear problem, a sinusoidal variation of the flow velocity with frequency  $\omega$  inevitably produces a heat response with other frequency components. We define the nonlinear transfer function  $Tr$  in the following way

$$(6-3) \quad \left( \frac{\dot{Q}'}{\dot{Q}_0} \right)_{\omega} = Tr \frac{(u')_{\omega}}{u_0},$$

where  $(\ )_{\omega}$  designates a component of the function in brackets that oscillates with frequency  $\omega$ . The natural choice for the parameter measuring nonlinear behavior is the ratio of the oscillating velocity amplitude and the mean velocity  $\alpha = u_1' / u_0$ , estimated in the vicinity of the heater.

Now we propose the main *hypothesis* in our analysis: The frequency dependence of the nonlinear transfer function is assumed to be the same as for the linear transfer function; and the nonlinearity is taken into account by a coefficient  $G(\alpha)$ , which is a function of the parameter  $\alpha$ ,

$$(6-4) \quad Tr(\omega, \alpha) = G(\alpha) Tr_{lin}(\omega).$$

The hypothesis (6-4) is similar to the method of describing functions (DF) that is applied in the nonlinear control system theory (e.g., Eveleigh 1972). The DF method is commonly used to extend linear analysis to the nonlinear systems, retaining only one component of the output that has a fundamental frequency; and the nonlinear function relating input and output in a time domain is known. In this work, the motivation of implementing this approach is slightly different: the assumption of independence of the phase shift on the amplitude of oscillation is utilized with a purpose of approximately estimating the nonlinear unsteady heat transfer rate, which is not known in advance.

The mean heat transfer rate in the nonlinear case is assumed to be equal to the quasi-steady heat transfer rate averaged over a period of oscillation (the validity of this assumption will be discussed below)

$$(6-5) \quad \dot{Q}_0^{un}(\alpha) = \dot{Q}_0^{qs}(\alpha).$$

Symbol *un* is introduced to distinguish the heat transfer in the unsteady flow from the steady flow and the quasi-steady flow model. From Equation (6-4) we can immediately write

$$(6-6) \quad Tr^{qs}(\omega, \alpha) = G(\alpha) Tr_{lin}^{qs}(\omega).$$

We have already established that  $Tr_{lin}^{qs} = 1/2$ , hence the nonlinear component of the transfer function is expressed as follows

$$(6-7) \quad G(\alpha) = 2Tr^{qs}(\alpha).$$

Therefore, with the assumptions used here, a quasi-steady transfer function and a linear transfer function completely describe a nonlinear transfer function.

Let us calculate  $Tr^{qs}$  using Equation (6-2) and a sinusoidal function for the oscillating component in the total velocity  $u'(t) = u_0\alpha \sin(\omega t)$ . Applying Equation (6-2), we implicitly assume that the heat transferred to the flow is effectively diffused in the fluid so that the flow incident on a heated object always has the same temperature. Time variations of the velocity and the heat transfer in the quasi-steady model are shown in Figure 6-1 for different values of the nonlinear parameter.

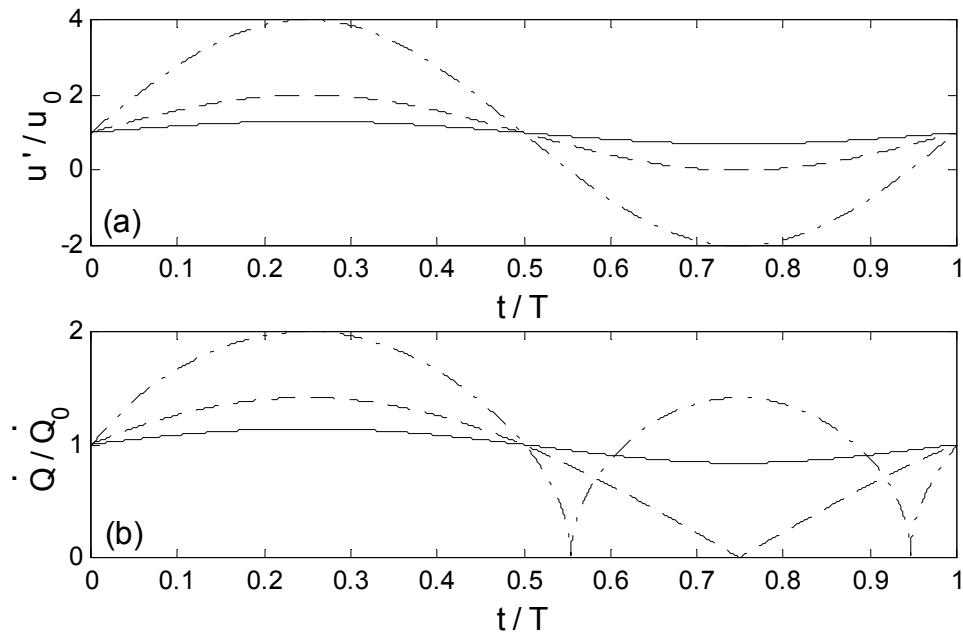


**Figure 6-1: Time variation of the reduced velocity in the incident flow (a) and the quasi-steady heat transfer rate (b):  $\alpha = 0.3$  (solid line);  $\alpha = 1$  (dashed line);  $\alpha = 3$  (dash-dotted line).**



From Equation (6-2) it follows that the mean quasi-steady heat transfer rate  $\dot{Q}_0^{qs}$  is

$$(6-8) \quad \dot{Q}_0^{qs} = \frac{\dot{Q}_0}{2\pi} \int_0^{2\pi} \sqrt{|1 + \alpha \sin \phi|} d\phi ,$$

where  $\dot{Q}_0$  is defined by expression (6-1). The unsteady component of the heat transfer rate is

$$(6-9) \quad \dot{Q}^{qs}(t) = \dot{Q}_0 \left( \sqrt{|1 + \alpha \sin \omega t|} - \frac{1}{2\pi} \int_0^{2\pi} \sqrt{|1 + \alpha \sin \phi|} d\phi \right) .$$

The quasi-steady nonlinear transfer function defined by Equation (6-3) can be computed from the following equation

$$(6-10) \quad \left( \frac{\dot{Q}'}{\dot{Q}_0} \right)_\omega^{qs}(t) = Tr^{qs} \alpha \sin(\omega t) .$$

Thus, substituting Equation (6-8) and (6-9) into expression (6-10) and taking a Fourier component corresponding to frequency  $\omega$ , we find the quasi-steady nonlinear transfer function:

$$(6-11) \quad Tr^{qs}(\alpha) = \frac{1}{\alpha} \frac{2}{T} \int_0^T \left( \frac{\dot{Q}'}{\dot{Q}_0} \right)_\omega^{qs}(\tau) \sin(\omega\tau) d\tau .$$

A velocity fluctuation having a finite amplitude inevitably produces higher harmonics in heat release due to the nonlinear form of the heat transfer rate. The amplitude of the  $n^{th}$  harmonic of the heat release can be estimated by the formula

$$(6-12) \quad \dot{Q}_n = \frac{2}{T} \left| \int_0^T \dot{Q}^{qs} \exp(in\omega\tau) d\tau \right| .$$

Nonlinear modifications for the mean heat transfer rate, the transfer function and the reduced amplitude of higher harmonics  $\dot{Q}_n / \dot{Q}_0^{un}$ , calculated from Equations (6-8), (6-11) and (6-12), are shown in Figure 6-2a and 6-3a. From Equation (6-11) it follows that  $Tr^{qs}(\alpha) \rightarrow 1/2$  when  $\alpha \rightarrow 0$ , i.e.,  $G(0) = 1$ . The nonlinear mean heat transfer rate decreases when the nonlinear

parameter increases from zero to one; this is caused by the square root law (Equation 6-2). After this point the heat exchange increases, since the heat transfer rate remains positive when the total velocity is negative. The behavior of the transfer function is opposite: it increases at the beginning, achieving maximum near unity of the nonlinear parameter, and then decreases, since at the limit of high oscillating velocity, or, equivalently, low mean flow velocity, the unsteady heat transfer does not possess a component with the frequency of flow oscillation. The second harmonic becomes dominant, as seen in Figures 6-1 and 6-3a. The amplitude of the second harmonic in heat release manifests a significantly pronounced local minimum when the nonlinear parameter  $\alpha$  is greater than one. The strong non-monotonic behavior is attributed to the specific law used for the heat transfer (Equation 6-2), which is not correct in time intervals when the total velocity is close to zero; in the real flow, this dependence should be smoother.

Now we examine the validity of the quasi-steady assumption for the time-averaged heat transfer. Such an assumption is widely used in practical applications involving convective heat

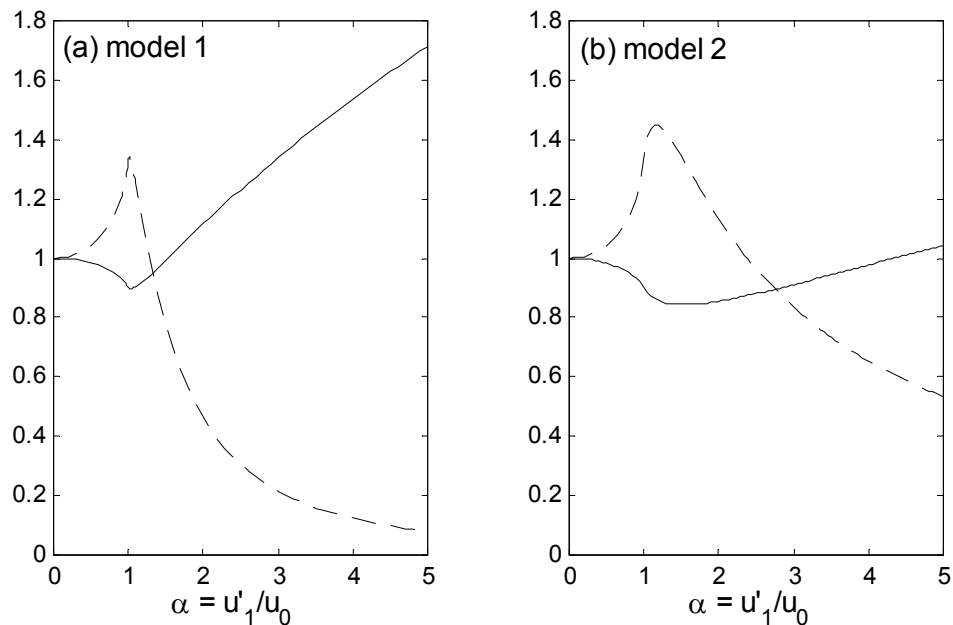


**Figure 6-2: Nonlinear corrections, calculated using model 1 (a) and model 2 (b): solid line, mean heat transfer rate  $\dot{Q}_0^{un} / \dot{Q}^{st}$ ; dashed line, transfer function  $Tr / Tr_{lin}$ .**

transfer from objects small compared to the acoustic wavelength, e.g., for granular drying processes in pulsating flows (Fraenkel et al. 1998). It is instructive to compare our model with a detailed CFD study accomplished for spherical particles in oscillating flows with a steady velocity component (Ha and Yavuzkurt 1993). The mean flow was too low for the boundary layer assumptions to be valid, similar to our Rijke tube experiment. The nonlinear parameter was varied from 0 to 5. A decrease of about 10% in the heat transfer rate was computed for  $\alpha = 1$ , and an increase of about 85% corresponded to  $\alpha = 5$ . The simple quasi-steady model, used in this work, produces a 10% decrease in the first case and 71% increase in the second. Thus, we conclude that the quasi-steady assumption for the mean heat transfer rate from the grid is justified for approximate reduced-order modeling, at least for moderate values of the nonlinear parameter.

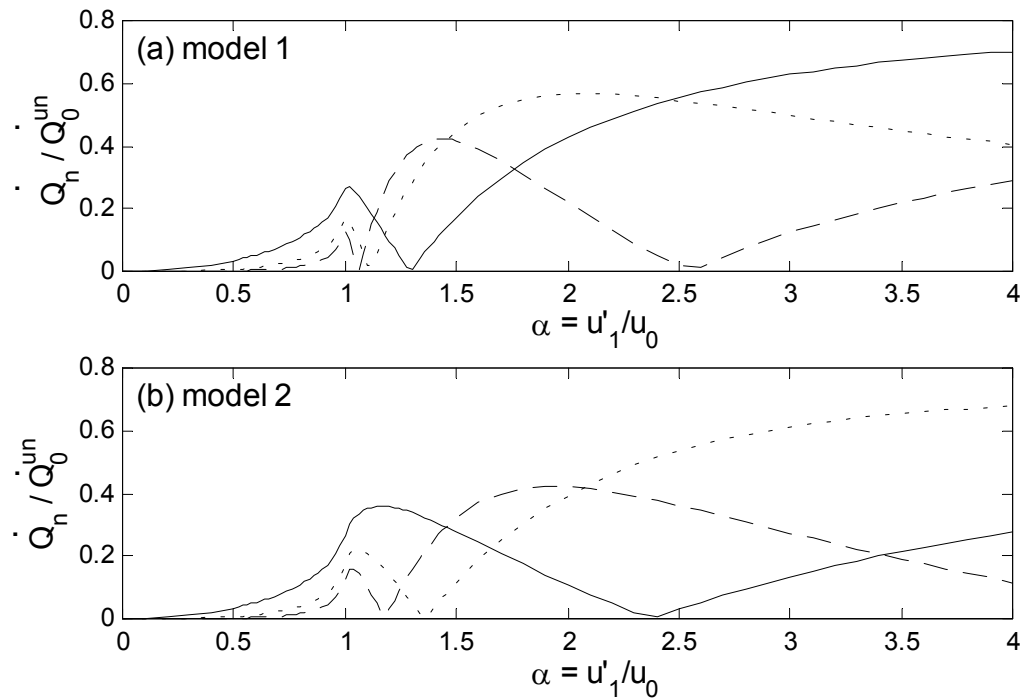


**Figure 6-3: Amplitudes of higher harmonics of heat transfer rate  $\dot{Q}_n / \dot{Q}_0^{un}$ : solid line, second harmonic; dotted line, third harmonic; dashed line, fourth harmonic.**

In the CFD study cited, no special attention was paid to quantification of the phase shift between the velocity and heat transfer fluctuations. However, variation of the phase shift with velocity amplitude, noticeable in the plots given by Ha and Yavuzkurt (1993) is definitely smaller than the typical phase delay of the transfer function (Figure 5-2). Therefore, the proposed hypothesis about weak dependence of the phase of the transfer function on the nonlinear parameter is consistent with the CFD study. Comparison of the nonlinear modeling results with experimental data and the ability to predict interesting nonlinear phenomena observed in the Rijke tube experiments will allow us to judge the validity of this hypothesis.

The situation with time-averaged heat exchange between the oscillating air flow and the tube walls is less clear. Most researchers apply quasi-steady models, which sometimes produce results perfectly matching experimental data (Hanby 1969). The complexity of the process does not allow us to obtain either theoretical solutions or widely applicable empirical correlations in this case. To achieve accurate results, the heat transfer between the pulsating air flow and the tube walls must be empirically adjusted to the experimental data as a function of both amplitude and frequency of the acoustic fluctuations (Perry and Culick 1974, Arpaci et al. 1993). Nevertheless, it is found that a quasi-steady model produces valid trends in heat transfer, so this assumption can be used for rough estimations. In the Rijke tube, the heat transfer between the grid and the air flow dominates over that between the tube walls and the air flow; hence, a quasi-steady model is sufficient for heat exchange between air and tube walls in our approximate analysis.

Before proceeding with modeling the nonlinear characteristics of a Rijke tube, we must address one more issue. The heating element in the Rijke tube is a grid, which can be viewed as a set of thin wires. The distance between the wires is small, and the boundary layer model is not valid, so that all regions between the wires of the grid are heated. Due to such heating, and small external heat losses immediately behind the grid, the temperature of the air incident on the grid becomes higher during some intervals of the cycle when the nonlinear parameter exceeds unity. This effect is caused by multiple crossing of the grid by some pockets in the flow. The coefficient  $k$  in

Equation (6-2) is no longer constant. To account for this effect, a simple modification of the dependence of the heat transfer rate on the total velocity is proposed

$$(6-13) \quad \begin{aligned} \dot{Q}^{qs} &= k\sqrt{|u|}, \quad \text{when } u > 0, \\ &= 0, \quad \text{when } u < 0. \end{aligned}$$

This model is similar to that discussed by Lehmann (1937). We should notice that it is not relevant to linear modeling of the transition to instability, when the magnitude of the acoustic velocity is always much smaller than the mean flow velocity. Equation (6-13) is applicable only to those heating elements where the effective heating of the air occurs on its pass through the heater, so that the temperature of the air becomes close to the heater temperature.

The correction described by Equation (6-13) significantly affects both the mean heat transfer rate and the transfer function in the nonlinear regimes. Although this rule is surely not very accurate, like Equation (6-2) it is simple and can be easily applied to various heaters. More accurate results can be obtained only by expensive CFD studies, which are usually valid only for particular configurations. The nonlinear modifications for the transfer function, the mean heat transfer rate and the amplitudes of higher harmonic of the heat release, calculated on the basis of Equation (6-13), are given in Figures 6-2b and 6-3b. We will refer to the model described by Equation (6-2) as the first; and the model incorporating Equation (6-13) as the second. The general trends are similar for both models. However, the maximum of the transfer function in the second model is greater and it decreases slower with the growth of the nonlinear parameter. A mean heat transfer in model 2 falls more steeply around  $\alpha = 1$ , and increases slower afterwards. The extreme points of these functions in model 2 are displaced to higher values of the nonlinear parameter.

Generally, the larger the absolute value of the transfer function, the more abrupt is development of the instability. The transfer function of the second model significantly exceeds that of the first model, so that the limit-cycle amplitudes predicted by the second model must be greater than

those for the first case. For high enough amplitudes of the oscillating component of the velocity, the transfer functions decrease in both cases, so further development of the instability is discouraged. This factor determines the amplitude of the limit cycles.

For oscillation amplitudes smaller than the mean flow velocity (compared at the heater location), the amplification increases with amplitude. That means that a steady-state limit cycle with finite amplitude may be possible when the system is linearly stable, so two different stable states can exist in the system for the same values of the parameters; the choice of a particular state is determined either by history or other factors, such as noise. A similar effect was derived by Bayly (1985) for a different system, namely, when the Peclet number based on the wire radius was much less than unity.

### 6.3 Stability boundaries

The transition to instability is modeled using the linear theory developed in Chapter 5. In the previous section we derived the transformation from the nonlinear transfer function  $Tr_{KL}$ , depicted in Figure 5-2, to the linear function  $Tr_{lin}$ ; the correction is given in Figure 6-2. Since  $Tr_{KL}$  was computed for constant amplitude of the oscillating velocity  $u'^* = 1$ , then from Equation (6-4) it follows that

$$(6-14) \quad Tr_{lin}(\omega) = \frac{Tr_{KL}(\omega, 1/u_0^*)}{G(1/u_0^*)}.$$

The inverse value of the reduced mean flow velocity plays the role of the nonlinear parameter, because the amplitude of the reduced oscillating velocity was equal to unity.

The calculated stability boundaries are shown in Figure 6-4. The computational procedure is identical to that employed in Chapter 5. Since in the modeling we assume the absence of finite-amplitude disturbances, theoretical results are to be compared with experimental data

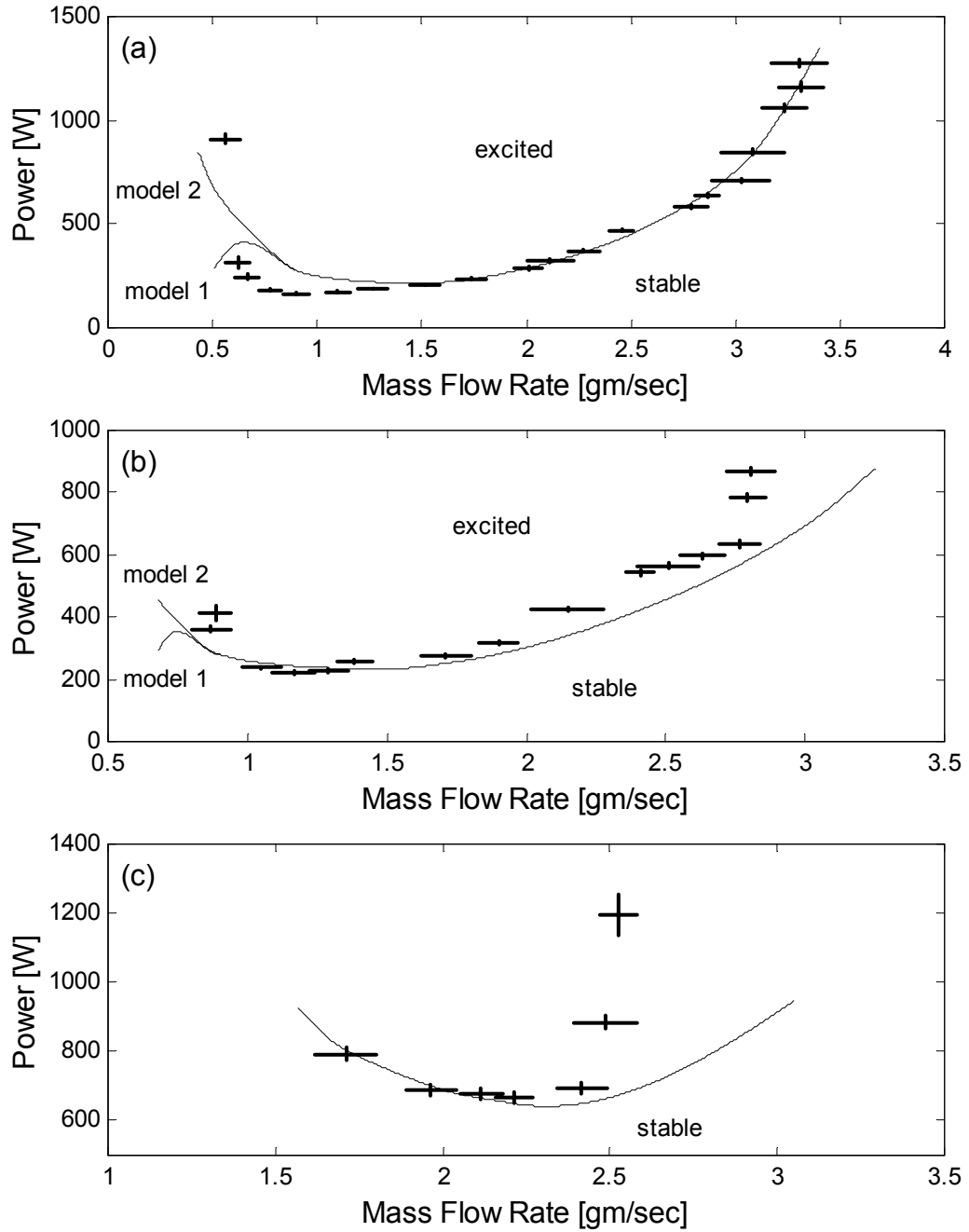


**Figure 6-4: Stability boundary for heater positions: (a)  $x/L = 1/4$ ; (b)  $x/L = 1/8$ ; (c)  $x/L = 5/8$ . Crosses, experimental data; curves, model results.**

corresponding to increasing power variation. For the heater locations  $x/L = 1/4$  and  $x/L = 1/8$ , it appears that at mass flow rates exceeding 0.85 gm/sec the nonlinear parameter in the original transfer function  $Tr_{KL}$  was less than unity in the vicinity of the stability boundary. In this case the nonlinear corrections for both models are identical, and they produce the same stability boundary, which agrees well with the experiment, except for high flow rates for the heater location  $x/L = 1/8$ . At low flow rates, the nonlinear parameter exceeds unity, and the difference between the two nonlinear models appears. The second model (Equation 6-13) qualitatively agrees with the observed behavior of the Rijke tube; deviations may be due to increased roles of natural convection and possible air leakage in the system. The stability curve of the first model (Equation 6-2) changes a direction at some point, contrary to the experiments. Such a discrepancy can be explained by the fact that at very low mean flow velocity, even if the oscillating component is high, the heat received by the flow from a cylinder is not convected away effectively, so in the reverse motion the temperature of the air is certainly higher than that in the incoming flow far enough from the cylinder; hence the assumption that  $k$  is constant in Equation (6-2) is not valid. Nevertheless, at sufficiently high enough mass flow rates this deficiency of model 1 is not exhibited, so it does not prevent us from using it to model the excited states in this range of flow rates.

For the heater location  $x/L = 5/8$ , the nonlinear parameter in the original transfer function  $Tr_{KL}$  was always less than one, so both models produce the same result. Accuracy is compromised at high mass flow rates. Since the second mode is responsible for instability, the characteristic frequency is about two times higher than that for the upstream heater location; and the assumption in the acoustic model that the tube is narrow may be marginal due to the high frequency of the sound waves in this case.



## 6.4 Hysteresis effect

The computational procedure for determining nonlinear behavior is similar to the calculations of linear stability, except in two respects. First, the time-averaged heat transfer is modified as shown by Equation (6-8) for model 1, and by the appropriate equation for model 2. Second, the transfer function is dependent on the nonlinear parameter  $\alpha$  (Equation 6-4); this factor is dominant in finding the limit-cycle amplitude. The equilibrium limit cycle corresponds to the case when the growth rate of the mode excited is equal to zero. Determining the limit-cycle properties is similar to the harmonic balance principle of the nonlinear control theory (Eveleigh 1972).

The results obtained are presented for a pressure amplitude at a location 15% of the tube length from the upstream end of the tube, the location of one of the pressure transducers during the tests. Since this location was always positioned upstream of the heater, the temperature variation at this point was relatively small for different operating conditions. This location is not far from the tube edge, so the results may be affected by the nonlinear tube end effects not accounted for here.

For investigating hysteresis, we consider the heater location  $x/L = 1/4$ , where records are available for both directions of power variation, and hysteresis is significantly pronounced. We define the critical power as the power value at which the jump occurs from one state (stable or excited) to the other. At high mass flow rates, a large gap appears between the critical powers, corresponding to the opposite directions of power variation (Figure 6-5a). Thus, two states can be observed for the same set of system parameters: one state is associated with a limit cycle having a finite amplitude; in the other state the amplitude is zero. This effect is identified as hysteresis at the stability boundary. The choice of a certain state is determined by the direction of the power variation. The results obtained by modeling show a similar pattern (Figure 6-5b), although the size of the power gap predicted by the model is notably higher than that measured.

The reason for the appearance of hysteresis is the non-monotonic behavior of the transfer function with respect to the amplitude of the acoustic velocity fluctuation (Figure 6-2). The

magnitude of the transfer function affects the effectiveness of the thermal-to-acoustic energy conversion (Equations 6-1 and 1-1): the larger the transfer function, the more significant is the unsteady component of the heat transfer rate. Due to the non-monotonic shape of the transfer function, more than one value of the amplitude of acoustic oscillation can exist at which the same amount of the energy input into the acoustic mode is provided; this energy addition compensates acoustic losses, and hence leads to the existence of the limit cycle. The transfer function grows initially with the increasing amplitude of the acoustic velocity fluctuation; therefore, the system that is linearly stable may also have two excited equilibrium states: one corresponds to the inclining part of the transfer function curve ( $0 < \alpha < 1$ ), the other to the declining portion ( $\alpha > 1$ ). The equilibrium limit cycle at the increasing branch of  $Tr$  is unstable, because at a small deviation from this point the increment of the thermoacoustic energy conversion has a sign opposite to that needed to return the system into the equilibrium state. The equilibrium limit cycle

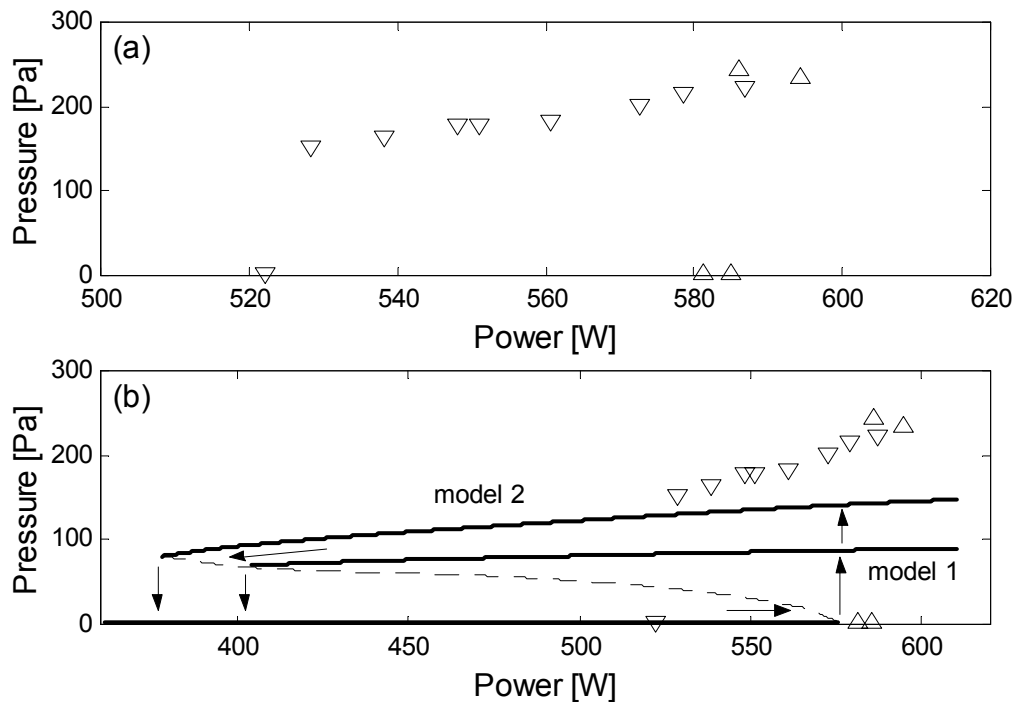


**Figure 6-5: Transition between stable and excited states: (a) test data ( $\Delta$ , power increase;  $\nabla$ , power decrease); (b) model results (bold line, stable limit cycle; dashed line, unstable) and test data. Mass flow rate 2.75 gm/sec. Heater location  $x/L = 1/4$ .**

at the declining  $Tr$  is stable, since now the input to the acoustic mode energy (from the heat released) varies in the way to prevent a deviation from the equilibrium point. These three equilibrium limit cycles are manifested in Figure 6-5b in the power range from 400 to 570 W: one stable state has a zero pressure fluctuation magnitude; the second equilibrium is unstable and depicted by a dashed line; and the third equilibrium limit cycle is stable with a finite amplitude in the vicinity of 100 Pa. Notice that the third (stable) equilibrium limit cycle is different for two considered models, and the first two equilibrium states are the same for both models.

At low mass flow rates, the experiment does not exhibit significant hysteresis. In fact, there is a narrow range of power between stable and unstable regimes where a steady state is not well defined. A tone can appear and disappear, and beating in the sound was sometimes observed. Pressure magnitudes in the range of the power 165–170 W (Figure 6-6a) correspond to some arbitrary recorded states. When the power exceeds 170 W, the sound amplitude is more or less

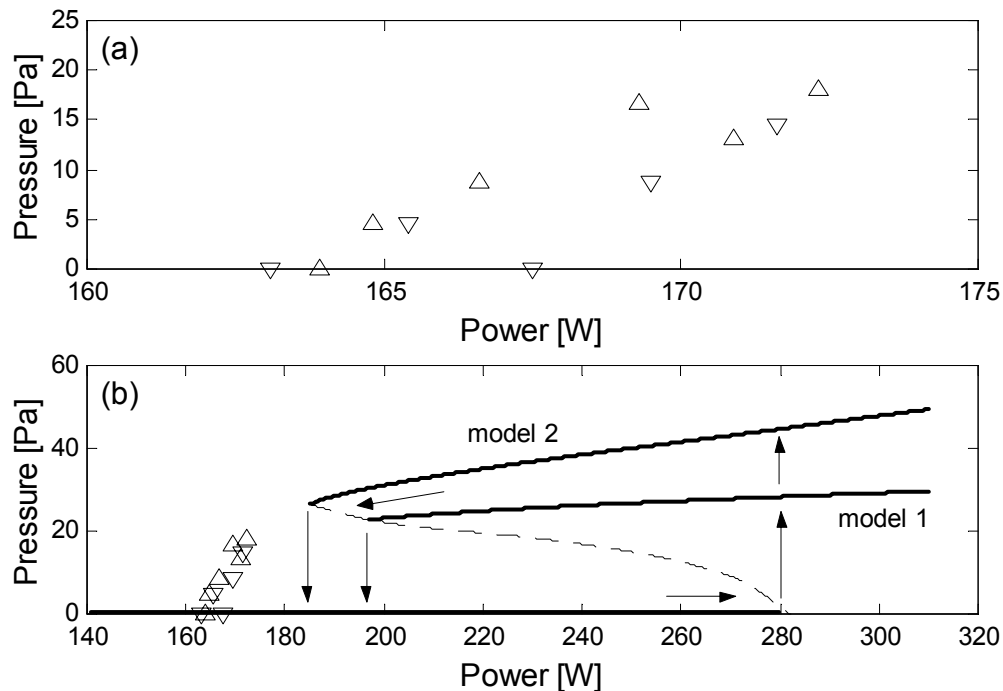


**Figure 6-6: Transition between stable and excited states: (a) test data ( $\Delta$ , power increase;  $\nabla$ , power decrease); (b) model results (bold line, stable limit cycle; dashed line, unstable) and test data. Mass flow rate 0.89 gm/sec. Heater location  $x/L = 1/4$ .**

stable. The model still produces hysteresis, although with a smaller gap between the critical powers (Figure 6-6b) than that for high flow rates. The computed and measured transitions to instability at flow rate 0.89 gm/sec are shifted quite far from each other. This is due to the discrepancy between test data and the results produced by both linear and nonlinear models for the stability boundary at low flow rates (Figures 5-5 and 6-4).

Thus, the models developed here help explain the mystery of hysteresis, although they overpredict the effect. The most likely reason for this discrepancy is a noisy environment in the vicinity of the heater inside the tube. Variations of the flow rate even in stable regimes are around 10%, corresponding to the size of the error bars shown in Figure 6-4. Those oscillations may be caused by the geometry of the system, e.g., the heated grid is fixed on a frame so as to avoid thermal and electric contact with the tube wall. Vortices can shed from this frame and disturb the flow. Such perturbations may initiate early transitions between stable and excited states, effectively reducing the hysteresis loop. This mechanism would explain the overprediction of the gap between critical powers, corresponding to the opposite directions of power variation, at high mass flow rates. At the lower flow rates, two additional factors cause the hysteresis gap to contract even more: first, the relative error in mass flow rate increases when the mean velocities are lower (Figure 6-4); and second, the predicted gap is smaller. That can lead to total disappearance of hysteresis, similar to the experimental observations (Figure 6-6a).

## **6.5 Limit-cycle properties of a self-excited mode**

Let us now consider the limit-cycle properties deep inside the excited regimes for two characteristic heater positions  $x/L = 1/4$  and  $x/L = 1/8$ . The calculated and experimental results for the amplitude and frequency of the self-excited (first) acoustic mode in the unstable

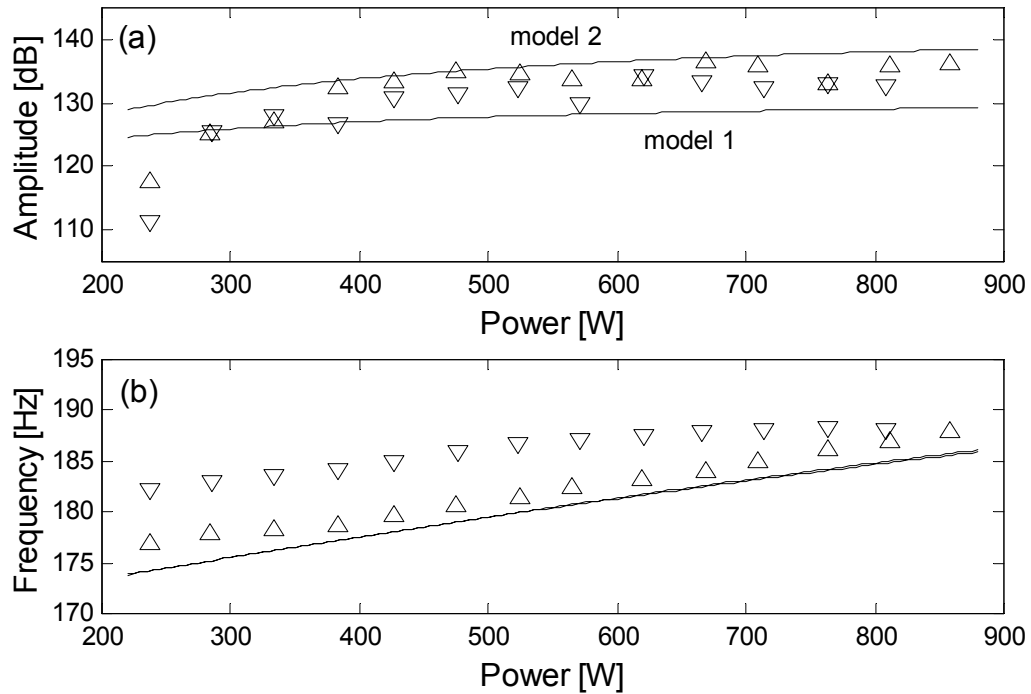


**Figure 6-7: Properties of the excited eigen acoustic mode at heater location  $x/L = 1/4$  and mass flow rate 1.63 gm/sec. Measured data:  $\Delta$ , power increase;  $\nabla$ , power decrease. Lines correspond to the results of modeling.**

regimes of operation of the Rijke tube are given in Figures 6-7 and 6-8 for heater location  $x/L = 1/4$  and two mass flow rates, which are fixed in individual runs. The amplitude and frequency of the excited mode are shown versus power supplied. The goal of comparison between the calculated and experimental results is to check how well the limit cycle properties are modeled in regions far from the stability boundaries. Trends in amplitudes and frequencies are predicted correctly. The amplitudes predicted with model 2 (Equation 6-13), in which the nonlinear modification of the transfer function is greater, are more accurate than those found with model 1 (Equation 6-2), which underpredicts the values. Both models produce nearly the same frequency, which is close to the experimentally recorded frequency corresponding to increasing power. The difference in experimental data for opposite directions of power variation is caused mainly by the thermal inertia of the system; the average temperature was higher as the power was

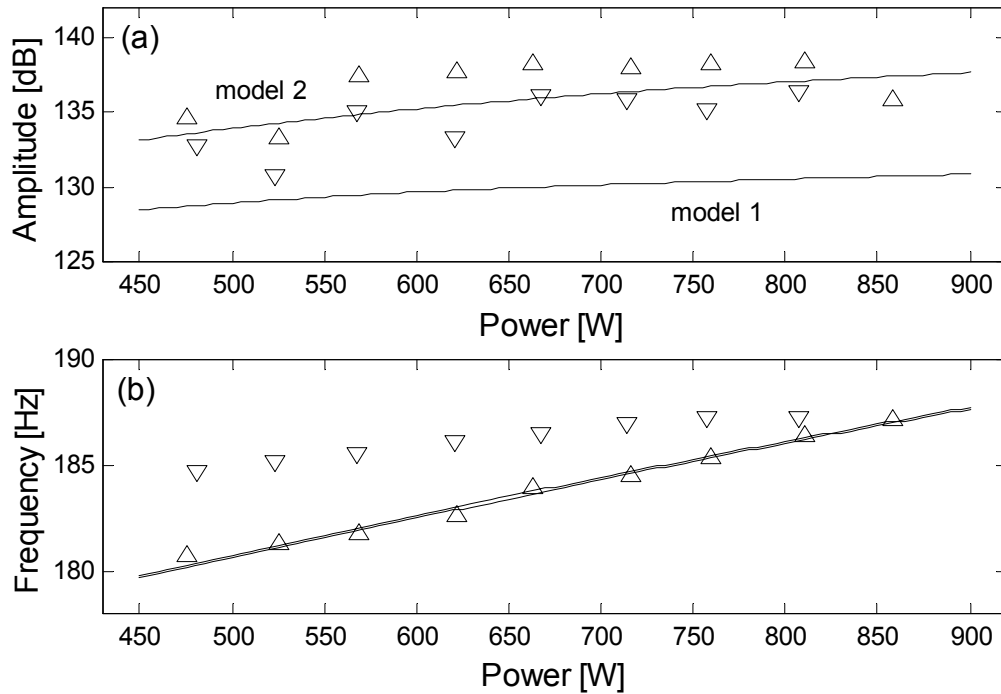


**Figure 6-8: Properties of the excited eigen acoustic mode at heater location  $x/L = 1/4$  and mass flow rate 2.40 gm/sec. Measured data:  $\Delta$ , power increase;  $\nabla$ , power decrease. Lines correspond to the results of modeling.**

decreased, causing higher frequencies.

The calculated and experimental results for the limit-cycle properties of the self-excited mode at heater location  $x/L = 5/8$  are shown in Figure 6-9 for two mass flow rates. At these system conditions, the excitable mode is the second eigen acoustic mode of the tube, and its frequency is about twice as big as that of the first mode. The errors are larger than those for heater location  $x/L = 1/4$ , probably due to inaccuracies in both acoustic modeling at high frequencies and thermal analysis at high temperatures (when thermal radiation becomes more important). Although the model predicts satisfactorily the maximum level of pressure magnitude in the excited state, it does not capture the amplitude variation with power supplied as seen in the test data. The tendency in the frequency behavior is modeled well, but the numerical value is underpredicted by a few percent.

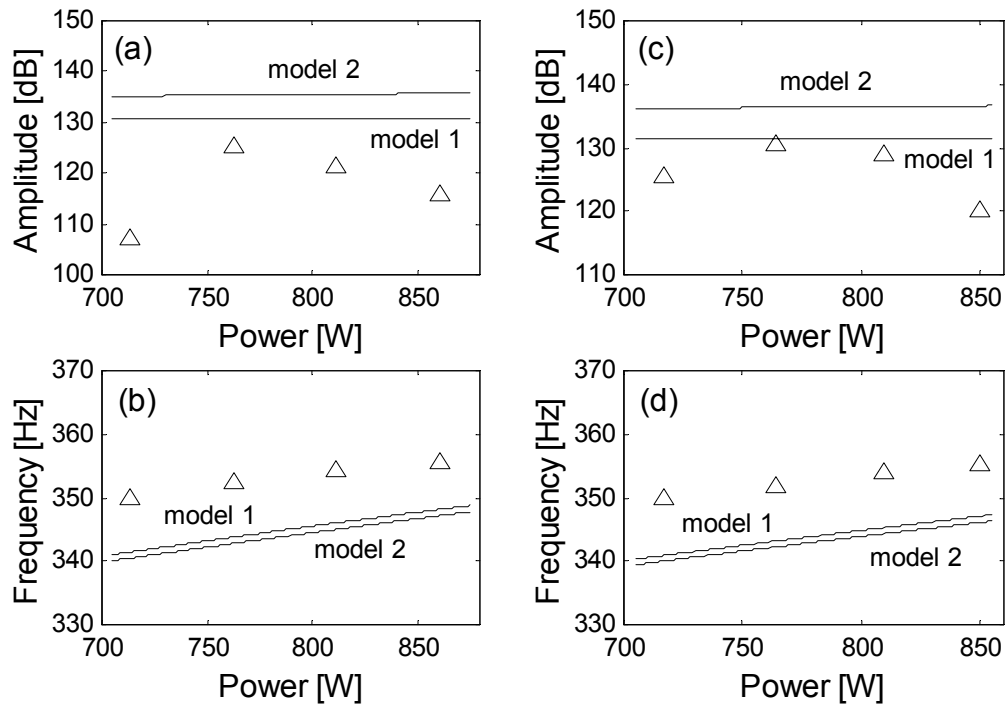


**Figure 6-9: Properties of the excited eigen acoustic mode at heater location  $x/L = 5/8$ . Mass flow rate: (a) and (b) 2.05 gm/sec; (c) and (d) 2.20 gm/sec. Measured data:  $\Delta$ , power increase;  $\nabla$ , power decrease. Lines correspond to the results of modeling.**

## 6.6 Simplified theory for higher harmonics

During the tests, higher harmonics of the excited mode were noticeable in the pressure signal. Since the major nonlinear mechanism in the Rijke tube is related to the heat release, we believe that the nonlinear response of the heater to the first mode velocity fluctuation results in the appearance of acoustic limit cycles with frequencies higher than that of the self-excited mode. The amplitude of the heat release fluctuating at higher frequencies can be estimated by Equation (6-12). Those limit cycles are *driven* by the first mode. An accurate model for finding the properties of higher harmonics would be difficult to construct given the uncertainties in the real system. However, estimations for the amplitudes and frequencies of the limit cycles in the

unstable regime can be easily obtained, introducing several approximations and using a modal analysis.

The major simplified assumption is a uniform temperature field inside a Rijke tube. In this case, the wave equation for the pressure fluctuation is

$$(6-15) \quad \frac{\partial^2 p'}{\partial t^2} + \zeta \frac{\partial p'}{\partial t} - a^2 \frac{\partial^2 p'}{\partial x^2} = (\gamma - 1) \frac{\partial \dot{Q}}{\partial t},$$

where  $\zeta$  is the generic damping (in our case due to the boundary layer on the tube walls and sound radiation);  $a$  is the speed of sound;  $\dot{Q}$  is the heat addition rate per unit of volume. The expansion of the pressure perturbation through acoustic modes is employed (Culick 1976), considering both tube ends open:

$$(6-16) \quad p' = \sum p'_n = \sum B_n e^{in\omega t} \sin(k_n x),$$

where  $k_n = n\omega / a$  is the wave number and  $B_n$  is the complex amplitude of the  $n^{\text{th}}$  mode;  $\omega$  is the frequency of the first mode. We assume that each acoustic mode reacts predominantly to forcing having frequency equal to the natural frequency of this mode. Equation (6-16) is substituted into (6-15), which is then multiplied by  $\sin(k_n x)$  and integrated over the tube length  $L$ . By using orthogonality of the eigen modes, the approximate equation for the amplitude of an individual mode is derived

$$(6-17) \quad i\xi_n n\omega B_n e^{in\omega t} \frac{L}{2} = (\gamma - 1) \int_0^L \frac{\partial \dot{Q}_{n\omega}}{\partial t} \sin(k_n x) dx,$$

where  $\dot{Q}_{n\omega}$  is the unsteady (sinusoidal) heat transfer rate having frequency  $n\omega$ . This heat addition consists of two components: the first is generated by acoustic motion of frequency  $n\omega$  (Equation 6-3); the second is due to the appearance of higher harmonics  $\dot{Q}_n$  in the unsteady heat transfer rate caused by the unstable mode (Equation 6-12). Therefore,  $\dot{Q}_{n\omega}$  can be expressed by the formula:



$$(6-18) \quad \dot{Q}_{n\omega} = \frac{\delta(x-l_g)}{S} \left( \dot{Q}_0 Tr \frac{u'_{n\omega}}{u_0} + \dot{Q}_n e^{in\omega t} \right),$$

where  $\delta(x)$  is a delta function;  $S$  is the cross-section area of the tube; and  $l_g$  is the heater location. Acoustic velocity is related to pressure perturbation as  $u' = ip'_x / \rho_0 \omega$ . Equation (6-18) can be transformed as follows

$$(6-19) \quad \dot{Q}_{n\omega} = \theta_n \frac{\partial p'_{n\omega}}{\partial x} \delta(x-l_g) + \frac{\dot{Q}_n}{S} e^{in\omega t} \delta(x-l_g),$$

where

$$(6-20) \quad \theta_n = i \frac{\dot{Q}_0}{m\omega_n} Tr(\omega_n, \alpha_n),$$

where  $m$  is the mass flow rate;  $\alpha_n$  is the nonlinear parameter associated with the amplitude of the  $n^{th}$  harmonic. Substituting Equation (6-19) into (6-17), we obtain

$$(6-21) \quad i\xi_n n\omega B_n e^{in\omega t} \frac{L}{2} = (\gamma - 1) \left( \theta_n \frac{\partial^2 p'_{n\omega}}{\partial t \partial x} \Big|_{x=l_g} \sin(k_n l_g) + in\omega \frac{\dot{Q}'_n}{S} e^{in\omega t} \sin(k_n l_g) \right).$$

The damping coefficient  $\xi_n$ , due to sound radiation from the open tube ends and boundary layer losses, is estimated with the standard formula (Howe 1998):

$$(6-22) \quad \xi_n = \frac{1}{\pi} \frac{\omega_n^2 S}{La} + \frac{1}{\sqrt{2}} \frac{\Pi \sqrt{\omega_n}}{S} (\sqrt{\nu} + (\gamma - 1)\sqrt{\chi}),$$

where  $\Pi$  is the perimeter of the tube cross section;  $\nu$  is the kinematic viscosity; and  $\chi$  is the thermal diffusivity. From Equations (6-16) and (6-21) it follows that the amplitude of the  $n^{th}$  harmonic is

$$(6-23) \quad B_n = \frac{2(\gamma - 1)\dot{Q}_n \sin(k_n l_g)}{S(\xi_n L - (\gamma - 1)\theta_n (|B_n|)k_n \sin(2k_n l_g))}.$$

The amplitudes of harmonics are found by solving this equation iteratively.

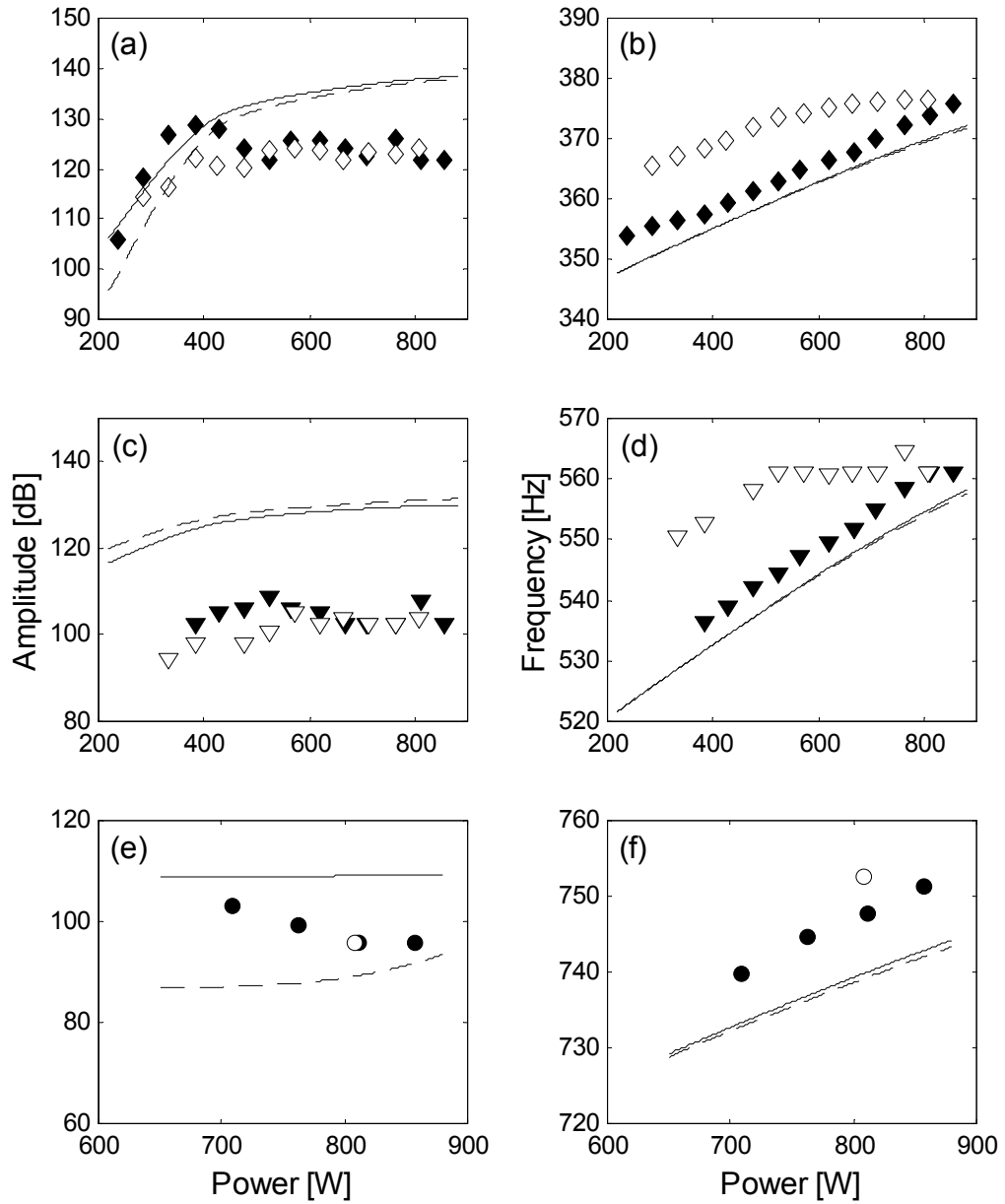


**Figure 6-10: Properties of higher harmonics of the excited mode at heater location  $x/L = 1/4$ , and mass flow rate 1.63 gm/sec. Measured data:  $\diamond$ , second harmonic;  $\nabla$ , third harmonic;  $\circ$ , fourth harmonic. Marked symbols correspond to power increase; empty symbols to power decrease. Solid line, model 1; dashed line, model 2.**

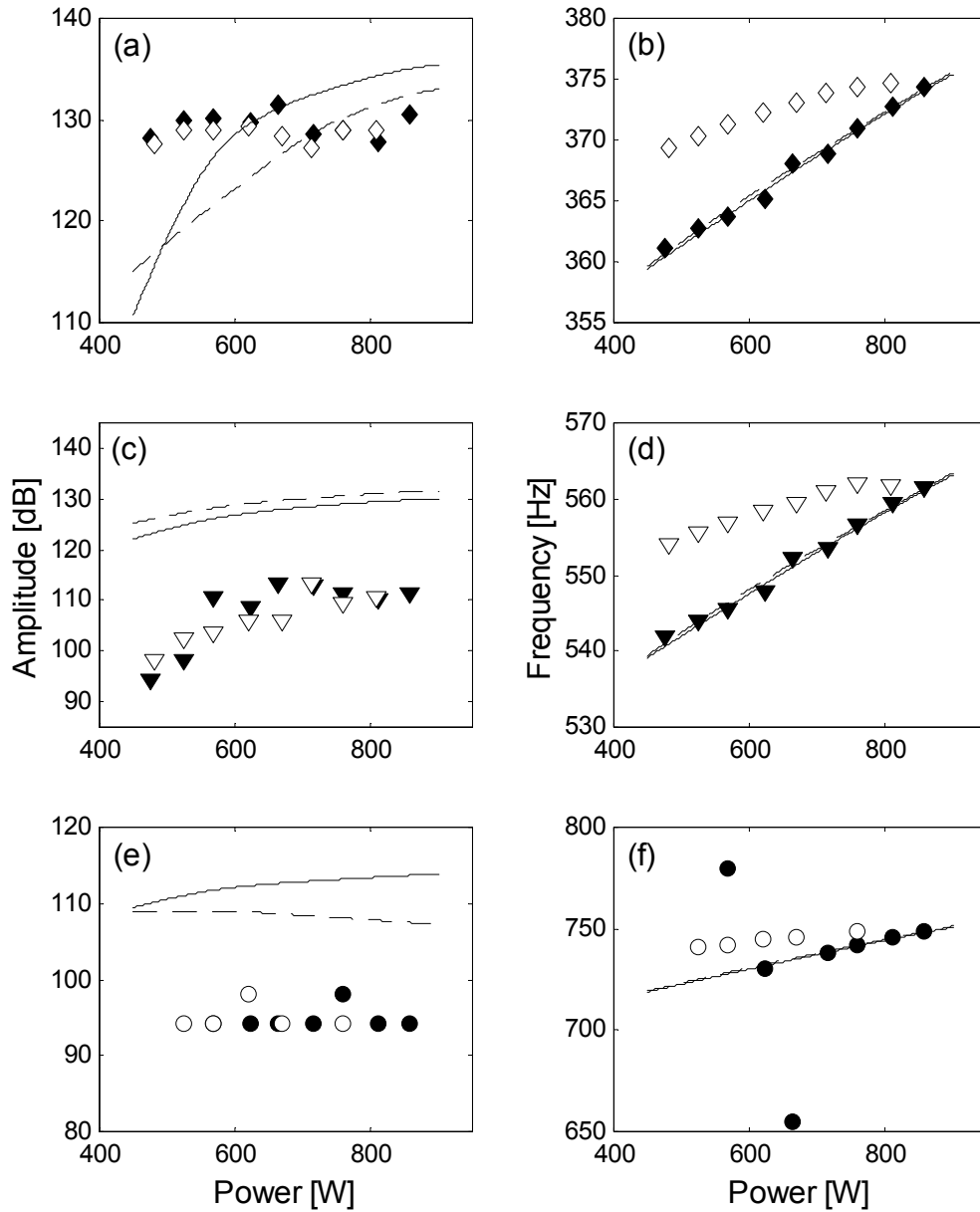


**Figure 6-11: Properties of higher harmonics of the excited mode at heater location  $x/L = 1/4$ , and mass flow rate 2.40 gm/sec. Measured data:  $\diamond$ , second harmonic;  $\nabla$ , third harmonic;  $\circ$ , fourth harmonic. Marked symbols correspond to power increase; empty symbols to power decrease. Solid line, model 1; dashed line, model 2.**

The results of the modeling, as well as experimental data, are shown in Figures 6-10 and 6-11 for the amplitude and frequencies of three higher harmonic of the excited mode for the heater location  $x/L = 1/4$ . The discrepancy between theoretical and test results is greater than that for the self-excited mode. The most likely reasons for inaccuracies are the approximations used: the temperature field uniformity; the simplified model for the amplitudes of high frequency heat release components (Equation 6-12); the absence of coupling between non-orthogonal modes; and the assumption that a tube diameter is much less than a sound wavelength. However, since the harmonics of a self-excited mode are usually of secondary importance due to their relatively small magnitudes, this theory can be considered satisfactory for rough estimations of high frequency components in the signal.

## Chapter 7

# Concluding Remarks

This work has been carried out with two primary intentions: 1) to obtain accurate data for the stability boundary and the limit cycles of thermoacoustic oscillations in the Rijke tube; and 2) to develop a theory that could predict the transition to instability and explain the nonlinear phenomena observed in the tests.

For the purpose of obtaining data for a broad range of system parameters, a horizontally oriented Rijke tube with mean flow provided by a fan and heat addition from a movable electrically heated gauze is employed. In this way, the three main system parameters – heater location, air flow rate, and power supplied – can be varied and controlled independently. To generate reproducible experimental results convenient for mathematical modeling, a quasi-steady data acquisition procedure was established: for fixed heater location and flow rate, the power is varied slowly enough to minimize the effects of unsteadiness of the temperature field in the system and of finite power increments that could cause nonlinear triggering of instability. To accomplish the experiment in reasonable time, an iterative method is employed to control the

power supplied: large power increments are used for rough determination of the stability boundary, and fine steps near the boundary vicinity are utilized for accurate localization of the transition between stable and excited states.

The stability boundary has been obtained for three characteristic heater locations ( $1/4$ ,  $1/8$ , and  $5/8$  of the tube length from the upstream tube end) favorable for excitation of the lowest eigen acoustic modes of the pipe. An unexpected experimental result was the observation of apparent hysteresis in the stability boundary at certain ranges of system parameters: the stability boundary is dependent on the direction of power variation at high mass flow rates at heater location  $x/L = 1/4$ , and at any flow rates at  $x/L = 5/8$ . That means that two stable states (either excited or with no oscillations) can exist at the same values of the main system parameters, and the choice of a particular state depends on the history of the experiment. The properties of the limit cycles have been quantified for the unstable domains of operation of the Rijke tube. Significant axial temperature variations along the pipe in both stable and excited regimes were measured during the tests. That shows the necessity of accounting for this effect in mathematical modeling, which was usually neglected in the previous works on Rijke tubes.

To predict the onset of thermoacoustic oscillations a linear acoustic theory has been formulated. Owing to the very low Mach number of the mean flow, interactions between the mean flow and the oscillating field are ignored, except the heater response to flow disturbances. Since the horizontal dimension of the heating element is small, jump conditions involving the transfer function of the heater are applied. To obtain satisfactory theoretical results, it is essential to account for the axial variations of the temperature, and a thorough thermal analysis is carried out to determine the temperature field. The computed results are in quite good agreement with the stability boundaries observed. Larger errors in the predicted stability boundary are introduced by commonly used simplified theories, assuming, for instance, the uniformity of the temperature along the tube. Errors at the extreme conditions (high and low flow rates, and high power range)

may be due to inaccurate representation of the transfer function of the heater, approximations in thermal analysis, and air leakage during the tests.

A rather simple theory is proposed in this thesis for the nonlinear modeling of a complex thermoacoustic phenomenon in the presence of a mean flow. The results confirm the speculation that the nonlinear behavior of Rijke tubes of the sort investigated in this work is dominated by nonlinear characteristics of heat transfer from the source of the instabilities. Two models for nonlinear heat transfer modifications, distinctive from each other when the acoustic velocity amplitude exceeds the mean flow velocity, are used. A quasi-steady assumption for the mean heat transfer rate is invoked, and a hypothesis for the general form of the heater transfer function that accounts for finite flow disturbances is proposed. This theory demonstrates satisfactory agreement with experimental results for two locations of the heating element, corresponding to the different excitable modes of the Rijke tube. Discovered experimentally, the hysteresis effect in the transition between stable and excited states is explained theoretically. Overestimation of the hysteresis gap between critical powers is attributed to the presence of the noise in the flow that can trigger early transitions between different states in the system. Limit-cycle properties of higher harmonics of a self-excited mode can be estimated using a simplified theory based on modal analysis and assuming uniform temperature field.

The results obtained in this work suggest that the approach developed should be applicable to assessing the stability of motion and the limit cycles in other thermal devices, such as combustion driven Rijke tubes, combustors, and thermoacoustic engines, if the Mach number of the average flow is small. Two generally important points must be emphasized: 1) nonuniformities of the temperature field significantly affect the stability boundaries; 2) as always in the case for unsteady behavior in combustion systems, the greatest unknown is the interaction (feedback) between the unsteady motion and the source of energy. The behavior of the Rijke tube observed and explained here clearly confirms these points.

The model developed is recommended for approximate analysis and preliminary design of the thermal devices where thermoacoustic instability is a concern. For more accurate knowledge of the process in a particular real-world system, a sophisticated CFD study or detailed experiments must be carried out.

Another problem having a thermoacoustic origin and important for rocket engines and various burners has been considered in this work. Interactions between vortex shedding, combustion and chamber acoustics may lead to the appearance of large pressure oscillations. Better understanding of the complex nature of this phenomenon, which is a type of combustion instability, can be achieved by applying the apparatus of dynamical systems to the simple reduced-order model offered here. Two novel ideas are introduced: 1) the criterion for vortex shedding, based on the quasi-steady hypothesis, and 2) application of the kicked oscillator model for analysis of this type of combustion instability. The vortex shedding sub-model is partly validated, producing the lock-in effect in vortex shedding as observed in experiments carried out elsewhere. The second idea, application of the kicked oscillator model, allows us to work out a fast and inexpensive calculation giving results that are easily interpreted. An important factor for accurate modeling is the inclusion of a sufficient number of modes into the simulation. Recommendations are given for modal truncation in the system considered. The model developed here can be further extended, including various additional physical effects. It is capable of simulating interesting nonlinear phenomena such as mode coupling, lock-in, hysteresis, and chaos, which are observed in real combustors.

To apply this theory for analysis of actual combustors, accurate identification of system parameters is needed. Determination of the system modes, acoustic losses, and vortex combustion properties is required. Some systems, where pulse burning occurs prior to complete separation of a vortex from a flameholder, are not suitable for modeling by the theory in its present state. However, we believe that the model can be developed to treat a wide variety of combustion instability problems.



## Appendix

# A Model for Combustion Instability in the Systems with Vortex Shedding

### A.1 Introduction

Combustion of reactants in a confined volume may be accompanied by the development of significant pressure oscillations. If these oscillations appear due to unsteady heat release, they are usually called a combustion instability. According to Rayleigh's criterion (Rayleigh 1945), an acoustic-thermal instability is encouraged if the heat release fluctuates in phase with the pressure perturbation. In combustion systems where vortex shedding may take place, for instance ramjet engines, afterburners, and solid-fuel motors, combustion instabilities are common phenomena. This effect has long been recognized as a serious problem in propulsion systems (Culick 1988). In recent years, specially designed pulsed combustors have also been built to take advantage of combustion instability due to vortex formation (Bai et al. 1993).

Early observations of vortex shedding from flameholders were reported by Kaskan and Noreen (1955) and Rogers and Marble (1956). Since the 1980's a number of experimental investigations have been accomplished, studying the role of vortex shedding on the acoustic instability inside

premixed type combustors (e.g., Smith and Zukoski 1985, Hedge et al. 1986, Poinso et al. 1987, Schadow et al. 1989, Yu et al. 1991, Sterling and Zukoski 1991, Zsak 1993, Kendrick 1995, Cohen and Anderson 1996). These works demonstrated that the dominant mechanism in the development of instability is due to the coupling between the acoustic field and periodic energy released by combustion of shed vortices, consisting initially of unmixed cold reactants and hot products. Another possible reason for the appearance of pressure oscillations in combustion chambers is the impingement of vortices on downstream obstacles, when vortices consist of combustion products only. This effect has been also thoroughly investigated (e.g., Culick and Magiawala 1979, Brown et al. 1981, Flandro 1986, Jou and Menon 1990). This is a purely acoustic phenomenon, not associated with unsteady heat release caused by combustion, and is not a subject of this study. We will assume that an acoustic source due to vortex collision with a structure has much smaller effect than that produced by vortex combustion.

Under certain circumstances determined by the velocity field and the system geometry, vortices are formed behind flameholders on the boundary of the recirculation zone. They entrain unburnt mixture on one side of the interface with the combustion products on the other side. Aimed at resolving a question how the rate of combustion of the vortex varies as the vortex rolls up and propagates downstream, theoretical studies have been undertaken (Marble 1984, Karagozian and Marble 1986, Laverdant and Candel 1989). The results have not clearly demonstrated pulse-like combustion that was observed in experiments; therefore, the impingement of a vortex on a solid structure (e.g., on chamber walls or restrictors), which greatly enhances mixing process, seems to be an important mechanism in most cases of this type of combustion instability.

With increasing computing power, it became possible to incorporate combustion and chamber acoustics into CFD codes, and numerical modeling of combustion-vortex-acoustics interactions were accomplished (e.g., Kailasanath et al. 1991, Bauwens and Daily 1992, Najm and Ghoneim 1993). At the present time, Large-Eddy Simulation is the most powerful technique for simulation of this type of combustion instability (Angelberger et al. 2000, Fureby 2000), and it is expected

to provide better understanding of such a complex phenomenon under various operating conditions of combustors.

Both experimental and CFD studies deliver valuable information on combustion instabilities. Nevertheless, both approaches are quite expensive, time-consuming, and the results obtained are usually applicable only to particular geometries. For those reasons, and for possible use in applications of active feedback control, a reduced-order modeling, capable of producing estimates of combustion instabilities in a rapid and inexpensive manner, has attracted attention despite a significantly simplified treatment of the problem. Culick (1988) proposed an idea of instantaneous burning of localized vortices in premixed type combustors involving vortex shedding, so that the unsteady heat release can be modeled by delta functions in space and time. Sterling (1993) formulated a discrete theory for combustion instability based on two models: delayed combustion response and twice-kicked oscillator. Only one acoustic mode was considered. It was shown that with variation of model parameters, the periodic limit cycles undergo subharmonic bifurcations and transition to chaos. However, these theories are essentially incomplete due to lack of a reasonable and sufficiently simple model (consistent with the goal of reduced order) for vortex shedding in the unsteady flow.

A combustion instability involving vortex shedding is affected mainly by four factors: chamber acoustics, unsteady combustion, hydrodynamics (vortex shedding), and the reactant supply system. In this paper we will not consider the last component, then the interaction between major effects can be schematically represented as shown in Figure A-1. Vortices originating from unstable shear layers are shed downstream in the chamber. They can burn vigorously after a certain induction time, determined either by the moment of vortex impingement on a structure or by characteristic combustion times. This transient burning acts as a source for excitation of acoustic modes of the chamber. The resulting oscillatory flow affects the vortex shedding process, modifying the shedding frequency and intensities of the vortices. Therefore, a feedback loop is formed that can destabilize the system. The steady-state equilibrium is reached when the

energy gained from the burning compensates the acoustic losses. It is achieved either by nonlinear combustion or by nonlinear acoustic losses.

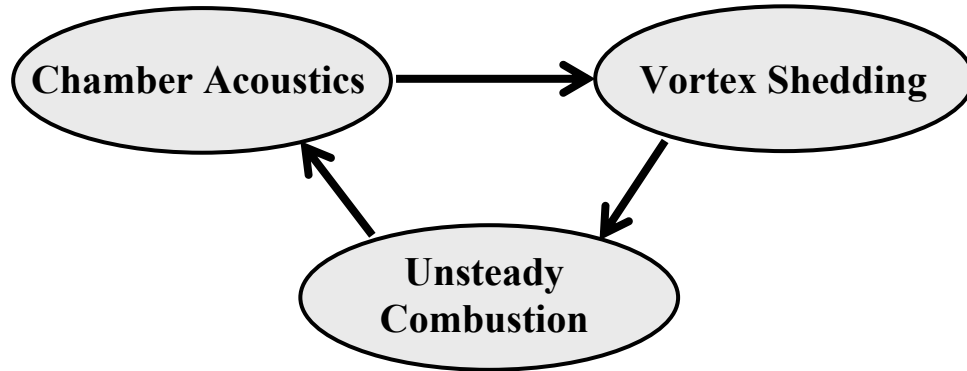


**Figure A-1: Acoustic / vortex / combustion interactions.**

In this Appendix we will derive a dynamical system according to the scheme in Figure A-1. Flow fluctuations are represented through eigen acoustic modes. The source for perturbations is vortex burning. A novel model for vortex shedding in unsteady flows is introduced, using a hypothesis of quasi-steady behavior to determine the moment of vortex separation. This model can be applied to a much larger variety of hydrodynamic problems involving vortex shedding in time-dependent flows than those relevant to this study, i.e., with heat release due to combustion. In this way, all important processes in the systems – chamber acoustics, vortex shedding, and unsteady combustion – are interconnected. Applying boundary and initial conditions, and treating geometrical and chemical properties as parameters, the system dynamics can be calculated. Results of one simulation will be presented and discussed in Section A-3.

## A.2 Theory

A dump combustor is considered as the configuration for studying combustion instabilities involving vortex shedding (Figure A-2). This geometry is motivated by the works of Zukoski's group (Smith and Zukoski 1985, Sterling and Zukoski 1993, Zsak 1993, and Kendrick 1995). However, our model can also be applied to other configurations, such as combustors with cavities (Najm and Ghoneim 1993), with baffles or other downstream obstacles. In the case of stable flow, a recirculation zone filled by hot products is formed behind the rearward-facing step. Products mix with cold reactants, heating them and supporting stable distributed combustion. At certain flow velocities the shear layer at the lip becomes unstable, and vortex formation occurs. Shed vortices can impinge on structural components of a combustor downstream of the expansion; for the case shown in Figure A-2, it is a lower wall in the chamber. That greatly enhances mixing between the cold and hot components resulting in vigorous burning of the vortex. Alternatively, a vortex can burn intensively after a certain induction time determined by the characteristic hydrodynamic and chemical times (Keller et al. 1990).

The major assumptions used in the mathematical formulation are the following:

- Only longitudinal acoustic modes are important; i.e., one-dimensional acoustic theory can be applied.
- The Mach numbers of both the mean and oscillating flows are small, and their effects on acoustics are neglected.
- Vortex burning is the only source of unsteady heat addition; and its influence on acoustics greatly exceeds that due to collision of vorticity with a solid structure.
- Non-uniformity in the temperature field and variation of the combustor cross-section area are neglected.
- During the vortex formation stage, a vortex does not move significantly in comparison with its displacement after detachment up to the impingement point.

- Combustion occurs only at the moment of collision.

The first four assumptions are not significantly restrictive; they can be relaxed, and the model can be easily extended further. For clarity of presentation, we derive a theory within these limitations. The last two assumptions make the model applicable to a narrower class of problems than that characteristic of real-world devices. However, certain adjustments can probably be made to overcome these limitations as well.

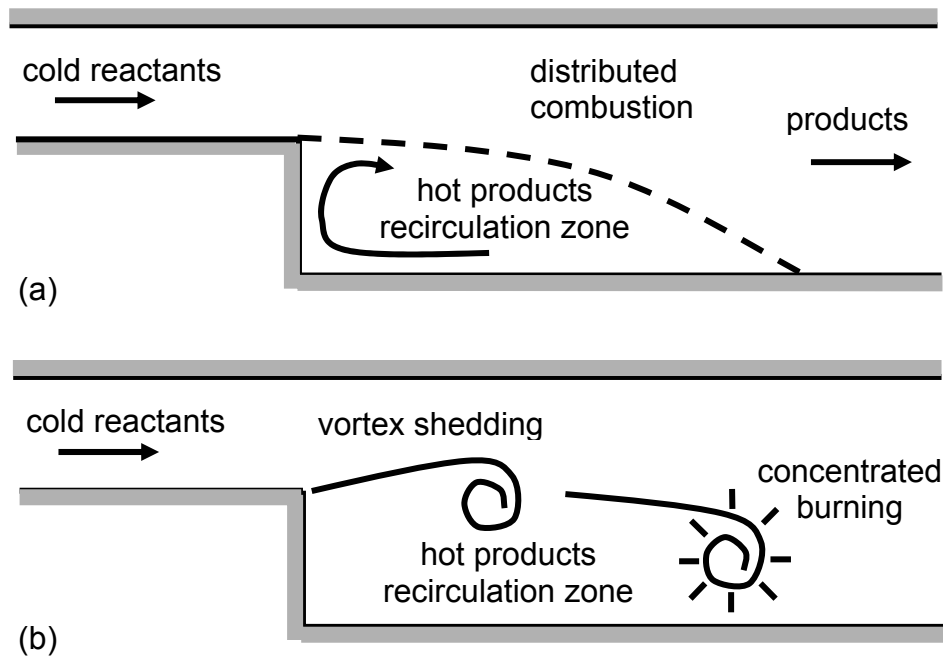


**Figure A-2: Stable (a) and unstable (b) flow in dump combustor.**

A one-dimensional wave equation for the pressure fluctuation  $p'$  in a uniform medium in the absence of losses and with a forcing term due to heat release is

$$(A-1) \quad \frac{\partial^2 p'}{\partial t^2} - a^2 \frac{\partial^2 p'}{\partial x^2} = (\gamma - 1) \frac{\partial \dot{Q}}{\partial t},$$

where  $a$  is the speed of sound, and  $\dot{Q}$  is the heat addition rate per unit volume. For boundary conditions, the chamber ends are considered open, i.e.,  $p'(0, t) = p'(L, t) = 0$ . All direct effects of the mean flow on the acoustic field are ignored.

The expansion of pressure and velocity perturbations through eigen acoustic modes is employed (Culick 1976):

$$(A-2) \quad p'(x, t) = \sum p'_n(x, t) = p_0 \sum \eta_n(t) \psi_n(x),$$

$$(A-3) \quad u'(x, t) = \sum u'_n(x, t) = \sum \frac{\dot{\eta}_n(t)}{\gamma k_n^2} \frac{d\psi_n(x)}{dx},$$

where  $p_0$  is the mean undisturbed pressure;  $\eta_n(t)$  is the time-varying amplitude of the  $n^{\text{th}}$  mode;  $\psi_n(x)$  is the mode shape;  $\gamma$  is the gas constant; and  $k_n$  is the wave number. For boundary conditions considered here, mode shapes are  $\psi_n(x) = \sin(k_n x)$ , and wave numbers are  $k_n = n\pi / L$ .

Equations (A-2) and (A-3) are substituted into Equation (A-1), which is then multiplied by  $\psi_n(x)$  and integrated over the chamber volume. By using orthogonality of the eigen modes and introducing linear mode damping  $\xi_n$ , the dynamic equations for individual modes are derived,

$$(A-4) \quad \frac{d^2 \eta_n}{dt^2} + 2\xi_n \omega_n \frac{d\eta_n}{dt} + \omega_n^2 \eta_n = \frac{\gamma - 1}{pE_n^2} \int \psi_n \frac{\partial \dot{Q}}{\partial t} dx,$$

where  $E_n^2 = \int \psi_n^2 dx$ .

The larger the vortex circulation, the more reactants are entrained into the vortex; therefore, at the moment of vortex burning at its impingement, the greater is the energy release. For modeling purposes, we assume the energy release to be proportional to vortex circulation  $\Gamma$ . Assuming vortex burning to occur instantaneously, and the size of the vortex to be small in comparison with

other characteristic dimensions in the system, the heat addition rate can be expressed using delta functions in space and time,

$$(A-5) \quad \dot{Q} = \beta \sum \Gamma_j \delta(x - x_j) \delta(t - t_j),$$

where summation is carried over the number of shed vortices;  $\beta$  is an appropriate coefficient to be determined;  $x_j$  is the vortex location; and  $t_j$  is the moment of burning. The vortex location and burning instant are defined either by the time of vortex impingement on a downstream obstacle (e.g., a chamber wall or a restrictor) or by the induction time dependent on mixing and chemical properties of the flow. The velocity of a shed vortex depends on the total flow velocity at the vortex instant position. Since a vortex is moving along the boundary between the primary flow and the recirculation zone, its steady velocity component is lower than that of the primary flow. For example, vortices shed at the lip of the splitter plate separating two streams move at approximately the average speed of the streams. The vortex velocity is approximated by the formula

$$(A-6) \quad \dot{x}_j(t) = \alpha u_0(x_j) + u'(x_j, t),$$

where the coefficient  $\alpha$  is usually in the range 0.5-0.6 (Dotson et al. 1997).

Substituting Equation (A-5) into Equation (A-4), we find the dynamics equation for the  $n^{\text{th}}$  mode amplitude in time interval  $(t_{j-1}; t_{j+1})$ :

$$(A-7) \quad \ddot{\eta}_n + 2\xi_n \omega_n \dot{\eta}_n + \omega_n^2 \eta_n = c \psi_n(x_j) \Gamma_j \dot{\delta}(t - t_j).$$

Following Andronov et al. (1987), it can be shown that this system behaves as a usual oscillator in the interval  $(t_{j-1}; t_{j+1})$  except at the moment  $t_j$ , when the following jump conditions are fulfilled

$$(A-8) \quad \eta_n(t_{j+}) - \eta_n(t_{j-}) = c \psi_n(x_j) \Gamma_j,$$

$$(A-9) \quad \dot{\eta}_n(t_{j+}) - \dot{\eta}_n(t_{j-}) = 0.$$



Equations (A-8) and (A-9) mean that at the moment of vortex burning the amplitudes of the acoustic modes change discontinuously while their derivatives remain the same. Such a system is related to the family of ‘kicked’ oscillators.

In order to complete the mathematical formulation, the time of vortex separation and the vortex circulation need to be modeled. The essential feature of this problem is the presence of an unsteady flow, which greatly affects the vortex shedding process. In this section, we will derive and justify a simple reduced-order model for vortex shedding in unsteady flows. When the velocity of an incident flow is constant, regular vortex shedding behind bluff bodies is observed. The frequency of vortex separation is commonly expressed as

$$(A-10) \quad f_{s0} = St \frac{u_0}{D},$$

where  $St$  is the Strouhal number, nearly constant in certain ranges of the Reynolds number;  $D$  is the characteristic size, usually taken either as a boundary layer momentum thickness at the detachment point or as a body/nozzle diameter. Discussion of Equation (A-10) with respect to combustor geometries is given by Schadow and Gutmark (1992).

Following Clements (1973), the growth of the circulation of a vortex formed behind the step can be found as an integral over a boundary layer thickness of vorticity shed per unit of time from a separation edge:

$$(A-11) \quad \dot{\Gamma} = \int_0^{\delta} u \frac{\partial u}{\partial y} dy = \frac{1}{2} u_s^2,$$

where  $u_s$  is the flow velocity at the outer edge of the boundary layer. Both mean flow and shed vorticity, as well as its mirror reflection due to proximity to a solid body, contribute to this velocity. A portion of shed vorticity diffuses, not entering the formed vortex, which eventually detaches from a body. Assuming the mean flow velocity is dominant part of  $u_s$ , the average rate of circulation production can be approximated by

$$(A-12) \quad \bar{\Gamma} = \frac{1}{2} b u_0^2,$$

where the coefficient  $b$  accounts for the influence of the factors mentioned. When this influence is small,  $b$  can be taken equal to one. Then the circulation of a separated vortex is found by integrating Equation (A-11) over one period

$$(A-13) \quad \Gamma_{sep} = \int_0^{1/f} \frac{1}{2} u_0^2 dt = \frac{u_0 D}{2St}.$$

This result has the interpretation that the detachment of a vortex occurs at the moment when its circulation is equal to the critical value defined by Equation (A-13).

By analogy with Equation (A-13), we propose a quasi-steady hypothesis for vortex shedding in the flow with an oscillatory component: a vortex separation occurs when its circulation reaches the critical level defined by the momentary flow velocity  $u(t)$ ,

$$(A-14) \quad \Gamma_{sep}(t) = \frac{u(t)D}{2St},$$

where the total velocity is  $u(t) = u_0 + u'(t)$ ; and the Strouhal number  $St$  is the same as that in steady flow. Vorticity production is described by Equation (A-11), where velocity  $u_s$  is replaced by  $u(t)$ . Taking the coefficient  $b$  equal to unity implies that the hypothesis cannot be applied to pronounced antisymmetrical vortex shedding (e.g., from a cylinder in a cross flow), where two vortices of opposite circulations (with a certain phase shift) strongly affect each other's formation. However, in other cases (e.g., for vortices formed behind a step, baffle or ring), when the influence on the total velocity at the separation point by the shed vorticity can be weak, then the hypothesis is applicable.

In order to validate the proposed model for vortex shedding in oscillatory flows, comparison with appropriate experiments must be made. The characteristic feature of various systems with unsteady flows and vortex shedding is the existence of lock-in regimes, when a vortex separation

frequency  $f_s$  stabilizes near the forcing frequency  $f_p$ . The comparison will be made with results on vortex shedding from a ring in the oscillatory flow (Castro 1987). Two lock-in regions were observed experimentally, when the ratio  $f_p / f_{s0}$  of the oscillatory velocity frequency  $f_p$  in a forced flow to the natural vortex shedding frequency  $f_{s0}$ , corresponding to a steady flow with velocity equal to the mean velocity in pulsating flow, was equal to 1 and 2.

In this model, a flow starts from the state without any vortices, and integration in time is carried out until a steady state is achieved. In the absence of forcing, a vortex shedding frequency is equal to that defined by Equation (A-10). In oscillatory flows, it was found that the vortex shedding behaves in the way resembling that experimentally observed. Experimental and modeling results for the average steady-state shedding frequency are shown in Figure A-3 for the case when the ratio of the amplitude of an oscillatory component to the mean flow velocity is 0.05. Similar dependence is found for other values of the oscillating velocity component. The agreement between theoretical and experimental results is satisfactory; hence, the quasi-steady hypothesis proposed is appropriate at least for this system. Information suitable for comparison with mathematical modeling, on vortex shedding in oscillatory flows in other configurations that are also relevant to our study (step, baffle, etc.) and *without* coupling to the chamber acoustics (feedback) have not been reported in the literature; further experiments would be desirable to advance this model. Since the proposed hypothesis for vortex shedding is found to be reasonable, we include it in the dynamical system developed in this paper. Thus, the mathematical formulation for combustion instability involving vortex shedding is closed, and the model dynamics can be studied numerically by integrating the equations for mode amplitudes and for vortex formation, motion and burning.

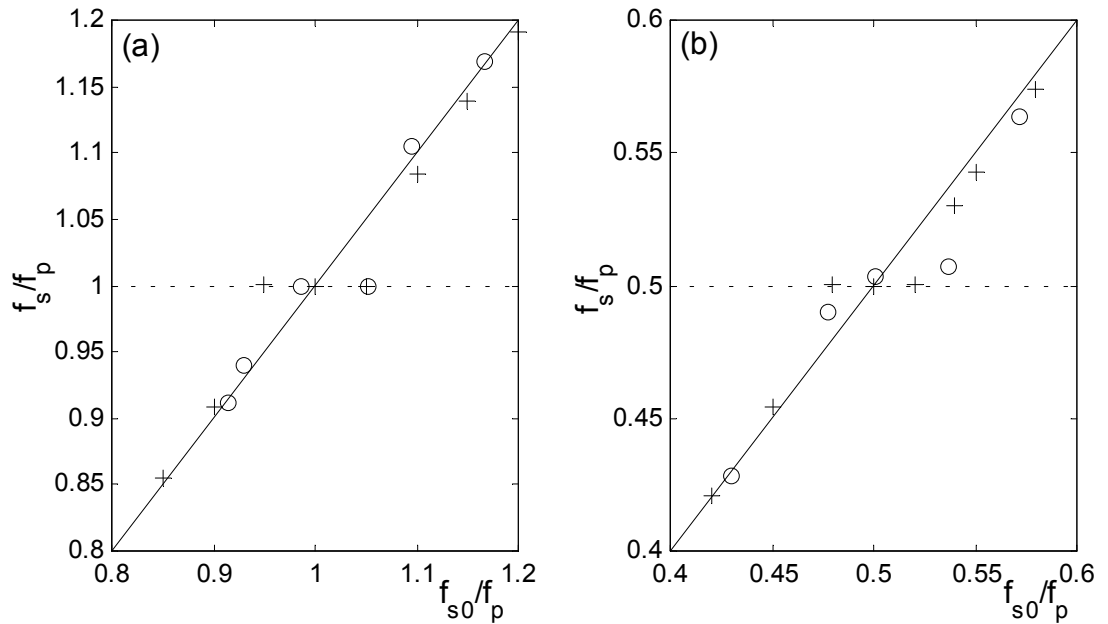


**Figure A-3: Lock-in regions: (a) around  $f_{s0}/f_p = 1$ ; (b) around  $f_{s0}/f_p = 0.5$ . (o) experimental data (Castro 1997); (+) modeling results. Solid lines have slope one.**

### A.3 Some results

In order to apply the model constructed in this Appendix to actual combustors with vortex shedding, it is necessary to assign values to all parameters. This procedure can be quite difficult due to the complex nature of combustion processes and the unavailability of necessary test data. Such system identification is beyond the scope of this study. Instead, some simulations have been carried out for arbitrarily selected but realistic system parameters.

Results will be given for a dump combustor, Figure A-2, having the following characteristics. The total chamber length is  $L = 2$  m; vortex separation occurs at  $L_1 = 0.85$  m from the upstream end; vortex burning at  $L_2 = 1.15$  m; ratio  $St/D$  is  $10 \text{ m}^{-1}$ ; the lowest natural frequency is 200 Hz; coefficients  $c$  and  $\xi_1$  are  $0.04 \text{ s/m}^2$  and 0.05, respectively, the sound speed is 800 m/s, and the coefficient for the vortex velocity  $\alpha$  is 0.5. The frequencies of higher modes are integral

multiples of the first mode frequency; the damping coefficients are proportional to the frequency. The chamber ends are acoustically closed, so that modes shapes are  $\psi_n = \sin(n\pi x / L)$ . The mean flow velocity is a variable parameter. At the speed 20 m/s the natural vortex shedding frequency in the steady flow coincides with the natural frequency of the lowest acoustic mode, and at 40 m/s the steady shedding frequency is equal to the second mode frequency. Limits on both minimum and maximum vortex circulations are imposed as 0.1 and 10 of the circulation corresponding to the steady flow. The low limit means that at low speed no vortex shedding occurs (stable flow); the high limit is due to finite system dimensions.

Equations for acoustic mode dynamics and vortex formation and motion are integrated with the time step  $1.25 \cdot 10^{-5}$  sec. Limit cycles are achieved after a finite time from initiation; typical time to reach steady-state regime is about 0.3 sec. Simulations are started without any flow perturbations or shed vortices. The model contains the mechanism of vortex generation in steady flow discussed in Section A.2. When shed vortices burn, pressure fluctuations appear, inducing velocity perturbations at the step edge. This acoustic component of the velocity modifies the process of vortex formation, completing a feedback loop in the system. In steady state, during one cycle, the energy transformed from heat release to the acoustics is equal to the acoustic losses.

For accurate representation of instability development, a sufficient number of modes must be included. The question of what number is sufficient is of great importance to the representation of combustion instabilities using reduced order modeling. Until recently, there was no convincing argument for how many modes should be retained in order to predict acoustic dynamics correctly. Ananthkrishnan et al. (2002) considered the problem of truncation for the system of nonlinearly coupled oscillators, which describes the development of acoustic waves in combustors, accounting for nonlinear gasdynamics. Based on the analysis of energy transfer between modes, it was shown that for correct results it was necessary to include three types of modes: linearly

unstable modes; those resonantly excited by unstable modes; and energy-sink modes. For example, if only the first mode is linearly unstable, then at least four modes must be included.

The analysis by Ananthkrishnan et al. (2002) is applicable to the systems consisting of continuous differential equations with small disturbances with gasdynamics the only nonlinear process accounted for. The problem considered in this paper does not satisfy those conditions, and another approach to the modal truncation question is needed. The source of perturbation in our system is vortex burning; hence, the characteristics of the vortices dominate the nonlinear behavior. The only factor that affects vortex generation in this model is the flow velocity at the lip (Equations A-11 and A-14). Therefore, the importance of an acoustic mode can be estimated by considering its contribution to the total velocity at that point. The location of the vortex burning with respect to the mode shape determines how effectively energy is pumped into the mode. High mode damping may prevent a mode from affecting the vortex formation significantly, even if its mode shape favorably correlates with the positions of vortex separation and burning. Combining these premises, we introduce a dimensionless parameter characterizing the importance of the  $n^{\text{th}}$  mode:

$$(A-15) \quad G_n = |\psi_n(L_2)| \cdot \left| \frac{1}{k_n} \frac{d\psi_n}{dx}(L_1) \right| \cdot \exp(-\xi_n k_n (L_2 - L_1)).$$

The first multiplier in Equation (A-15) is the absolute value of the  $n^{\text{th}}$  mode shape at the location of vortex burning (Equation A-8); the second multiplier relates to the mode contribution to the total velocity at the lip (Equation A-3); and the last multiplier estimates the loss of the mode amplitude for the time needed for sound to propagate from the point of vortex combustion to the point of vortex generation. The higher the parameter  $G_n$ , the greater the importance of the  $n^{\text{th}}$  mode. This proposition, however, cannot be considered rigorous; it does not take into account phasing between the mode amplitude and the events of vortex burning and detachment. Instead,

the parameter  $G_n$  can be thought as a simple and preliminary means for estimating the number of acoustic modes to be retained for correct representation of system dynamics.

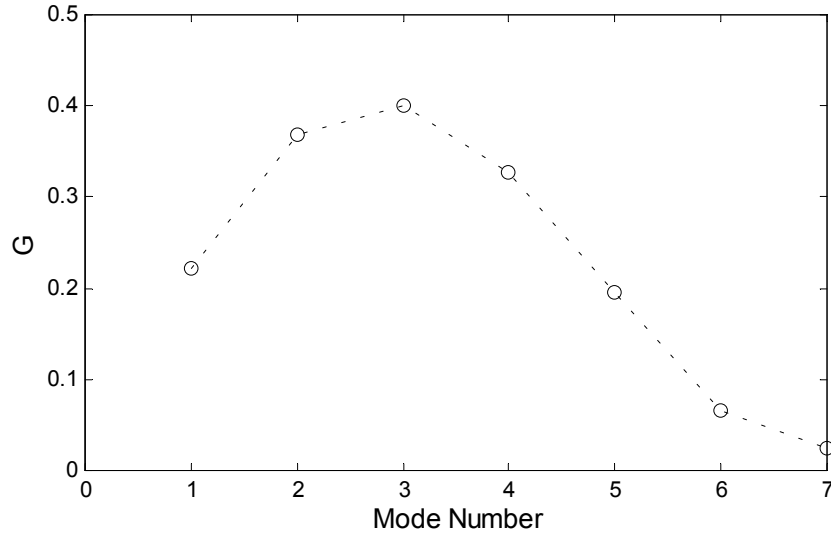


**Figure A-4: Coefficient of the mode importance.**

A recommendation for modal truncation can now be given. The mode having frequency closest to the vortex shedding frequency, evaluated at the mean flow velocity (Equation A-10), must be examined first. The parameter  $G_n$  for this mode is calculated by Equation (A-15). Higher modes with parameter  $G$  that is significantly lower than  $G_n$  can be discarded. This parameter goes asymptotically to zero with a frequency growth, since the first two multipliers in Equation (A-15) are usually of order of unity, and the exponent generally quickly decreases with a frequency. Therefore, only low modes usually need to be retained. For the given system parameters, coefficient  $G$  is computed and shown in Figure A-4 for the first seven modes. From this plot, we conclude that modes 3 and 4 can be potentially very important even at a low characteristic forcing frequency, which is a stationary vortex shedding frequency based on a low mean flow velocity. To achieve accurate results, modes 5 and 6 should also be accounted for.

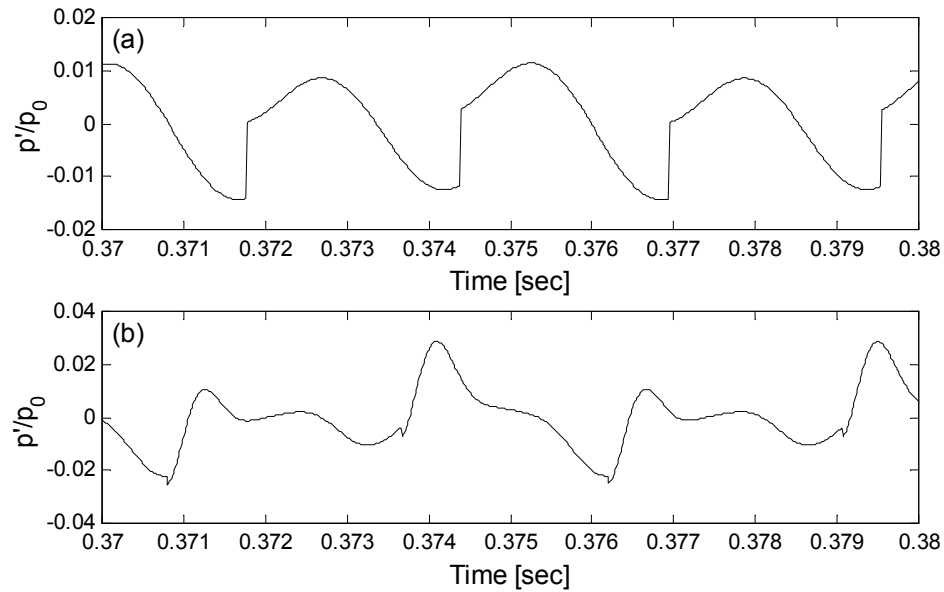


**Figure A-5: Pressure fluctuations near at the lip in the limit-cycle regime: (a) one-mode model; (b) six-mode model. Mean flow velocity 40 m/s.**

Numerical simulations have been carried out for one, two, four, and six modes. Examples of the waveform of the pressure fluctuation in the step edge vicinity at the limit-cycle regime are shown in Figure A-5 for a mean flow velocity 40 m/s and generated by the two-mode and six-mode models. As one can see, the waveforms are quite different for the two cases considered. In the first case (Figure A-5a), when only the two lowest modes are accounted for, the combustion kicks produce significant abrupt changes in the instant pressure. Discontinuous variation of pressure corresponds to the instant of vortex burning. These kicks cause the dominant frequency of oscillation to be near 385 Hz, which is close to the second mode natural frequency (400 Hz).

Despite a high level of the kicks (comparable with oscillation amplitude), it does not lead to further development of instability due to non-optimal phasing between pressure and heat release fluctuations. When six modes are taken into consideration (Figure A-5b), the waveform of the pressure fluctuation changes dramatically. The maximum level of pressure fluctuation increases nearly threefold. Two characteristic cycles with frequencies that are close to the natural



frequencies of the lowest modes, as well as high frequency components, are noticeable now. Individual combustion kicks produce much smaller discontinuous variations in the pressure signal; these jumps, however, are positioned so that thermal energy is effectively transformed into acoustic energy. Thus, Figure 6 demonstrates how large is the effect of the number of modes included in the analysis on the waveform of pressure fluctuation.

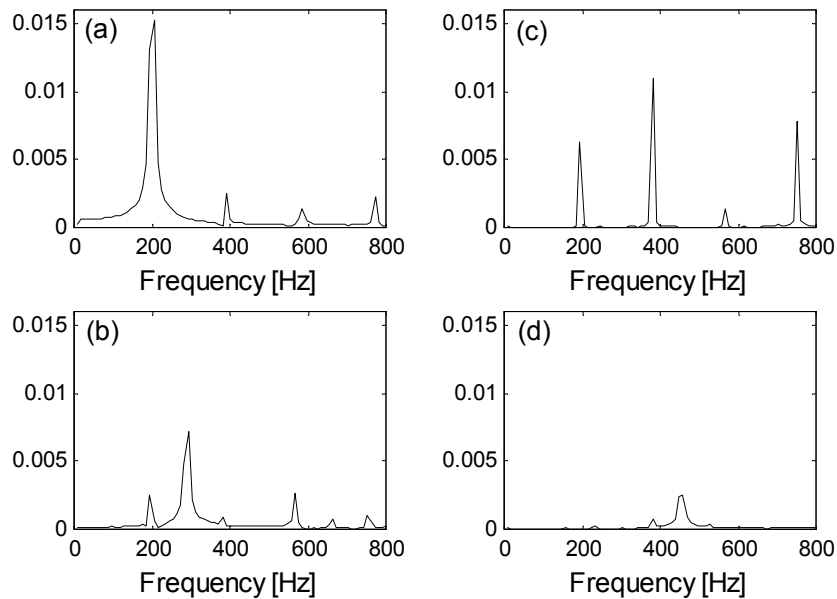


**Figure A-6: Amplitude spectra of the pressure fluctuation: (a) 20 m/s; (b) 30 m/s; (c) 40 m/s; and (d) 50 m/s.**

Spectra of limit cycles for six-mode simulations are presented in Figure A-6. A summary of results of numerical modeling for the variable number of modes and the mean flow velocity is given in Figure A-7, showing amplitudes of the spectral peaks of the pressure fluctuation signal in the limit cycles. The pressure is computed in the vicinity of the lip where vortex formation occurs. The range of the mean flow velocity is 20-50 m/s. In Figures A-7a and A-7b, the amplitudes of the signal components with frequencies near the natural frequencies of the first two modes are shown. The dominant spectral components observed at frequencies distant from the natural frequencies are given in Figure 8c. The number of modes noticeably affects the results. If

too few modes are selected, the accuracy can be significantly compromised, as especially seen from data corresponding to 40 m/s (Figures A-5 and A-7).

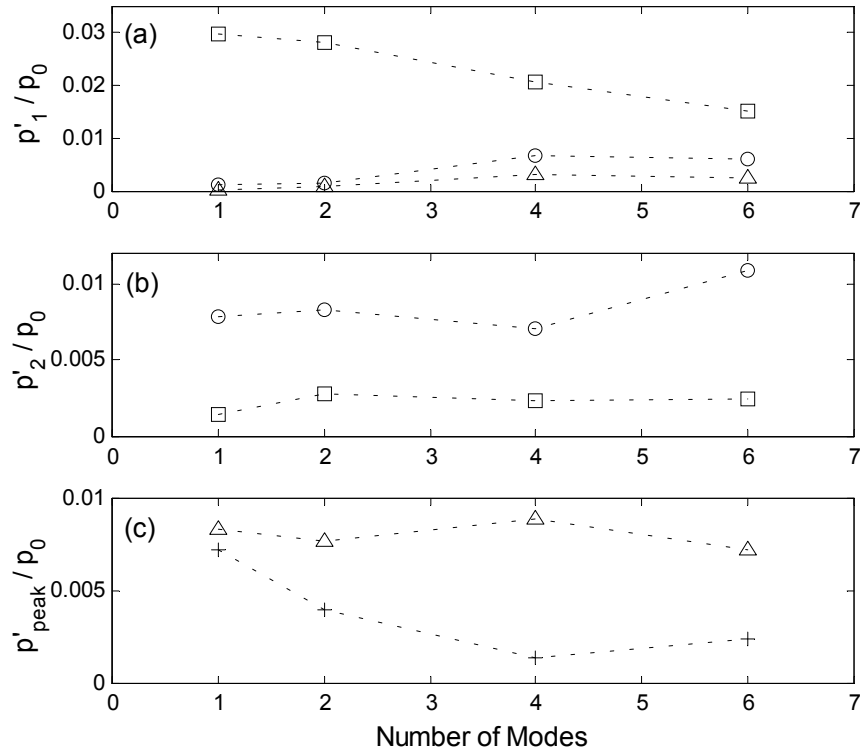


**Figure A-7: Amplitudes of the spectral peaks in steady-state regimes: (a) near the first mode natural frequency (200 Hz); (b) near the second mode natural frequency (400 Hz); (c) near 300 Hz ( $\Delta$ ) and near 500 Hz (+). Mean flow velocity:  $\square$  20 m/s;  $\Delta$  30 m/s;  $\circ$  40 m/s; and + 50 m/s.**

The amplitude of a low-frequency component of the pressure waveform is maximal for flow velocity 20 m/s, when the vortex shedding frequency in steady flow is close to the first mode natural frequency. For velocity 40 m/s, when the stationary vortex shedding frequency is a harmonic of the first mode frequency, the first mode magnitude is also pronounced. The similar effect is exhibited by the second mode (Figure A-7b); its amplitude is maximal at 40 m/s and significant at 20 m/s, when the second mode frequency is a subharmonic of the steady vortex shedding frequency. For velocities 30 m/s and 50 m/s, when a characteristic vortex shedding

frequency (estimated for a mean flow velocity) is distant from those corresponding to eigen acoustic modes, the dominant components in the fluctuating pressure appear at frequencies near 300 Hz and near 500 Hz, respectively (Figures A-6b,d and A-7c). It shows that combustion instabilities may emerge on frequencies that are far off the natural frequencies of the system. Although the individual modes do not possess these frequencies, the combustion kicks, producing phase jumps in the signal, cause the appearance of new frequencies. This phenomenon has been observed in experiments (Schadow and Gutmark 1992).

# References

- Ananthkrishnan, N., Deo, S., and Culick, F. E. C. (2002). Modeling and dynamics of nonlinear acoustic waves in a combustion chamber, *38th AIAA/ASME/SAE/ASEE Joint Propulsion Conference and Exhibit*, AIAA paper no. 2002-3592.
- Andronov, A. A., Vitt, A. A., and Khaikin, S. E. (1987, re-issue). *Theory of Oscillators*, Dover Publications, New York.
- Angelberger, C., Veynante, D., and Egolfopoulos, F. (2000). LES of chemical and acoustic forcing a premixed dump combustor, *Flow, Turbulence and Combustion* **65**: 205-222.
- Arpaci, V. S., Dec, J. E., and Keller, J. O. (1993) Heat transfer in pulse combustor tailpipes, *Combustion Science and Technology* **94**: 131-146.
- Bai, T., Cheng, X. C., Daniel, B. R., Jagoda, J. I., and Zinn, B. T. (1993). Performance of a gas burning Rijke pulse combustor with tangential reactants injection, *Combustion Science and Technology* **94**: 1-10.
- Bauwens, L. and Daily, J. W. (1992). Flame sheet algorithm for use in numerical modeling of ramjet combustion instability, *Journal of Propulsion and Power* **8**: 264-270.

- Bayly, B. J. (1985). Heat transfer from a cylinder in a time-dependent cross flow at low Peclet number, *The Physics of Fluids* **28**(12): 3451-3456.
- Bayly, B. J. (1986). Onset and equilibration of oscillations in general Rijke devices, *Journal of the Acoustical Society of America* **79**(3): 846-851.
- Bisio, G. and Rubatto, G. (1999). Sondhauss and Rijke oscillations – thermodynamic analysis, possible applications and analogies, *Energy* **24**:117-131.
- Brown, R. S., Dunlap, R., Young, S. W., and Waugh, R. C. (1981). Vortex shedding as a source of acoustic energy in segmented solid rockets, *Journal of Spacecraft* **18**: 312-319.
- Burnley, V. S. and Culick, F. E. C. (2000). Comment on triggering of longitudinal combustion instabilities in rocket motors: nonlinear combustion response, *Journal of Propulsion and Power* **16**(1): 164-166.
- Carrier, G. F. (1955). The mechanics of the Rijke tube, *Quarterly Applied Mathematics* **12**, 383-395.
- Castro, J. P. (1997). Vortex shedding from a ring in oscillatory flow, *Journal of Wind Engineering and Industrial Aerodynamics* **71**: 387-398.
- Chester, W. (1981). Resonant oscillations of a gas in an open-ended tube, *Proceedings of the Royal Society A* **337**: 449-467.
- Churchill, S. W. (1990). Combined free and forced convection around immersed bodies, *Hemisphere Heat Exchanger Design Handbook*, ed. G.F. Hewitt, § 2.5.9., Hemisphere, Washington, D.C.
- Churchill, S. W. and Chu, H. H. S. (1975). Correlating equations for laminar and turbulent free convection from a horizontal cylinder, *International Journal of Heat and Mass Transfer* **18**: 1049-1053.
- Clements, R. R. (1973). An inviscid model of two-dimensional vortex shedding, *Journal of Fluid Mechanics* **57**: 321-336.

- Cohen, J. M. and Anderson, T. J. (1996). Experimental investigation of near-blowout instabilities in a lean, premixed step combustor, AIAA paper no. 96-0819.
- Collyer, A. A. and Ayres, D. J. (1972). The generation of sound in a Rijke tube using two heating coils, *Journal of Physics D: Applied Physics* **5**.
- Correa, S. M. (1998). Power generation and aeropropulsion gas turbines: from combustion science to combustion technology, *27th Symposium on Combustion / The Combustion Institute*.
- Culick, F. E. C. (1976). Nonlinear behavior of acoustic waves in combustion chambers, Parts I and II, *Acta Astronautica* **3**: 714-757.
- Culick, F. E. C. and Magiawala, K. (1979). Excitation of acoustic modes in a chamber by vortex shedding, *Journal of Sound and Vibration* **64**: 455-457.
- Culick, F. E. C. (1988). Combustion instabilities in liquid-fuelled propulsion systems – an overview, *AGARD-CP-450*.
- Dickey, N. S., Selamet, A., and Novak, J. M. (2000). The effect of high-amplitude sound on the attenuation of perforated tube silencers, *Journal of the Acoustical Society of America* **108**(3): 1068-1081.
- Disselhorst, J. H. M. and Van Wijngaarden, L. (1980) Flow in the exit of open pipes during acoustic resonance, *Journal of Fluid Mechanics* **99**: 293-319.
- Dotson, K. W., Koshigoe, S., and Pace, K. K. (1997). Vortex shedding in a large solid rocket motor without inhibitors at the segment interfaces, *Journal of Propulsion and Power* **13**: 197-206.
- Dowling, A. P. (1995). The calculation of thermoacoustic oscillations, *Journal of Sound and Vibration* **180**(4): 557-581.
- Entezam, B., Moohem, W. K., and Majdalani, J. (2002). Two-dimensional numerical verification of the unsteady thermoacoustic field inside a Rijke-type pulse combustor, *Numerical Heat Transfer A* **41**: 245-262.

- Eveleigh, V.W. (1972). *Introduction to Control System Design*, McGraw Hill, New York.
- Feldman, K. T. (1968). Review of the literature on Rijke thermoacoustic phenomena, *Journal of Sound and Vibration*, **7**(1): 83-89.
- Finlinson, J. C., Nelson, M. A., and Beckstead, M. W. (1987). Characterization of a modified Rijke burner for measurement of distributed combustion, *24th JANNAF Combustion Meeting 1*: 13-25.
- Flandro, G. A. (1986). Vortex driving mechanism in oscillatory rocket flows, *Journal of Propulsion 2*: 206-214.
- Fraenkel, S. L., Nogueira, L. A. H., Carvalho-Jr., J. A., and Costa, F. S. (1998). Heat transfer coefficients in pulsating flows, *International Communications in Heat and Mass Transfer 24*: 471-480.
- Fureby, C. (2000). A computational study of combustion instabilities due to vortex shedding, *Proceedings of the Combustion Institute 28*: 783-791.
- Garret, S. L. and Backhaus, S. (2000). The power of sound, *American Scientist 88*(6): 516-525.
- Gurbatov, S. N. and Rudenko, O. V. (1996). *Acoustics in Problems*, Nauka, Moscow.
- Ha, M. Y. and Yavuzkurt, S. (1993). A theoretical investigation of acoustic enhancement of heat and mass transfer – II. Oscillating flow with a steady velocity component, *International Journal of Heat and Mass Transfer 36*: 2193-2202.
- Hanby, V. I. (1969). Convective heat transfer in a gas-fired pulsating combustor, *Journal of Engineering for Power 91*: 48-52.
- Hantschk, C.-C. and Vortmeyer, D. (1999). Numerical simulation of self-excited thermoacoustic instabilities in a Rijke tube, *Journal of Sound and Vibration 277*: 511-522.
- Hatton, A. P., James, D. D., and Swire, H. W. (1970). Combined forced and free convection with low-speed air flow over horizontal cylinders, *Journal of Fluid Mechanics 42*: 17-31.
- Heckl, M. A. (1985). *Heat sources in acoustic resonators*, Ph.D. Thesis. Cambridge University.

- Heckl, M. A. (1988). Active control of the noise from a Rijke tube, *Journal of Sound and Vibration*, **124**: 117-133.
- Heckl, M. A. (1990). Non-linear acoustic effects in the Rijke tube, *Acustica* **72**: 63-71.
- Hedge, U., Reuter, D., Zinn, B., and Daniel B. (1986). Flame driving of longitudinal instabilities in dump type ramjet combustors, AIAA paper no. 86-0371.
- Higgins, B. (1802). *Journal of Natural Philosophy and Chemical Arts* **1**: 129.
- Howe, M. S. (1998). *Acoustics of Fluid-Structure Interactions*, Cambridge University Press, Cambridge.
- Ingard, U. (1953). On the theory and design of Acoustic Resonators, *Journal of the Acoustical Society of America* **25**(6): 1037-1061.
- Ingard, U. and Singhal, V. K. (1975). Effect of flow on the acoustic resonances of an open-ended duct, *Journal of the Acoustical Society of America* **58**: 788-793.
- Ishii, T., Hihara, E., and Saito, T. (1998). Numerical analysis of heat-induced vibration of air column, *International Journal of Japanese Society of Mechanical Engineers* **41**(3): 674-681.
- Jain, V. K., Collins, W. L., and Davis, D. C. (1979). High-accuracy analog measurements via interpolated FFT, *IEEE Transactions on Instrumentation and Measurement* **IM-28**(2): 113-122.
- Jou, W.-H. and Menon, S. (1990). Modes of oscillation in a nonreacting ramjet combustor flow, *Journal of Propulsion* **6**: 535-543.
- Kailasanath, J., Gardner, J., Oran, E., and Boris, J. (1991). Numerical simulation of unsteady reactive flows in a combustion chamber, *Combustion and Flame* **86**: 115-134.
- Kapur, A., Cummings, A., and Mungur, P. (1972). Sound propagation in a combustion can with axial temperature and density gradients, *Journal of Sound and Vibration* **25**: 129-138.
- Karagozian, A. R. and Marble, F. E. (1986). Study of a diffusion flame in a stretched vortex, *Combustion Science and Technology* **45**: 65-84.



- Kaskan, W. E. and Noreen, A. E. (1955). High-frequency oscillations of a flame held by a bluff body, *ASME Transactions* **77**: 885-895.
- Katto, Y. and Sajiki, A. (1977). Onset of oscillation of a gas-column in a tube due to the existence of heat-conduction field, *Bulletin of the Japanese Society of Mechanical Engineers* **20**(147): 1161-1168.
- Keller, J. O., Bramlette, T. T., Westbrook, C. K., and Dec, J. E. (1990). Pulse combustion: the quantification of characteristic times, *Combustion and Flame* **79**: 151-161.
- Kendrick, D. W. (1995). *An Experimental and Numerical Investigation into Reacting Vortex Structures Associated with Unstable Combustion*, Ph.D. Thesis, California Institute of Technology.
- Knudsen, V. O. and Harris, C. M. (1950). *Acoustical Designing in Architecture*, Wiley, New York.
- Kosarev, V. I. (1995). *Twelve Lectures on Computational Mathematics*, MIPT, Moscow.
- Kwon, Y.-P. and Lee, B.-H. (1985). Stability of the Rijke thermoacoustic oscillation, *Journal of the Acoustical Society of America* **78**(4), 1414-1420.
- Laverdant, A. M. and Candel, S. M. (1989). Computation of diffusion and premixed flames rolled up in vortex structures, *Journal Propulsion and Power* **5**: 134-143.
- Lehmann, K. O. (1937). Uber die theory der netztone, *Annalen der Physik* **29**: 527-555.
- Levine, H. and Schwinger, J. (1948). On the radiation of sound from an unflanged circular pipe, *Physical Review Letters* **73**: 383-406.
- Lienhard, J. H. (1973). On the commonality of equations for natural convection from immersed bodies, *International Journal of Heat and Mass Transfer* **16**: 2121-2123.
- Lighthill, M. J. (1954). The response of laminar skin friction and heat transfer to fluctuations in the stream velocity, *Proceedings of the Royal Society A* **224**: 1-23.

- Madarame, H. (1981). Thermally induced acoustic oscillations in a pipe, *Bulletin of the Japanese Society of Mechanical Engineers* **24**(195): 1626-1633.
- Maling, G. C. (1963). Simplified analysis of the Rijke phenomenon, *Journal of the Acoustical Society of America* **35**(7): 1058-1060.
- Marble, F. E. (1985). Growth of a diffusion flame in the field of a vortex, *Recent Advances in the Aerospace Sciences*: 395-413.
- Margolin, A. (1999). Early investigations of solid-propellant combustion instability in Russia, *Journal of Propulsion and Power* **15**(6): 922-925.
- Marone, I. Y. and Tarakanovskii, A. A. (1967). Investigation of sound generation in a Rijke tube, *Soviet Physics - Acoustics*, **12**(2): 261-263.
- Matveev, K. I. and Culick, F. E. C. (2001). A study of thermoacoustic instabilities in a resonator with heat release, *142nd Meeting of the Acoustical Society of America*, Fort Lauderdale, FL.
- Matveev, K. I. and Culick, F. E. C. (2002a). Experimental and mathematical modeling of thermoacoustic instabilities in a Rijke tube, *40th Aerospace Meeting and Exhibit*, Reno, NV, AIAA paper no. 2002-1013.
- Matveev, K. I. and Culick, F. E. C. (2002b). A study of the transition to instability in a Rijke tube with axial temperature gradient, *Journal of Sound and Vibration*, in press.
- Matveev, K. I. and Culick, F. E. C. (2002c). On the nonlinear characteristics of a Rijke tube, *Proceedings of the 9th International Congress on Sound and Vibration*, Orlando, FL.
- Matveev, K. I. and Culick, F. E. C. (2002d). A model for combustion instabilities due to vortex shedding in rocket motors, *Proceedings of the 9th International Congress on Sound and Vibration*, Orlando, FL.
- Matveev, K. I. and Culick, F. E. C. (2002e). Modeling of unstable regimes in a Rijke tube, *Proceedings of the 5th International Symposium on Fluid-Structure Interactions*, New Orleans, LA, ASME paper IMECE 2002-33369.

- Matveev, K. I. and Culick, F. E. C. (2002f). A model for combustion instabilities involving vortex shedding, *Combustion Science and Technology*, in press.
- Matveev, K. I. and Culick, F. E. C. (2003a). Nonlinear modeling of heat transfer functions in thermoacoustic systems, *41st Aerospace Sciences Meeting & Exhibit*, Reno, NV, AIAA paper no. 2003-165.
- Matveev, K. I. and Culick, F. E. C. (2003b). Limit-cycle properties of the Rijke tube: experiment and modeling, *Journal of Sound and Vibration*, submitted.
- McQuay, M. Q., Dubey, R. K., and Carvalho Jr., J. A. (2000). The effect of acoustic mode on time-resolved temperature measurements in a Rijke-tube pulse combustor, *Fuel* **79**: 1645-1655.
- Merk, H. J. (1957). Analysis of heat-driven oscillations of gas flows, *Applied Scientific Research*, **A 6**: 402-420.
- Metais, B., and Eckert, E. R. G. (1964). Forced, mixed, and free convection regimes, *Journal of Heat Transfer* **86**: 295-296.
- Mills, A. F. (1992). *Heat Transfer*, Irwin, Homewood, Illinois.
- Murray, R. M. (1995). *Sparrow Reference Manual*, California Institute of Technology.
- Najm, H. N. and Ghoniem, A. F. (1993). Modeling pulsating combustion due to flow-flame interactions in vortex-stabilized pre-mixed flames, *Combustion Science and Technology* **94**: 259-278.
- Neuringer, J. L. and Hudson, G. E. (1952). An investigation of sound vibrations in a tube containing a heat source, *Journal of the Acoustical Society of America* **24**: 667-674.
- Nicoli, C. and Pelce, P. (1989). One-dimensional model for the Rijke tube, *Journal of Fluid Mechanics* **202**, 83-96.
- Perry, E. H. and Culick, F. E. C. (1974). Measurements of wall heat-transfer in presence of large-amplitude combustion-driven oscillations, *Combustion Science and Technology* **9**: 49-53.

- Poinsot, T., Trounev, A., Veynante, D., Candel, S., and Espitito, E. (1987). Vortex-driven acoustically coupled combustion instabilities, *Journal of Fluid Mechanics* **117**: 265-292.
- Poncica, G. (1998). *A Study on Thermoacoustic Instability Phenomena in Combustion Chambers for Active Control*, Ph.D. Thesis, Politecnico di Milano.
- Pun, W. (2001). *Measurements of Thermo-Acoustic Coupling*, Ph.D. Thesis, California Institute of Technology.
- Putman, A. A. and Dennis, W. R. (1954). Burner oscillations of the gauze-tone type, *Journal of the Acoustical Society of America* **26**(5): 716-725.
- Randall, R. B. (1998). Acoustical and vibration analysis, in *Handbook of Acoustical Measurements and Noise Control*, edited by Harris, S.M., American Institute of Physics.
- Raun, R. L. and Beckstead, M. W. (1993). A numerical model for temperature gradient and particle effects on Rijke burner oscillations, *Combustion and Flame* **94**: 1-24.
- Raun, R. L., Beckstead, M. W., Finlinson, J. C., and Brooks, K. P. (1993). A review of Rijke tubes, Rijke burners and related devices, *Progress in Energy and Combustion Science* **19**: 313-364.
- Rayleigh, J. W. S. (1945, re-issue). *The Theory of Sound*, Dover Publications.
- Rijke, P. L. (1859). Notiz über eine neue art, die luft in einer an beiden enden offenen Röhre in schwingungen zu versetzen, *Annalen der Physik*, **107**: 339-343.
- Rogers, D. E. and Marble, F. E. (1956). A mechanism for high-frequency oscillations in ramjet combustors and afterburners, *Jet Propulsion* **26**: 456-462.
- Rosfjord, T. (1995). Lean-limit combustion instability, *United Technologies Research Center*.
- Saito, T. (1965). Vibrations of air-columns excited by heat supply, *Bulletin of the Japanese Society of Mechanical Engineers* **8**(32): 651-659.
- Schadow, K., Gutmark, E., Parr, T., Parr, K., Wilson, K., and Crump, J. (1989). Large-scale coherent structures as drivers of combustion instability, *Combustion Science and Technology* **64**: 167-186.

- Schadow, K. and Gutmark, E. (1992). Combustion instability related to vortex shedding in dump combustors and their passive control, *Progress in Energy and Combustion Sciences* **18**: 117-132.
- Smith, D. A. and Zukoski, E. E. (1985). Combustion instability sustained by unsteady vortex shedding, AIAA paper no. 85-1248.
- Sterling, J. D. and Zukoski, E. E. (1991). Nonlinear dynamics of laboratory combustor pressure oscillations, *Combustion Science and Technology* **77**: 225-238.
- Sterling, J. D. (1993). Nonlinear analysis and modeling of combustion instabilities in a laboratory combustor, *Combustion Science and Technology* **89**: 167-179.
- Swift, G. W. (1988). Thermoacoustic engines, *Journal of the Acoustical Society of America* **84**(4): 1145-1180.
- Stuart, J. T. (1966). Double boundary layers in oscillatory viscous flow, *Journal of Fluid Mechanics* **24**: 673-687.
- Tarakanovskii, A. A. and Steinberg, V. B. (1972). Generation of acoustic oscillations in a Rijke tube with a double gauze system, *Soviet Physics - Acoustics*, **18**(2): 246-250.
- Torczynski, J. R. and O'Hern, T. J. (1995). Reynolds number dependence of the drag coefficient for laminar flow through electrically-heated photoetched screens, *Experiments in Fluids* **18**: 206-209.
- Wibulswas, P. (1966). *Laminar Flow Heat Transfer in Non-Circular Ducts*, Ph. D. Thesis, London University.
- Yoon, H.-G., Peddieson, J., and Purdy, K. R. (1998). Mathematical modeling of a generalized Rijke tube, *International Journal of Engineering Science* **36**: 1235-1264.
- Yoon, H.-G., Peddieson, J., and Purdy, K. R. (2001). Nonlinear response of a generalized Rijke tube, *International Journal of Engineering Science* **39**: 1707-1723.
- Yu, K. H., Trouve, A. C., and Daily, J. W. (1991). Low-frequency pressure oscillations in a model ramjet combustor, *Journal of Fluid Mechanics* **232**: 47-72.

Zsak, T. W. (1993). *An Investigation of the Reacting Vortex Structures Associated with Pulse Combustion*, Ph.D. Thesis, California Institute of Technology.

Zukauskas, A. (1987). Convective heat transfer in cross flow, in *Handbook of Single-Phase Convective Heat Transfer*, edited by S. Kakac et al., Wiley, New York.